Pion Interferometry in AuAu Collisions at a Center of Mass Energy per Nucleon of 200 GeV

DISSERTATION

Presented in Partial Fulfillment of the Requirements for

the Degree Doctor of Philosophy in the

Graduate School of The Ohio State University

By

Mercedes López Noriega, B.S. Physics

* * * * *

The Ohio State University

2004

Dissertation Committee:

Professor Michael A. Lisa, Adviser

Professor Thomas Humanic

Professor Ulrich W. Heinz

Professor Terrence P. Walker

Approved by

_____

Adviser

Department of Physics

ABSTRACT

Quantum Chromodynamics predicts a phase transition from a state formed by hadrons to a plasma of deconfined quarks and gluons, the Quark Gluon Plasma, as a the energy density exceeds a critical value. This deconfined phase is believed to be the one in which the early universe existed in a time-scale $\sim 10^{-5}$ s after the Big Bang.

Ultrarelativistic Heavy Ion Collisions, like the ones that take place at the Relativistic Heavy Ion Collider at Brookhaven National Laboratory, reach energy densities above the critical value creating a deconfined phase of quarks and gluons that can be studied at the laboratory. This gives us the opportunity to study a phase of matter in the deconfined region of QCD, the properties of the strong interaction, the formation of hadronic matter and the interaction between hadrons.

In the analysis presented in this thesis, the dynamical evolution of the particle emitting source and its space-time structure at freeze-out is studied using the two particle intensity interferometry technique. The expansion of the source is also studied. We find indications that this expansion may be caused by the initial pressure gradient generated in the initial stages of the collision through particle rescattering in a very dense medium.

A mis padres, Carlos y Mercedes.

ACKNOWLEDGMENTS

This thesis would have not been possible without the effort of the members of the STAR Collaboration to whom I would like to express my gratitude. In particular, I would like to thank every member of the STAR HBT group for their comments and criticisms on my analysis. Thanks to Fabrice Retière for helping me to get as much as possible from my analysis and for the long discussions on HBT from which I benefitted so much. I would also like to thank other members of STAR with whom I had the privilege of working with, those include Jerome Lauret, Sergey Panitkin, Gael Renault, Tom Gutierrez, Manuel Calderón de la Barca Sánchez, Zbigniew Chakecki and many more.

Special thanks to my advisor, Mike Lisa, who convinced me to stay and gave me the opportunity of living a great experience. His challenges and questions made me think and learn about what I was doing. Thanks Mike.

Also thanks to the members of my dissertation committee, Tom Humanic, Ulrich Heinz and Terry Walker for their help during these years and for reading and improving this thesis.

I would also like to thank the members of the Relativistic Heavy Ion Group at OSU. Thanks to Helen Caines and Frank Laue that helped me to get started and answered all my questions at the beginning. Thanks to Randy Wells,

who helped me to understand HBT, and Robert Willson whose help at the beginning was also invaluable. Also thanks to Selemon Bekele, Howard Dyke, Ivan Kotov, Dan Magestro, Bjorn Nilsen and Mary Smith. Thanks to J.D. from the Physics department who helped me with my endless computer problems.

I would also like to thank all the friends I have made during the past few years. They made my experience more enjoyable and were there when I needed them. Special thanks to Carlos, Nacho, Cecilia, Amaya, Savvas, Markus and Thomas with whom I shared great times.

No habría conseguido llegar hasta aquí sin el apoyo constante y el amor de mi familia. Gracias a mis padres, Carlos y Mercedes, quienes me empujaron a la vida. Gracias a mis hermanos, Isabel, Carlos y Adolfo por estar siempre a mi lado. Pita, gracias.

Javier, gracias por todo lo que me has enseñado, gracias por contestar a mis preguntas una y otra vez, gracias por darme ánimos cuando me costaba seguir... pero sobre todo gracias por haberme hecho tan feliz y por todo el amor de estos últimos años.

VITA

8 September 1974	Madrid, Spain
June 1999	M.S. Physics Universidad Autónoma de Madrid Madrid, Spain
1999 - present	Graduate Research Assistant Department of Physics The Ohio State University

PUBLICATIONS

Azimuthally sensitive HBT in Au+Au collisions at $\sqrt{s_{NN}}$ = 200 GeV
J. Adams *et al.* (STAR Collaboration), Phys. Rev. Lett. **93**, 012301 (2004)

Azimuthal anisotropy at the Relativistic Heavy Ion Collider: the first and fourth harmonics
J. Adams *et al.* (STAR Collaboration), Phys. Rev. Lett. **92**, 062301 (2004)

Cross Sections and Transverse Single-Spin Asymmetries in Forward Neutral Pion Production from Proton Collisions at $\sqrt{s_{NN}}$ = 200 GeV
J. Adams *et al.* (STAR Collaboration), Phys.Rev.Lett.**92**, 171801 (2004)

Identified particle distributions in pp and Au+Au collisions at $\sqrt{s_{NN}}$ = 200 GeV
J. Adams *et al.* (STAR Collaboration), Phys.Rev.Lett.**92**, 112301 (2004)

Pion-Kaon correlations in AuAu collisions at $\sqrt{s_{NN}}$ = 130 GeV
J. Adams *et al.* (STAR Collaboration), Phys.Rev.Lett.**91**, 262302 (2003)

Multi-Strange Baryon Production in AuAu collisions at $\sqrt{s_{NN}}$ = 130 GeV
J. Adams *et al.* (STAR Collaboration), Phys.Rev.Lett.**92**, 182301 (2004)

ρ^0 Production and Possible Modification in AuAu and pp Collisions at $\sqrt{s_{NN}}$ = 200 GeV
J. Adams *et al.* (STAR Collaboration), Phys.Rev.Lett.**92**, 092301 (2004)

Multiplicity fluctuations in AuAu collisions at $\sqrt{s_{NN}}$ = 130 GeV
J. Adams *et al.* (STAR Collaboration), Phys.Rev.**C68**, 044905(2003)

Three-Pion HBT Correlations in Relativistic Heavy-Ion Collisions from the STAR Experiment
J. Adams *et al.* (STAR Collaboration), Phys.Rev.Lett.**91**, 262301 (2003)

Evidence from dAu measurements for final-state suppression of high p_T hadrons in AuAu collisions at RHIC
J. Adams *et al.* (STAR Collaboration), Phys.Rev.Lett.**91**, 072304 (2003)

Particle dependence of azimuthal anisotropy and nuclear modification of particle production at moderate p_T in AuAu collisions at $\sqrt{s_{NN}}$ = 200 GeV
J. Adams *et al.* (STAR Collaboration), Phys.Rev.Lett.**92**, 052302 (2004)

Transverse momentum and collision energy dependence of high p_T hadron suppression in AuAu collisions at ultrarelativistic energies
J. Adams *et al.* (STAR Collaboration), Phys. Rev. Lett. **91**, 172302 (2003)

Narrowing of the Balance Function with Centrality in AuAu Collisions at $\sqrt{s_{NN}}$ = 130 GeV
J. Adams *et al.* (STAR Collaboration), Phys. Rev. Lett. **90**, 172301 (2003)

Strange anti-particle to particle ratios at mid-rapidity in $\sqrt{s_{NN}}$ = 130 GeV AuAu collisions
J. Adams *et al.* (STAR Collaboration), Phys. Lett. **B567**, 167-174 (2003)

Disappearance of back-to-back high p_T hadron correlations in central AuAu collisions at $\sqrt{s_{NN}}$ = 200 GeV
J. Adams *et al.* (STAR Collaboration), Phys. Rev. Lett. **90**, 082302 (2003)

Centrality Dependence of High p_T Hadron Suppression in AuAu Collisions at $\sqrt{s_{NN}}$ = 200 GeV
C. Adler *et al.* (STAR Collaboration), Phys. Rev. Lett. **89**, 202301 (2002)

Azimuthal Anisotropy and Correlations in the Hard Scattering Regime at RHIC
C. Adler *et al.* (STAR Collaboration), Phys. Rev. Lett. **90**, 032301 (2003)

Coherent Rho-zero Production in Ultra-Peripheral Heavy Ion Collisions
C. Adler *et al.* (STAR Collaboration), Phys. Rev. Lett. **89**, 272302 (2002)

Elliptic flow from two- and four-particle correlations in AuAu collisions at $\sqrt{s_{NN}}$ = 130 GeV
C. Adler *et al.* (STAR Collaboration), Phys. Rev. **C66**, 034904 (2002)

K*(892) Production in Relativistic Heavy Ion Collisions at $\sqrt{s_{NN}}$ = 130 GeV
C. Adler *et al.* (STAR Collaboration), Phys. Rev. **C66**, 061901(R) (2002)

Azimuthal anisotropy of K0s and Lambda + Lambdabar production at mid-rapidity from AuAu collisions at $\sqrt{s_{NN}}$ = 130 GeV
C. Adler *et al.* (STAR Collaboration), Phys. Rev. Lett. **89**, 132301 (2002)

Mid-rapidity Lambda and Lambda bar Production in AuAu Collisions at $\sqrt{s_{NN}}$ = 130 GeV
C. Adler *et al.* (STAR Collaboration), Phys. Rev. Lett. **89**, 092301 (2002)

Mid-rapidity phi production in AuAu collisions at $\sqrt{s_{NN}}$ = 130 GeV
C. Adler *et al.* (STAR Collaboration), Phys. Rev. **C65**, 041901(R) (2002)

Measurement of inclusive antiprotons from AuAu collisions at $\sqrt{s_{NN}}$ = 130 GeV
C. Adler *et al.* (STAR Collaboration), Phys. Rev. Lett. **87**, 262302-1 (2001)

Antideuteron and Antihelium production in Au+Au collisions at $\sqrt{s_{NN}}$ = 130 GeV
C. Adler *et al.* (STAR Collaboration), Phys. Rev. Lett. **87**, 262301-1 (2001).

Identified Particle Elliptic Flow in AuAu Collisions at $\sqrt{s_{NN}}$ = 130 GeV
C. Adler *et al.* (STAR Collaboration), Phys. Rev. Lett. **87**, 182301 (2001).

Multiplicity distribution and spectra of negatively charged hadrons in AuAu collisions at $\sqrt{s_{NN}}$ = 130 GeV
C. Adler *et al.* (STAR Collaboration), Phys. Rev. Lett. **87**, 112303 (2001).

Pion Interferometry of $\sqrt{s_{NN}}$ = 130 GeV AuAu collisions at RHIC
C. Adler *et al.* (STAR Collaboration), Phys. Rev. Lett. **87**, 082301 (2001).

Midrapidity Antiproton-to-Proton Ratio from AuAu $\sqrt{s_{NN}}$ = 130 GeV
C. Adler *et al.* (STAR Collaboration), Phys. Rev. Lett. **86**, 4778 (2001).

Elliptic Flow in Au+Au Collisions at $\sqrt{s_{NN}}$ = 130 GeV
K.H. Ackermann *et al.* (STAR Collaboration), Phys. Rev. Lett. **86**, 402 (2001).

Conference Contribution:

Pion Interferometry in AuAu collisions at $\sqrt{s_{NN}}$ = 200 GeV
M. López Noriega (for the STAR Collaboration), contributed to 2^{nd} Warsaw Meeting on Particle Correlations and Resonances in Heavy Ion Collisions, Warsaw, Poland, 15-18 Oct 2003; nucl-ex/0401037

Identical Particle Interferometry at STAR
M. López Noriega (for the STAR Collaboration), Contributed to 16th International Conference on Ultrarelativistic Nucleus-Nucleus Collisions, Quark Matter 2002 (QM 2002), Nantes, France, 18-24 Jul 2002; Nucl.Phys.A**715**, 623 (2003)

FIELDS OF STUDY

Major Field: Physics

Studies in Experimental Nuclear Physics: Professor Michael A. Lisa

TABLE OF CONTENTS

Page

LIST OF FIGURES

LIST OF TABLES

Table **Page**

CHAPTER 1

INTRODUCTION

Quantum Chromodynamics (QCD) is the theory of the strong interaction, it describes the forces between the colored particles: quarks and gluons. Quarks are never seen in isolation, but only in strongly interacting particles, called hadrons, which are either baryons (formed by three quarks) or mesons (formed by a quark-antiquark pair) [1]. The color force (or strong force) is carried by gluons, just as the electromagnetic force between charged particles is carried by photons. However, whereas photons carry no electric charge, gluons carry color charge so they can interact with each other.

QCD predicts a phase transition from a state formed by hadrons to a plasma of deconfined quarks and gluons, as the energy density exceeds a critical value [2, 3]. This state is called the Quark Gluon Plasma (QGP) [4, 5], and is believed to be the one in which the early universe existed in a time-scale $\sim 10^{-5}$ s after the Big Bang [6].

Ultra-relativistic heavy ion collisions are a promising tool for the creation of a QGP in the laboratory, and for studying the properties of the strong interaction and the strongly interacting matter.

The experimental search for the QGP started in the mid 1980s at the Alternating Gradient Synchrotron (AGS) in Brookhaven National Laboratory (BNL), and at the Super Proton Synchrotron (SPS) in CERN. Since then, many collisions at different energies have been produced and studied in a fixed target basis, with one heavy ion beam impinging upon a stationary target (for recent reviews one can refer to the proceedings of the "Quark Matter" conferences, see [7, 8, 9, 10] for most recent ones).

In 2000, the Relativistic Heavy Ion Collider (RHIC) at BNL produced the first collisions of two heavy ion beams accelerated in two concentric rings. This method has the advantage, over the fixed target one, of being able to achieve higher center of mass energies. The Solenoidal Tracker at RHIC (STAR) is one of the four experiments at RHIC.

The analysis presented here, in which we extract information about the space-time geometry of the collision region, is based on data taken by STAR from AuAu collisions at a center of mass energy per nucleon pair $\sqrt{s_{NN}}$ = 200 GeV. This thesis is organized as follows. It starts with a brief introduction on the physics of the strong interaction at high energy densities and the experimental search for the QGP in Chapters 2 and 3. A theoretical overview of two particle interferometry (HBT) is given in Chapter 4. In Chapter 5, a description of the STAR detector is presented. The analysis method is described in Chapter 6. The results as well as the discussion of them are presented in Chapter 7. It finishes with conclusion and outlook.

CHAPTER 2

THE QUARK-GLUON PLASMA

QCD predicts a phase transition from hadronic matter to a deconfined state of quarks and gluons. In this chapter, an overview of this latter state of matter and the transition as described by QCD is given.

2.1 Deconfinement and Chiral Symmetry Restoration

QCD is the theory that describes the strong interaction between quarks and gluons. The strength of this interaction is given by the QCD running coupling constant $\alpha_s(q^2)$, which depends on the momentum transfer, q, as,

$$\alpha_s(q^2) = \frac{12\pi}{(33 - 2n_f)\ln\left(\frac{q^2}{\Lambda^2_{QCD}}\right)}. \tag{2.1}$$

Here, n_f is the number of flavors with mass below $|q^2|^{1/2}$ and Λ_{QCD} is a (dimensional) parameter introduced by the renormalization process.

If $\alpha_s(q^2)$ is expressed in terms of the coordinate space, r, which is inversely proportional to q, $\alpha_s(r)$ grows like r^2 for large distances, leading to a rising strength of the interaction with r. This behavior of the coupling constant results in the confinement of quarks and explains the fact that they are never

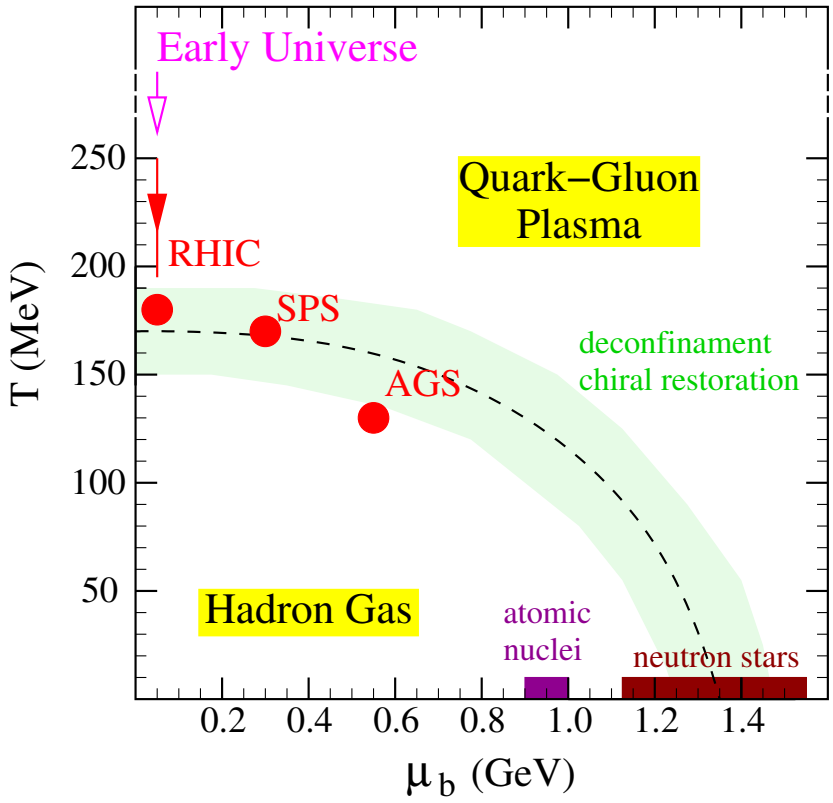

Figure 2.1: QCD phase diagram, temperature T vs. baryon chemical potential μ_b associated with the baryon density ρ_b. The dashed line and shadowed region indicate the most likely location for the transition and its theoretical uncertainty. Red dots indicate the region reached by different experiments.

seen in isolation but only in strongly interacting matter. However, at very small distances (large q^2), $\alpha_s(r) \rightarrow 0$, the coupling strength between color charged particles decreases, and quarks and gluons can be thought to be free particles. This is a fundamental property of the strong interaction known as "asymptotic freedom".

Therefore, based on the asymptotic freedom, QCD predicts a transition from a state formed by hadrons to a plasma of deconfined quarks and gluons, at sufficient high energy density, where the average distance between particles becomes smaller and confinement disappears [2, 3]. This critical energy density ε_c, at which the transition takes place, can be reached by heating the matter at zero baryon chemical potential to a temperature T_c, by compressing the nuclear matter at zero temperature to baryon densities above ρ_c, or by a combination of both, as can be seen in the QCD phase diagram of Fig. 2.1 [11].

At zero temperature and high baryon densities we expect a deconfined high-density phase predicted to exist in the interior of the neutron stars [12]. The region at zero baryon chemical potential and high temperatures is the one predicted to exist at the early universe [6] and the one expected to be reached at the highest energy collisions at RHIC, where the baryon chemical potential is very small.

An important result of lattice QCD calculations is that at the critical temperature for deconfinement, the approximate chiral symmetry of QCD, which is spontaneously broken at low temperatures, is restored [13]. Chiral symmetry is related to the helicity of the quarks. If the quark fields are decomposed into left and right chirality components: $\psi_{L,R} = (1 \mp \gamma_5 \psi)$, the QCD Lagrangian with 3 massless quarks is invariant under the independent transformations of right- and left-handed fields ("chiral rotations"). Therefore, in the limit of massless quarks, QCD possesses chiral symmetry.

At temperatures below T_c, quarks are confined in hadrons and do not appear as massless constituents, but instead posses mass of a few hundred MeV, that is generated dynamically, and the symmetry gets broken. Also, the fact that the density of $q\bar{q}$ pairs in the QCD vacuum, as given by the *quark condensate* $\langle q\bar{q}\rangle$, is non-vanishing is directly related to chiral symmetry breaking [14].

Lattice QCD calculations show that around the critical temperature for deconfinement, in which the interaction between quarks is minimized and their effective masses are no longer given by their dynamical masses but by their current mass values which are much smaller, quark condensate dramatically decreases and chiral symmetry is restored.

This phase of QCD that exhibits deconfinement and chiral symmetry is the one called Quark Gluon Plasma.

2.1.1 Phase transition at $\mu_b = 0$

The region μ_b = 0 in Fig. 2.1 is accessible to lattice QCD numerical simulations [15]. These methods provide reliable predictions for the thermodynamic properties of the transition for systems with 2- and 3- flavor quarks. The results from these calculations are shown in Fig. 2.2, where the transition to free quarks and gluons is observed in the sudden increase of the energy density as a function of temperature. The critical temperature for the 2-flavor light quarks case, as predicted by these simulations, is $T_c \sim 170$ MeV with a critical density $\varepsilon_c \sim 0.7$ GeV, for the 3-flavor case T_c is smaller by about 20

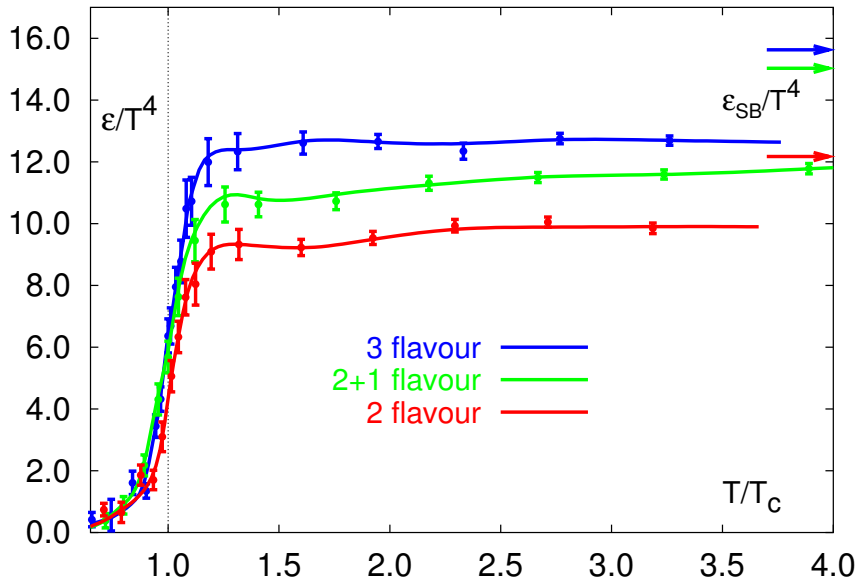

Figure 2.2: Energy density ε/T^4 vs. T/T_c for the case of 2- or 3-flavor light quarks and for the one with 2-flavor light quarks plus 1-flavor heavy quark. Arrows show the ideal gas limit ε_{SB}.

MeV [16, 17]. For the most realistic case of 2-flavor light quarks and 1-flavor heavier quark $T_c \simeq 160$ MeV [18].

One could think that in the QGP phase, the QCD coupling constant is very small and the interaction between (massless) particles is very weak so, to a good approximation, the QGP becomes an ideal gas whose properties can be studied by thermodynamics [19]. The grand partition function for a relativistic gas of fermions, or bosons, is:

$$(T \ln Z)_f = \frac{g_f V}{12}\left(\frac{7\pi^2}{30}T^4 + \mu^2 T^2 + \frac{1}{2\pi^2}\mu^4\right), \qquad (T \ln Z)_b = \frac{g_b V \pi^2}{90}T^4, \tag{2.2}$$

where g_f and g_b are the degeneracies (degrees of freedom). And the energy density, particle number, pressure and entropy density are:

$$\varepsilon = \frac{T}{V}\frac{\partial(T\ln Z)}{\partial T} + \mu n, \quad n = \frac{1}{V}\frac{\partial(T\ln Z)}{\partial \mu}, \quad P = \frac{\partial(T\ln Z)}{\partial V}, \quad s = \frac{1}{V}\frac{\partial(T\ln Z)}{\partial T}. \tag{2.3}$$

Using the thermodynamic relation $\varepsilon = -P + Ts + \mu n$, one gets that the equation of state for an ideal massless gas is $P = \varepsilon/3$. Assuming $g_h = 3$ for the hadronic gas if everything is pions, $g_q = 3 \times 2 \times 2 \times N_f$ for the quarks, where N_f is the number of flavors, and $g_g = 2 \times 8$ for the gluons:

$$\frac{\varepsilon_h}{T^4} = \frac{\pi^2}{10}, \qquad \frac{\varepsilon_{qg}}{T^4} = (16 + \frac{21}{2}N_f)\frac{\pi^2}{30}T^4. \tag{2.4}$$

For $N_f = 3$, $\frac{\varepsilon_{qg}}{T^4} = 15.6$ is denoted as the Stefan-Boltzmann limit, and is indicated by the arrows (ε_{SB}/T^4) in Fig. 2.2 [15]. The calculated values using lattice QCD are below the values for an ideal gas, indicating strong interaction among partons even above the phase transition temperature T_c.

It is not yet clear if the transition between hadronic matter and QGP is a phase transition or just a rapid crossover. At zero baryon chemical potential and for the most realistic case of QCD with 2 flavors of light quarks and 1 flavor of a heavier quark, the order of the phase transition seems to depend on the numerical values of the masses of the light and heavy quarks [20, 18]. If the latter is too heavy, the transition might be just a rapid increase of the energy density over a small temperature interval, *i.e.* a rapid crossover.

Calculations at non-zero baryon chemical potential suggest the existence of a critical point at an undetermined value of $\mu_b = \mu_b(C.P.)$ which is most likely above the value of the baryon chemical potential at RHIC energies.

Transitions between the hadronic and the QGP phase at values of μ_b above $\mu_b(C.P.)$ would be first-order transitions while the ones at μ_b below $\mu_b(C.P.)$ would be crossover transitions [21].

CHAPTER 3

HEAVY ION COLLISIONS

Ultrarelativistic heavy ion collisions are the way of "heating" hadronic matter to temperatures above T_c, and densities above ε_c, creating a deconfined phase of quarks and gluons that can be studied in the laboratory. If this matter thermalizes quickly at an energy density still above ε_c, it passes through the QGP phase as the collision fireball expands and cools down.

This gives us the opportunity to study, not only the characteristics of an unknown phase of matter in an asymptotic region of QCD, but also the properties of the strong interaction, the formation of hadronic matter and the interaction between hadrons.

In this chapter, a description of how the collision region evolves and some unique signatures of the possible QGP formation are described. Some important results from RHIC are shown and the porpoise of the analysis presented in this thesis is given.

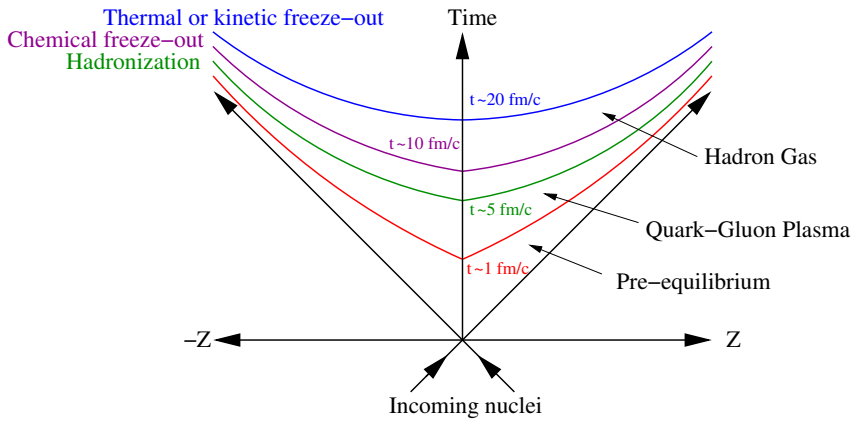

Figure 3.1: Space-time evolution of a heavy ion collision that undergoes a phase transition to a QGP.

3.1 The space-time evolution of the collision

The different stages of the collision of two heavy ions at sufficient high energy to create a phase of deconfined quarks and gluons is shown in Fig. 3.1. After the two initial nuclei collide, there is a pre-equilibrium stage in which each nucleon scatters several times and partons (quarks and gluons) are liberated. At some point these quarks and gluons thermalize by re-scattering, resulting in a thermalized QGP. The system expands collectively and cools down to temperatures around T_c, reaching hadronization in which hadrons are formed from the quarks and gluons. The hadrons then interact inelastically until the system reaches chemical freeze out when this kind of interactions stop as it keeps expanding. At that point there is not enough energy to change the different species population, however these hadrons are still

interacting elastically. Eventually, the system is diluted enough that the interaction between hadrons stops, the system undergoes a thermal freeze-out and hadrons fly off to the detectors.

At RHIC energies, the critical temperature T_c at which hadronization takes place and the chemical freeze-out temperature T_{ch} at which chemical equilibration takes place are very similar. T_c is calculated by lattice QCD and T_{ch} is extracted from a statistical model that reproduces the measured particle ratios [22]. This implies that in nucleus-nucleus collisions at RHIC energies, hadron multiplicities are established very close to the phase boundary between hadronic and quark matter.

3.2 Initial conditions

One can estimate the initially produced energy density by using the Bjorken estimate [23]

$$\varepsilon = \frac{\omega_h}{\pi R_A^2 \tau_0} \Big(\frac{dN_h}{dy} \Big)_{y=0}, \tag{3.1}$$

where $(dN_h/dy)_{y=0}$ is the number of hadrons per unit of rapidity produced at midrapidity, ω_h is the average energy of the hadrons, R_A is the nuclear radius and τ_0 is the formation time of the medium, which is not known but is generally taken to be 1 fm/c.

According to lattice QCD calculations, about 1 GeV/fm^3 is needed to make the transition to deconfined quarks and gluons. The estimate energy density for RHIC for central AuAu collisions at $\sqrt{s_{NN}} = 200$ GeV is ~ 5.0 GeV/fm^3 [24], which clearly exceeds the energy density necessary to generate a deconfined

state of quarks and gluons. We should therefore look for possible signatures of a QGP phase.

3.3 QGP signatures

The experiments detect hadrons after thermal freeze-out when they have lost most of the information about the early stages of the collision, and their formation, through rescattering and collective expansion. However, there are observables that can provide information about the early stages of the collision and the possible QGP phase. These early observables are discussed next.

3.3.1 Direct photons

The thermalized QGP would emit thermal radiation, real photons and virtual photons ($\gamma* \rightarrow e^+e^-$ or $\mu^+\mu^-$) produced in quark-antiquark annihilation ($q\bar{q} \rightarrow \gamma g$) and Comptom scattering ($qg \rightarrow \gamma q$) processes. These direct photons and leptons only interact through electromagnetic interaction and have a large mean free path compared to the size of the fireball so they escape the system without re-scattering carrying information on the earliest deconfined stage [25, 26].

However, direct photons, as well as dileptons, are very difficult to measure experimentally due to the large background of photons, and dileptons, emitted during the hadronic gas phase. No conclusive photon or dilepton spectra confirming the QGP phase have been measured so far, but there is a continuous effort to improve the sensibility of these measurements.

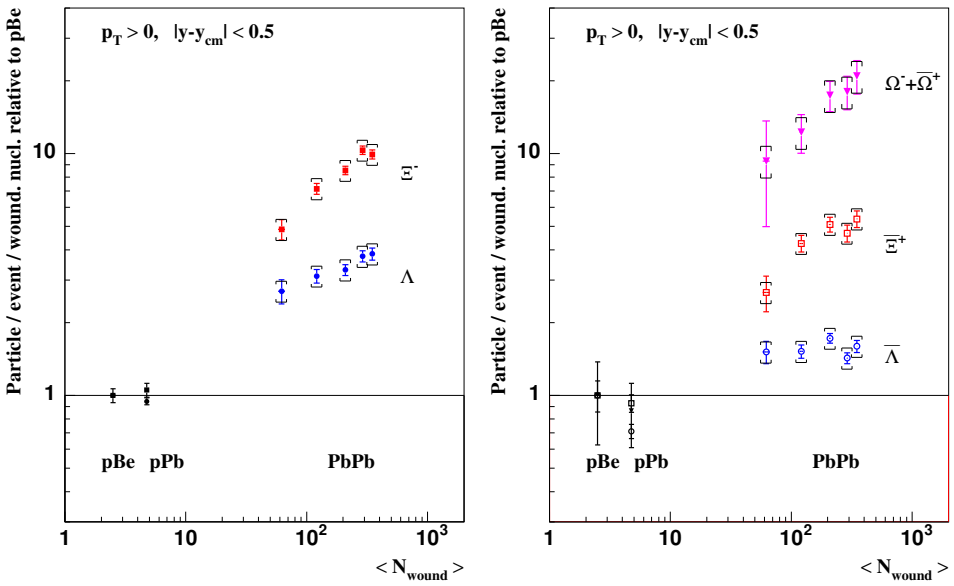

Figure 3.2: Strange particle yields scaled by the number of participants and normalized by p-Be collisions in PbPb collisions at 158 A GeV/c and pBe collisions at 40 A GeV/c.

3.3.2 Strangeness Enhancement

In purely hadronic reactions, the production of strange quarks (s) is normally suppressed due to the high mass of the s-quark compared to the u and d masses. With the high energy and gluon density in the QGP, the production of strange quarks and anti-quarks by gluon fusion should be enhanced as compared with lower energy and purely hadronic collisions [27, 28, 29]. Therefore, important observables are the yield and ratios of strange hadrons at different energies. Figure 3.2 [30] shows the enhancement of strange particles in heavy ion collisions (PbPb collisions at 158 A GeV/c) as compared to pBe collisions

at 40 A GeV/c. The enhancement increases with the strange quark content ($\Omega^-(sss)$, $\Xi^-(dss)$, $\Lambda(uds)$) [30].

3.3.3 Charmonium Suppression

Heavy quarks (c and b) are exclusively created in primary hard collisions. Consequently, they are ideal messengers of the early stage of the collision and the QGP formation. The J/ψ meson is a bound $c\bar{c}$ state. As it is tightly bound, it is unlikely to become unbound in interactions with hadronic matter and escapes the collision region. However, at high energies with a high gluon density resulting from the color deconfinement, a lot of light $q\bar{q}$ pairs are produced that act as screening color charges around the heavy quark pairs weakening the potential between them. This *Debye screening* of free color charges in QGP prevent heavy quark $c\bar{c}$ pairs from binding into a charmonium state like J/ψ. Instead, they would couple with a lighter quark to make hadrons with open charm. The predicted result is a suppression of charmonium in heavy ion collisions [31, 32]. J/ψ suppression was found at the SPS by the NA38/NA50 Collaboration [33], it is qualitatively in agreement with QGP predictions and cannot be reproduced by final state rescattering of the J/ψ with a dense hadronic environment after hadronization.

3.3.4 Elliptic Flow

In section 3.1, during the description of the evolution of the fireball that goes through a deconfined phase of quarks and gluons, it was mentioned that the system expands collectively, in particular it does so perpendicular to the

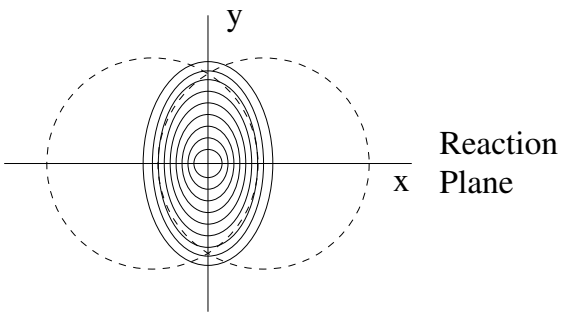

Figure 3.3: Initial overlap region in a non-central collision. The beam direction is perpendicular to the page.

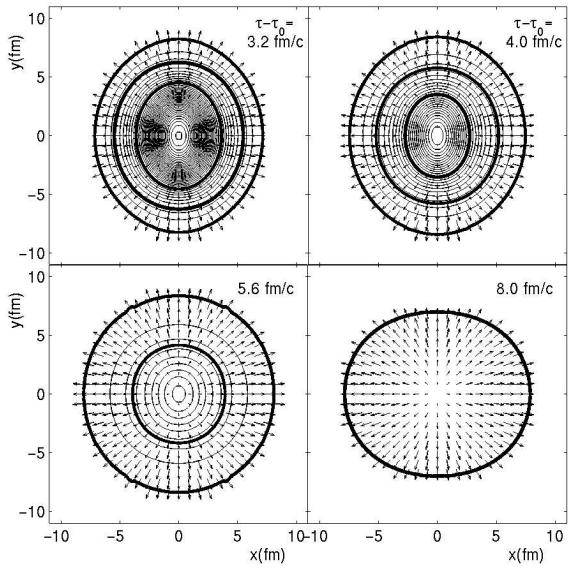

Figure 3.4: Time evolution of the energy density in a non-central collision.

beam direction in which the matter is initially at rest. This collective transverse flow is a consequence of the pressure gradient near the surface of the early collision fireball generated through rescattering that leads to a state of local thermal equilibrium. Although collective transverse flow does not necessarily imply a QGP phase, if QGP has been formed, collective transverse flow is an unavoidable consequence.

In the case of a non-central collision, like the one shown in Fig 3.3, the initial overlap region has an almond shape. If the produced matter thermalizes quickly, pressure builds up inside and the spatial deformation results in anisotropic pressure gradients that generate stronger collective flow in the shorter direction (in the reaction plane, the one formed by the bema axis and the vector between the center of the nuclei or impact parameter vector) than in the longer one (perpendicular to it) and the p_T distribution becomes anisotropic [34]. This anisotropy in momentum will reduce the initial spatial anisotropy as the source evolves with time as shown in Fig. 3.4 [35]. For this reason, it is believed that the final momentum anisotropy is primarily built up in the initial stages of the evolution [36].

This phenomenon is usually called *elliptic flow* and is measured by the second coefficient v_2 of the Fourier expansion of the p_T-spectrum [37]:

$$E\frac{d^3N}{d^3p} = \frac{1}{2\pi}\frac{d^2N}{p_T dp_T dy}\Big(1 + \sum_{n=1}^{\infty} 2v_n \cos(n(\varphi - \Psi_r))\Big), \tag{3.2}$$

where Ψ_r is the reaction plane angle and φ the azimuthal angle of the particle.

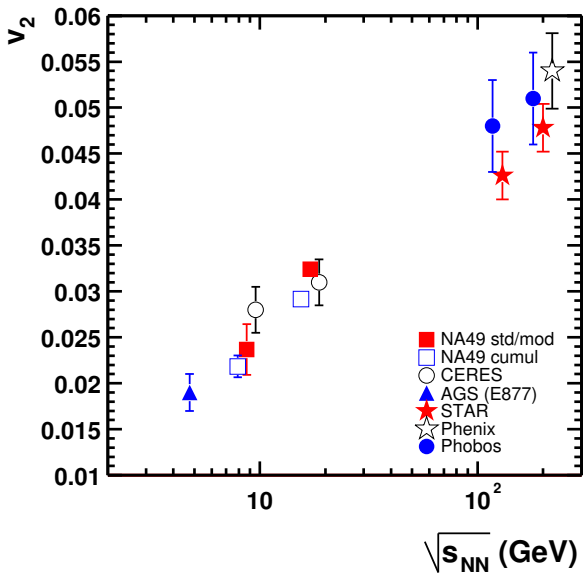

Figure 3.5: Integrated anisotropy parameter v_2 near mid-rapidity for mid-central events plotted vs. collision energy.

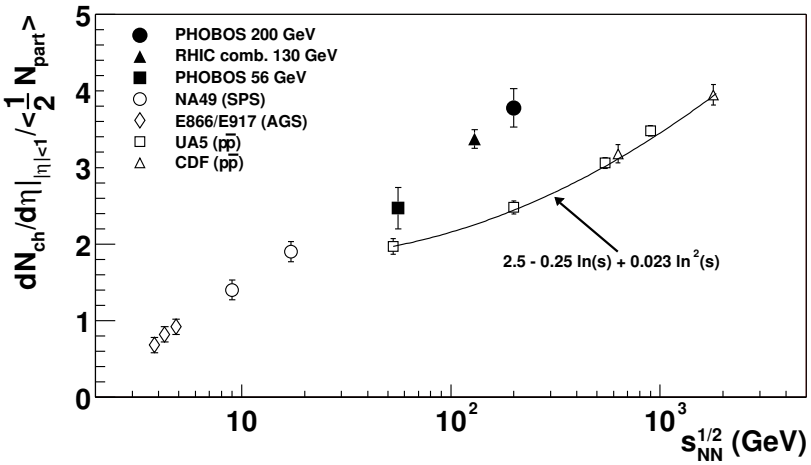

Figure 3.6: Energy dependence of the charged particle multiplicity near midrapidity for AuAu and pp collisions.

Figure 3.5 [38] shows the energy dependence of v_2 for charged particles near mid-rapidity. v_2 is positive and rising monotonically with the collision center of mass energy per nucleon.

3.4 Experimental results from RHIC

In this section, an overview of some of the most important measurements and results from RHIC is given. Detailed descriptions of the analysis are not given, nor are all the results covered, this section is just intended to give an idea of what the results from RHIC are telling us. Also, results related with two particle interferometry will be discussed later in this thesis.

3.4.1 Multiplicity

Multiplicity in heavy ion collisions tells us which fraction of the collision energy is inelastically transferred to secondary particles. One could try to calculate the multiplicity in nucleus-nucleus collisions as an incoherent superposition of independent nucleon-nucleon collisions which yields a multiplicity equal to the number of collisions times the multiplicity in NN collisions. From such calculation one would conclude that the AuAu multiplicity per participant pair should exceed NN multiplicity by a factor of 3. Instead, measured multiplicities at RHIC energies show a difference of only 50% percent as shown in Fig. 3.6 [39]. Given that inelastic scattering in the final state can only increase the multiplicity, this is an experimental proof that nuclear collisions at RHIC energies are not just an incoherent superposition of nucleus-nucleus collisions but instead there is a high degree of coherence in particle production [40].

3.4.2 Azimuthal anisotropy

Azimuthally anisotropic collisions in heavy ion were already introduced in section 3.3.4. The fact that the azimuthal anisotropy is quite sizeable at RHIC indicates the presence of collectivity. The latest results from RHIC show that not only the most abundant and light particles like pion, kaons or protons show this asymmetry but also the multi-strange baryons Ξ^- (dss) and Ω^- (sss) show a sizable anisotropy as shown by the parameter v_2 in Fig. 3.7 (left) [41]. Quark coalescence or recombination models [42, 43, 44], under the

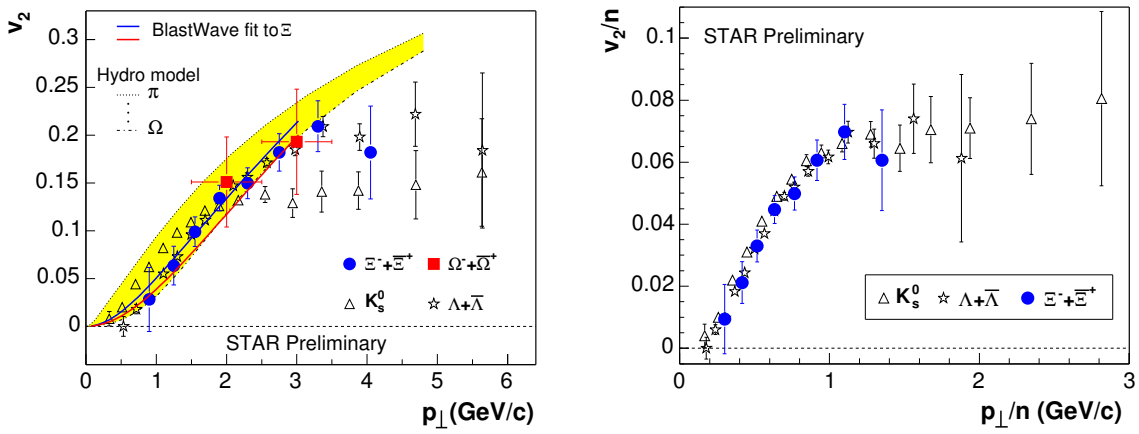

Figure 3.7: $v_2(p_T)$ for $\Xi^- + \bar{\Xi}^+$, $\Omega^- + \bar{\Omega}^+$, K^s_0 and $\Lambda^- + \bar{\Lambda}^+$ from minimum bias collisions (left). v_2/n as a function of p_T/n for $\Xi^- + \bar{\Xi}^+$, $\Omega^- + \bar{\Omega}^+$, K^s_0, where n is the number of constituent quarks for each particle (right).

assumption of partonic collectivity, predict a universal scaling of the elliptic flow parameter v_2 vs. p_T with the number of n constituents. Fig. 3.7 (right) shows the measured v_2 vs. p_T scaled by n [41]. These results agree with the predicted scaling which could be an indication of partonic collectivity at the early stage of the collision.

3.4.3 High p_T

In heavy ion collisions, large transverse momentum partons come from the initial hard scattering of nucleon constituents. These partons fragment and create a high energy cluster (jet) of particles. A high momentum parton traversing a dense colored medium experience substantial energy loss and may be absorbed [45, 46]. In the absence of effects in the nuclear medium the rate of hard processes should scale linearly with the number of binary

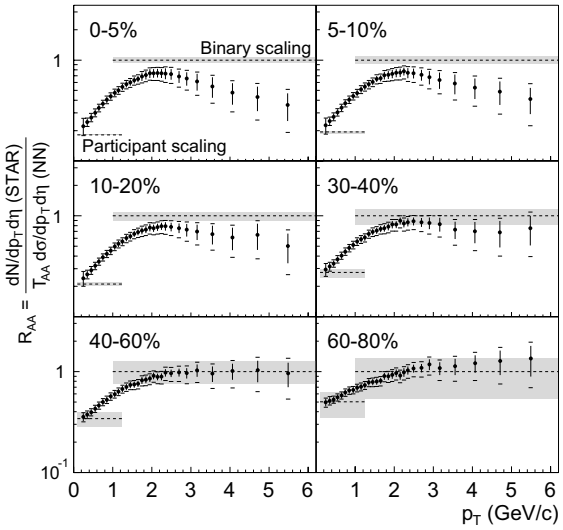

Figure 3.8: $R_{AA}(p_T)$ for various centrality bins, for AuAu relative to an NN reference spectrum.

nucleon-nucleon collisions. However, recent results from RHIC show a suppression of the single particle inclusive spectra of hadrons for $p_T > 2$ GeV/c in central AuAu collisions indicating substantial in-medium interactions as shown by $R_{AA}(p_T)$ in Fig. 3.8 [47]. This quantity gives us a comparison of spectra from AuAu collisions to an NN reference. A clear suppression is observed for $p_T > 2$ GeV/c for the most central collisions (0-5%, 5-10% and 10-20%).

The two particle azimuthal distribution of high p_T particles gives us more information on this. Two hadron angular correlations at large transverse momentum for AuAu collisions show a suppression of back-to-back relative to small-angle correlations in central AuAu collisions [48], Fig. 3.9 (b). This suppression is not observed in pp collisions even when the same mechanism

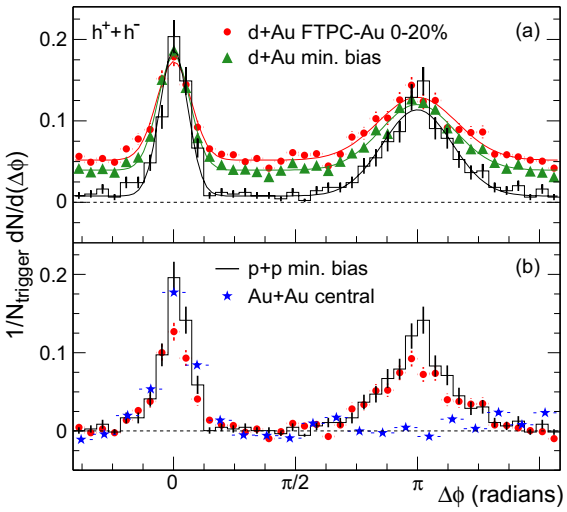

Figure 3.9: (a) Azimuthal distributions for minimum bias and central dAu collisions, and for pp collisions. (b) Comparison of two-particle azimuthal distributions for central dAu to pp and AuAu collisions.

(hard parton scattering and fragmentation) is responsible for the high transverse momentum particle production in pp and AuAu collisions. If the suppression is the result of initial-state effect, then it should also be observed in dAu collisions. However, no suppression is observed in dAu collisions, Fig. 3.9 (a) [49], from which one concludes that the suppression in central AuAu collisions is due to final state interactions with the dense system generated in the collision.

3.5 In this thesis

The porpoise of the analysis presented in this thesis is to study the space-time structure of the particle emitting source at freeze-out. We will also extract dynamical information on the evolution of the collision to freeze-out; we will study how much the source expands from the initial stage to freeze-out and we will discuss its relation with the initial energy density gradient.

CHAPTER 4

TWO-PARTICLE INTENSITY INTERFEROMETRY

To study the dynamical evolution and the space-time structure of the particle emitting source at freeze-out we use the two particle interferometry technique. In this chapter a theoretical overview of this technique and its application in heavy ion collisions are given.

4.1 HBT Interferometry

Two-particle intensity interferometry gives access to the space-time geometry of particle emitting sources. This technique was developed in the early 1950's by R. Hanbury Brown and R.Q. Twiss [50] who used it to measure the angular size of stellar objects. Because of their pioneering work, this method is commonly called HBT interferometry. It differs from ordinary amplitude interferometry in that it compares intensities, rather than amplitudes, at different points.

The first application of this technique to particle physics was by Goldhaber et al. [51] who extracted the spatial extend of the source in proton-antiproton annihilations from two pion correlations. The method exploits the

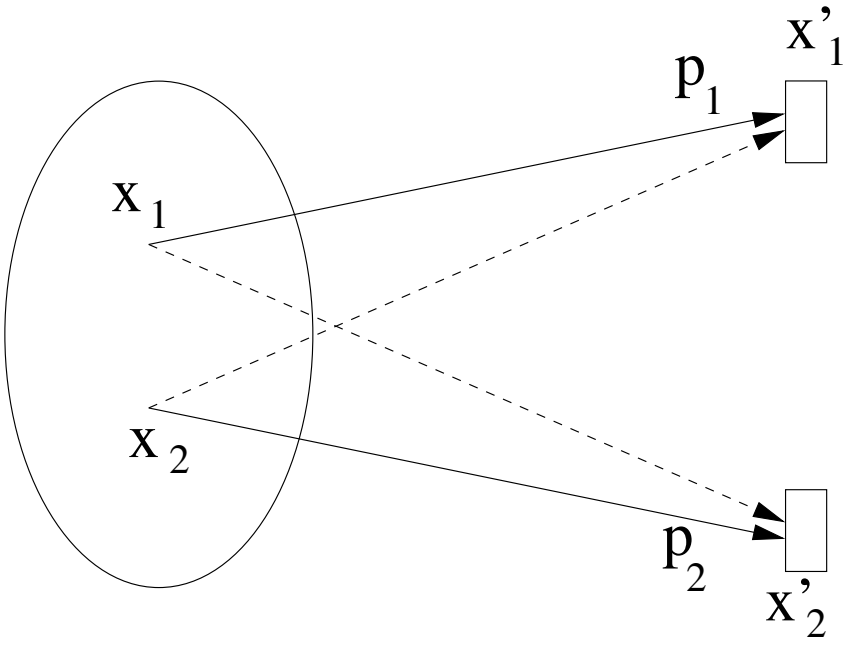

Figure 4.1: Basic HBT diagram.

fact that identical bosons (fermions) should satisfy the Bose-Einstein (Fermi-Dirac) statistics, therefore, for bosons (fermions) the two particle distribution should show an enhancement (suppression) at small relative momentum between the particles.

The basic diagram for an HBT experiment is shown in Fig. 4.1, where we have a source characterized by the emission function $S(x,p)$. For this first derivation, this emission function can be viewed as the probability that a particle with momentum p is emitted from the space-point x in the collision region, so that the total probability of emitting one particle with momentum p

is the integral over the whole source:

$$P(\vec{p}) = \int d^4x S(x,p)|_{p_0=E_p}. \tag{4.1}$$

The emission function must be evaluated on-shell, *i.e.* $p^0 = E_p = (m^2 + \vec{p}^{\,2})^{1/2}$.

If the source in Fig. 4.1 emits two identical particles from positions x_1 and x_2, with momenta p_1 and p_2 that are measured at positions $x_1^{'}$ and $x_2^{'}$, in an ideal case with no final state interaction, the wave function for the two particles is:

$$\Psi = \frac{1}{\sqrt{2}}[e^{i(x_1^{'}-x_1)p_1}e^{i(x_2^{'}-x_2)p_2} \pm e^{i(x_1^{'}-x_2)p_1}e^{i(x_2^{'}-x_1)p_2}]. \tag{4.2}$$

The fact that they are identical particles implies that we cannot distinguish between them, therefore, the wave function needs to be symmetrized for the case of bosons or anti-symmetrized for the case of fermions; the positive sign (+) is for bosons and the negative one (-) for fermions. This is also the probability density for measuring such a state.

Then the probability of measuring two particles with momenta p_1 and p_2 in our detector would be the squared of the wave function integrated over the whole source, which, for completely incoherent emission, is:

$$P(\vec{p_1},\vec{p_2}) = \int d^4x_1 d^4x_2 S(x_1,p_1)S(x_2,p_2)|\Psi|^2. \tag{4.3}$$

Introducing Eq. (4.2) in Eq. (4.3),

$$\begin{aligned} P(\vec{p_1},\vec{p_2}) &= \int d^4x_1 S(x_1,p_1) \int d^4x_2 S(x_2,p_2) \\ &\pm \int d^4x_1 d^4x_2 S(x_1,p_1)S(x_2,p_2)\cos((p_1-p_2)(x_1-x_2)). \end{aligned} \tag{4.4}$$

Assuming that the emission function has a smooth momentum dependence, it satisfies:

$$S(x_1,p_1)S(x_2,p_2) = S(x_1,k+\frac{1}{2}q)S(x_2,k-\frac{1}{2}q) \approx S(x_1,k)S(x_2,k), \tag{4.5}$$

where q and k are the relative and average pair momentum respectively. This is the so called *smoothness approximation* [52] and it is only valid for small relative momentum.

If one defines the variables $x = x_1 - x_2$ and $X = \frac{1}{2}(x_1 + x_2)$, using the smoothness approximation and Eq. (4.1), the two-particle probability can be expressed as,

$$P(\vec{p}_1,\vec{p}_2) = P(\vec{p}_1)P(\vec{p}_2) \pm \int d^4x\ \cos(qr) \cdot \int d^4X\ S(x+\frac{X}{2},k)S(x-\frac{X}{2},k), \tag{4.6}$$

where r is the relative separation and the term $\int d^4X\ S(x+\frac{X}{2},k)S(x-\frac{X}{2},k) = d(x,k)$ is the so-called relative distance distribution [52].

Then, the two-particle correlation function, defined as the ratio of the two-particle probability divided by the product of the single-particle probabilities, is given by

$$C(\vec{q},\vec{k}) = \frac{P(\vec{p}_1,\vec{p}_2)}{P(\vec{p}_1)P(\vec{p}_2)} \approx 1 \pm \frac{\int d^4x \cos(qr) d(x,k)}{\left|\int d^4x S(x,k)\right|^2}, \tag{4.7}$$

where we have used the smoothness approximation in the denominator to get the last term of the equation. Because the two measured particles are on-shell, $p^0_{1,2} = E_{1,2} = (m^2 + \vec{p}^{\,2}_{1,2})^{1/2}$, the four-momenta q and k are off-shell. They satisfy the orthogonality relation $k_\mu q^\nu = (m_1^2 - m_2^2)/2$ that would be zero only in the case of same mass particles. The *on-shell approximation* [52] $k^0 \approx E_k =$

$(m^2 + \vec{k}^2)^{1/2}$ is needed on the right-hand side of Eq. (4.17) in order to evaluate $S(x,k)$.

With the mass-shell constraint written in the form $q^0 = \vec{\beta} \cdot \vec{q}$, Eq. 4.7 can be rewritten as:

$$C(\vec{q},\vec{k}) = 1 \pm \frac{\int d^3x \cos(\vec{q}\vec{x}) \int dt d(\vec{x} + \vec{\beta}t, k)}{\left| \int d^4x S(x,p) \right|^2} = 1 \pm \frac{\int d^3x \cos(\vec{q}\vec{x}) S_{\vec{k}}(\vec{x})}{\left| \int d^4x S(x,p) \right|^2}, \qquad (4.8)$$

where $S_{\vec{k}}(\vec{x})$ is known as the "relative source function" [52].

The above derivation of the correlation function illustrates the basic ideas of the two particle intensity interferometry technique, however it has its limitations. The time structure of the source is completely integrated so that it is impossible to reconstruct the space-time of the source from the correlation function. This comes from the fact that the Wigner function $S(x,k)$ is taken as the phase-space probability density.

An alternative derivation for the two particle correlation function is as follows. The quantum state $|\phi>$ that describes the particle under consideration emitted from the source is calculated by solving the Klein-Gordon equation:

$$(\nabla^2 + m^2)\phi(x) = J(x), \qquad (4.9)$$

where m is the mass of the particle, $J(x)$ is the nuclear current operator acting as the source of pions, and $\phi(x)$ is the pion field.

The solution to this equation can be written as [53],

$$|\phi> = 2^{-n/2} \exp\left(i \int d^3p J(\vec{p}) a^+(\vec{p}) \right) |0>, \qquad (4.10)$$

where $J(\vec{p})$ is the Fourier transform of $J(\vec{x})$, $n = \int d^3p |J(\vec{p})|^2$, and a_p^+ is the creation operator.

$|\phi>$ has the property that it is an eigenstate of the annihilation operator [54],

$$a_p|\phi>= i\int d^4x \frac{e^{ipx}}{\sqrt{2E_p(2\pi)^3}} J(x)|\phi> . \tag{4.11}$$

Using the creation and annihilation operator, the single particle production probability is given by

$$P(\vec{p}) =< \phi|a_p^+ a_p|\phi >= \int d^4x S(x,p), \tag{4.12}$$

and the pair production probability is given by

$$P(\vec{p}_1,\vec{p}_2) =< \phi|a_{p_1}^+ a_{p_2}^+ a_{p_2} a_{p_1}|\phi > . \tag{4.13}$$

If one assumes chaotic particle emission, the expectation in Eq. (4.13) can be expanded using the Wick theorem [55]

$$\begin{aligned} &< \phi|a_{p_1}^+ a_{p_2}^+ a_{p_2} a_{p_1}|\phi >= \\ &< \phi|a_{p_1}^+ a_{p_1}|\phi >< \phi|a_{p_2}^+ a_{p_2}|\phi > \pm < \phi|a_{p_1}^+ a_{p_2}|\phi >< \phi|a_{p_2}^+ a_{p_1}|\phi >, \end{aligned} \tag{4.14}$$

where once more the positive (+) sign is for bosons and the negative (-) one is for fermions. This expansion can be viewed as the sum of probabilities of particles being emitted from two points taking into account the required symmetrization (anti-symmetrization). Then the pair production probability can be expressed as:

$$\begin{aligned} P(\vec{p}_1,\vec{p}_2) &= \int dx_1 S(x_1,p_1)\int dx_2 S(x_2,p_2) \\ &\pm \int dx_1 S\Big(x_1,\frac{p_1+p_2}{2}\Big)e^{i(p_1-p_2)x_1}\int dx_2 S\Big(x_2,\frac{p_1+p_2}{2}\Big)e^{i(p_1-p_2)x_2} \\ &= \int dx_1 S(x_1,p_1)\int dx_2 S(x_2,p_2) \pm \Big|\int dx S(x,k)e^{iqx}\Big|^2, \end{aligned} \tag{4.15}$$

and the correlation function is given by:

$$C(\vec{p}_1,\vec{p}_2)=\frac{P(\vec{p}_1,\vec{p}_2)}{P(\vec{p}_1)P(\vec{p}_2)}=1\pm\frac{\left|\int d^4xS(x,k)e^{iqx}\right|^2}{\int d^4x_1S(x_1,p_1)\int d^4x_2S(x_2,p_2)}. \tag{4.16}$$

Using the smoothness approximation in the denominator, the correlation function can then be expressed in terms of the relative and average momenta of the pair as

$$C(\vec{q},\vec{k})=1\pm\left|\frac{\int d^4xS(x,k)e^{iqx}}{\int d^4xS(x,k)}\right|^2. \tag{4.17}$$

The on-shell approximation is needed on the right-hand side of Eq. 4.17 in order to evaluate $S(x,k)$. The corrections due to this approximation are of order $\vec{q}/8E_k^2$ [56], which, for the range of $\vec{q}$ in which we are interested, are very small.

4.2 Final state interactions

The derivation of the two particle correlation function described above assumes no final state interactions. However, most HBT measurements in heavy ion collisions are performed with charged particles. These particles suffer long range Coulomb interaction effects on the way from the source to the detector, which for like-sign (unlike-sign) particles cause a suppression (enhancement) of the measured correlation function at low $\vec{q}$. These particles also feel the total electric charge of the source from which they are emitted. There is also a strong interaction between outgoing particles, which plays a very important role in proton-proton correlations due to the strong s-wave resonance in the two nucleon channel just above threshold. These final state

interactions will affect the correlation function and need to be taken into account in order to isolate the Bose-Einstein (Fermi-Dirac) interference effects.

In the case of the correlation function for particles under study in this thesis, like-charged pions, only Coulomb interaction between the outgoing particles plays an important role. The strong interaction between these particles is very weak. A repulsive s-wave interaction exists for the I=2 $\pi\pi$ system. However, the range of this interaction is estimated to be $\sim$ 0.2 fm [57], while the characteristic separation between pions produced in relativistic heavy-ion collisions is $\sim$ 5 fm. Also, there are no doubly charged mesonic resonances that could decay into same charged pions that would strong interact. For these reasons, the strong interaction will be ignored for like sign particles.

In the following, the discussion will be exclusively for bosons, since the particles used for the analysis presented in this thesis are pions.

4.2.1 Coulomb interaction

The fact that the two charged particles Coulomb interact on the way from the source to the detector implies that the particles do not propagate as plane waves. In order to account for the Coulomb interaction, it is possible to either include the interaction in the theoretical calculation described above or to take it into account when calculating the experimental correlation function. In this analysis the latter one is used. Isolating Bose-Einstein interference effects from Coulomb interaction is not easy because both interactions are of

similar size and affect the two-particle correlation in similar relative momentum scales.

In order to calculate the Coulomb interaction effects in the correlation function one proceeds as follows. The Schrödinger equation for the Coulomb wave function is [58]:

$$(-\frac{\nabla}{2\mu} - E + \frac{e^2}{r})\psi_c(\vec{q},\vec{r}) = 0, \tag{4.18}$$

where $r = |\vec{r}|$ is the relative coordinate, $E = \frac{q^2}{2\mu}$ is the energy of the particle in the center of mass system, μ is the reduced mass, and e is the electromagnetic coupling strength.

The solutions of this equation, written in terms of the confluent hypergeometric function F, are [59]:

$$\psi_c(\vec{q},\vec{r}) = \Gamma(1+i\eta_\pm)e^{-\frac{1}{2}\vec{q}\cdot\vec{r}}F(-i\eta;1;z_\pm), \tag{4.19}$$
$$z_\pm = \frac{1}{2}(qr \pm \vec{q}\cdot\vec{r}) = \frac{1}{2}qr(1\pm\cos\theta).$$

Here, θ denotes the angle between $\vec{r}$ and $\vec{q}$. The Sommerfeld parameter depends on the particle mass m and e:

$$\eta_\pm = \pm\frac{e^2}{4\pi}\frac{\mu}{q/2} = \pm\frac{me^2}{4\pi q}, \tag{4.20}$$

and the minus (plus) sign is for pairs of like-sign (unlike-sign) particles.

The symmetrized Coulomb wave function is:

$$\psi_r(\vec{q},\vec{r}) = \frac{1}{\sqrt{2}}(\psi_c(\vec{q},\vec{r}) + \psi_c(\vec{q},-\vec{r})). \tag{4.21}$$

Then the contribution from Coulomb interaction to the correlation function can be calculated as:

$$P_c(\vec{p}_1, \vec{p}_2) = \frac{1}{2} \int d^3r \rho(\vec{r}) |\psi_r(\vec{q}, \vec{r})|^2. \tag{4.22}$$

Here $\rho(\vec{r})$ is the source function or the distribution of the average distance between the particles in each pair as they are emitted. This expression is then integrated numerically to calculate the Coulomb wave contribution to the correlation function [59]. However, experimentally, the source function is not known in advance so one must make some approximations.

In the point-source approximation [53] traditionally used, $\rho(\vec{r}) \simeq \delta^3(x)$ and the Coulomb part of the correlator is given by the Gamow factor $G(\eta)$,

$$G(\eta) = |\varphi_c(0)|^2 = \frac{2\pi\eta}{e^{2\pi\eta} - 1}. \tag{4.23}$$

However, in heavy-ion collisions, in which the emitting source has a finite size, this approximation largely overestimates the Coulomb interaction effects since particles are emitted with finite separation which leads to a weaker Coulomb interaction.

An improved procedure is to calculate the interaction for a finite size static source by approximating the source function to a spherical Gaussian of a given radius and then integrating (4.22) [59, 58, 60]. This is the procedure followed in the analysis presented here, in which the values for the integrated Coulomb wave function were tabulated according to the assumed source size and the Sommerfeld factor. From now on, the integrated wave Coulomb function over a spherical Gaussian source will be called K_{coul}, it depends on q_{inv} and the

radius R of the Gaussian, and is given by:

$$K_{\text{coul}}(q_{\text{inv}}) = \int d^3r \rho(\vec{r}) |\psi_r(\vec{r}, \vec{q})|^2, \tag{4.24}$$

where $\rho(\vec{r}) \propto \exp(-\vec{r}/4R^2)$. The experimental application of this Coulomb factor will be discussed in Chapter 6.

As already mentioned, in addition to the Coulomb interaction between the outgoing particles, the emitted particles feel the positively charged source. The effects of this interaction on the pion correlation function was found to be very small and decreases as the collision energy becomes ultrarelativistic [61, 62]. Therefore, we do not apply any correction to the data due to the central Coulomb potential. The experimental validness of this will be discussed in Chapter 6.

4.3 Gaussian parametrization

In order to extract information from the experimentally measured correlation function about the space-momentum geometry of the source, the emission function can be approximated by a Gaussian [63, 64, 65]:

$$S(x,k) \approx S(\bar{x}(k),k) \exp[-\frac{1}{2}\tilde{x}^{\mu}(k) B_{\mu\nu}(k) \tilde{x}^{\nu}(k)], \tag{4.25}$$

where the space time coordinates $\tilde{x}^{\mu}$ are defined relative to the "effective source center" $\bar{x}(k)$ for bosons emitted with momenta k:

$$\tilde{x}^{\mu}(k) = x^{\mu} - \bar{x}^{\mu}(k) \qquad \bar{x}^{\mu}(k) = < x^{\mu} > (k), \tag{4.26}$$

where $< ... >$ denotes an average with the emission function:

$$< f > (k) = \frac{\int d^4x f(x) S(x,k)}{\int d^4x S(x,k)}, \tag{4.27}$$

and the choice $(B)^{-1}_{\mu\nu}(k) =< \tilde{x}_\mu \tilde{x}_\nu > (k)$ ensures that the Gaussian in (4.25) has the same RMS widths in space-time as the full emission function.

Inserting Eq. (4.25) in Eq. (4.17), the correlation function takes a Gaussian form:

$$C(\vec{q}, \vec{k}) = 1 + \exp(-q_\mu q_\nu < \tilde{x}_\mu \tilde{x}_\nu > (k)). \tag{4.28}$$

Since the correlation function depends only in relative distances $\tilde{x}^\mu$, no information can be obtained about the center of emission. Instead, these width parameters measure the widths of the distribution of particles in the system from which particle pairs with momentum k are most likely to be emitted. $< \tilde{x}_\mu \tilde{x}_\nu >$ coincide with the width of the total source only in the special case in which the emission function does not contain space-momentum correlations and factorizes as $S(x, k) = f(x)g(k)$. This will be discussed later in more detail.

4.3.1 Other contributions to the correlation function

Several effects can reduce or modify the experimentally measured correlation function. Equation (4.28) has been calculated assuming a complete chaotic emission. Pions emitted from the same coherent state or wave packet do not exhibit interference effects [53], therefore, for a complete coherent emission, the measured correlation function would be unity for all values of q when properly normalized. In general, the emission of particles is neither perfectly chaotic nor completely coherent, which will reduce the strength of the correlation function reducing its intercept point at $q = 0$ [59]. In principle

this can be taken into account by adding a new parameter, λ, to the correlation function, which, in general, depends on k:

$$C(q,k) = 1 + \lambda(k)\exp(-q_\mu q_\nu < \tilde{x}_\mu \tilde{x}_\nu > (k)). \tag{4.29}$$

This λ parameter should be unity for a fully chaotic source and smaller than unity for a source with partially coherent particle emission. This is probably not the best way of taking non-chaotic emission into account [66]. In the analysis presented here we have assumed completely chaotic emission and expect λ to take care of the possible small deviation from it.

In practice, however, there are many reasons why deviations from $C(q = 0, k) = 2$ may be observed. For example, contribution from pions coming from long-lived resonances, that lead to an extended source, modify the shape of the correlation function changing the intercept point at $q = 0$. Misidentified particles, such as electrons, in our pion sample that reduce the strength of the correlation, reducing the enhancement at low relative momentum and thus reducing the intercept point at $q = 0$. Or final state interaction not properly taken into account, such as Coulomb interaction that will also reduce the enhancement and therefore λ, or attractive strong interaction that would lead to a false stronger enhancement.

4.4 Coordinate parametrization

One must also choose a coordinate system in which to work, to extract information from the experimental two-particle correlator.

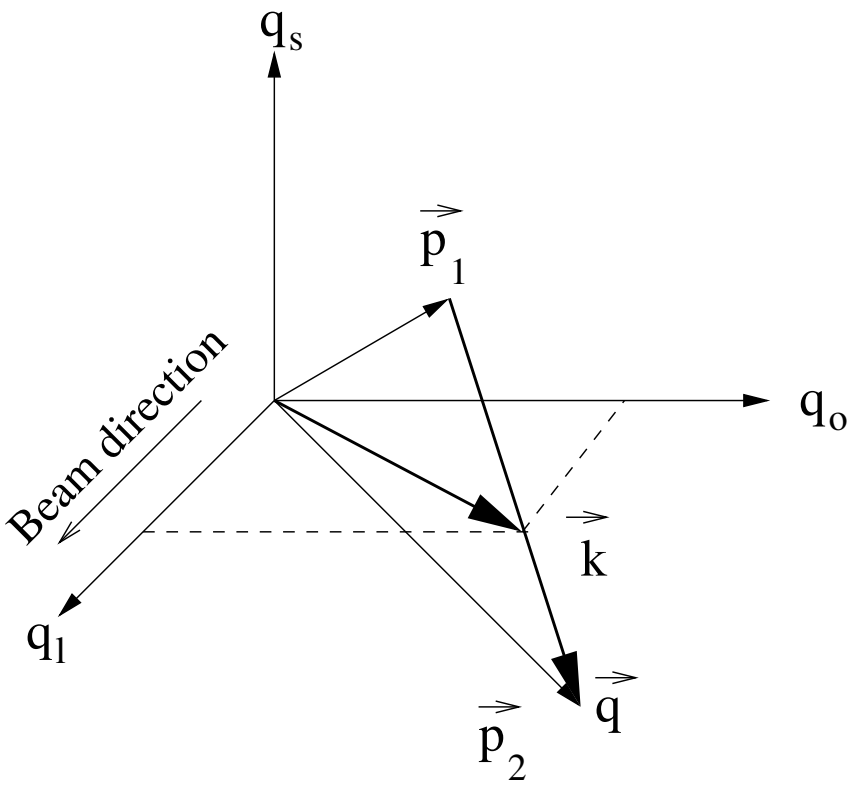

Figure 4.2: Cartesian or Bertsch-Pratt (osl) parametrization.

A commonly used 1-dimensional parametrization is

$$C(\vec{q},\vec{k}) = 1 + \lambda(\vec{k})\exp(-q_{\text{inv}}^2 R_{\text{inv}}^2(\vec{k})), \tag{4.30}$$

in which all the spatial and temporal information of the source is contained in R_{inv}. However, this parameter does not represent any physical extension of the source.

A 3-dimensional parametrization that will allow to get information of the source in the beam, and transverse directions is the Cartesian or Bertsch-Pratt ("$out-side-long$") parametrization [54, 67, 68, 69], shown in Fig. 4.2. In this parametrization, the relative momentum vector of the pair $\vec{q}$ is decomposed into a longitudinal direction along the beam axis, q_l, an outward direction parallel to the pair transverse momentum, q_o, and a sideward direction perpendicular to those two, q_s. Using the on-shell approximation the component of the 4-vector momentum q^0 can be expressed as $q^0 = \vec{\beta}\cdot\vec{q}$.

The correlation function in this parametrization is expressed by:

$$C(\vec{q},\vec{k}) = 1 + \lambda(\vec{k})\exp(-\sum_{i,j=o,s,l} R_{ij}^2(\vec{k})q_i q_j). \tag{4.31}$$

The Gaussian parameters, or HBT radii, R_{ij} are related to the space time variances of the emission function by:

$$R_{ij}^2(\vec{k}) = <(\tilde{x}_i - \beta_i\tilde{t})(\tilde{x}_j - \beta_j\tilde{t})>(\vec{k}) \qquad i,j = o,s,l. \tag{4.32}$$

For an azimuthally integrated analysis, the emission function has a reflection symmetry $x_s \to -x_s$ and the correlator is symmetric under $q_s \to -q_s$. Then $R_{os}^2 = R_{sl}^2 = 0$ and the correlator can be expressed as:

$$C(\vec{q},\vec{k}) = 1 + \lambda(\vec{k})\exp(-R_o^2(\vec{k})q_o^2 - R_s^2(\vec{k})q_s^2 - R_l^2(\vec{k})q_l^2 - 2R_{ol}^2(\vec{k})q_o q_l). \tag{4.33}$$

If one now chooses as the reference frame, the longitudinal comoving system (LCMS) frame of the pair, in which the source is symmetric under $x_l \rightarrow -x_l$ at midrapidity, the only cross-term left also vanishes and the two-particle correlation function is given by:

$$C(\vec{q},\vec{k}) = 1 + \lambda(\vec{k}) \exp(-R_o^2(\vec{k})q_o^2 - R_s^2(\vec{k})q_s^2 - R_l^2(\vec{k})q_l^2), \tag{4.34}$$

where the HBT radii measure the spatial and temporal extend of the collision system at freeze-out:

$$\begin{aligned} R_o^2(k) &= <(\tilde{x} - \beta_T\tilde{t})^2>(k) \\ R_s^2(k) &= <\tilde{y}^2> \\ R_l^2(k) &= <\tilde{z}^2>, \end{aligned} \tag{4.35}$$

here, $\beta_T = k_T/k_0$ is the transverse pair velocity.

Note that only $R_o^2(k)$ carries temporal information. By comparing $R_o^2(k)$ to $R_s^2(k)$ emission duration scales can be, in principle, extracted.

The azimuthally sensitive analysis, in which the not azimuthally symmetric collision is studied from different angles Φ, will not be discussed in this thesis, however it will be used to calculate systematic errors, so we will introduce the basis here. For a detail description of this analysis refer to [70].

In such analysis, the emission function does not have a reflection symmetry $x_s \rightarrow -x_s$ and so the correlator is not symmetric under $q_s \rightarrow -q_s$, working on the LCMS frame, and without knowledge of the first-order reaction plane (due to detector limitations), the Gaussian parametrization becomes [71]

$$C(\vec{q}) = 1 + \lambda \exp(-R_o^2(\vec{k})q_o^2 - R_s^2(\vec{k})q_s^2 - R_l^2(\vec{k})q_l^2 - 2R_{os}^2(\vec{k})q_o q_s). \tag{4.36}$$

While for the azimuthally integrated analysis the sign of the q components is arbitrary, in the azimuthally-sensitive analysis, the sign of R^2_{os} is important because it tells us the azimuthal direction of the emitted particles, so the signs of q_o and q_s are kept and particles in every pair are ordered such that $q_l > 0$.

References [52, 72] give a detailed description of the relation between the HBT radius parameters and the space-time geometry of the final freeze-out stage for this analysis.

For a boost-invariant system, the Φ dependence of the HBT radii of Eq. (4.36) can be written as [71]:

$$\begin{aligned} R^2_o(k_T,\Phi) &= R^2_{o,0}(k_T) + 2\sum_{n=2,4,6\cdots} R^2_{o,n}(k_T)\cos(n\Phi) \\ R^2_s(k_T,\Phi) &= R^2_{s,0}(k_T) + 2\sum_{n=2,4,6\cdots} R^2_{s,n}(k_T)\cos(n\Phi) \\ R^2_l(k_T,\Phi) &= R^2_{l,0}(k_T) + 2\sum_{n=2,4,6\cdots} R^2_{l,n}(k_T)\cos(n\Phi) \\ R^2_{os}(k_T,\Phi) &= 2\sum_{n=2,4,6\cdots} R^2_{os,n}(k_T)\sin(n\Phi), \end{aligned} \tag{4.37}$$

where $R_{\mu,n}(k_T)$ (for $\mu = o,s,l,os$, and $n = 0,2,4...$) are the n^{th} order Fourier coefficients. These coefficients, that are Φ independent, can be calculated as:

$$R^2_{\mu,n}(k_T) = \begin{cases} \langle R^2_\mu(k_T,\Phi)\cos(n\Phi)\rangle_\Phi & (\mu = o,s,l) \\ \langle R^2_\mu(k_T,\Phi)\sin(n\Phi)\rangle_\Phi & (\mu = os) \end{cases}$$

The 0^{th} order Fourier coefficients correspond to the extracted HBT radii in an azimuthally integrated analysis. In this analysis, Fourier coefficients for 4^{th} order and above are consistent with 0.

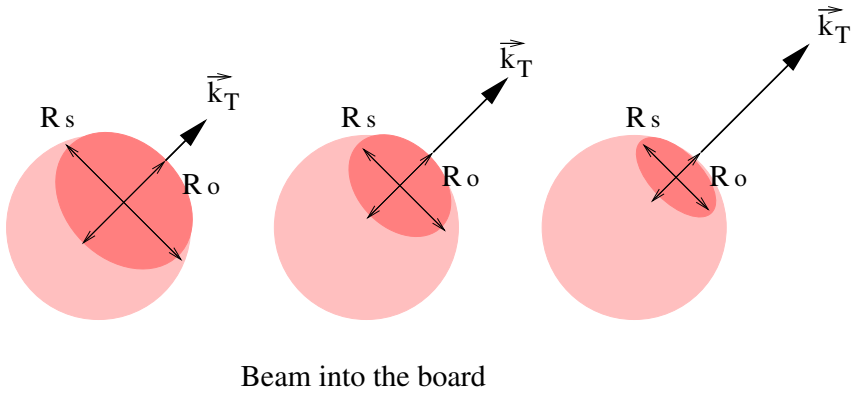

Figure 4.3: Homogeneity regions for different pair momenta.

4.5 HBT in dynamical systems

As already mentioned, the space-time variances $< \tilde{x}_\mu \tilde{x}_\nu > (k)$ in Eq. (4.29), and therefore the HBT radii $R_i(\vec{k})$ in Eq. (4.34), depend on the total momentum of the pair. This is because the particle momenta are correlated with their emission points (space-momentum correlations). In heavy-ion collisions, this is produced mainly by the collective expansion of the source. Also, thermalized sources may exhibit temperature gradients, causing additional space-momentum correlations. Low momentum pions from the decay of long-lived resonances that usually come from a larger space-time region may also generate space-momentum correlations.

Therefore, the HBT radii measure the size of the regions emitting particles of a given momenta, the so called *regions of homogeneity* [73], as shown in the sketch in Fig. 4.3. For an expanding source, depending on the direction and

the modulus of the momenta of the pairs of particles entering the correlation function, different parts of the source are measured. The center of a region of homogeneity $< \bar{x}_\mu >$ depends also on k and lies, typically, between the center of the collision region and the observer.

Also, the sizes of these regions of homogeneity are controlled by the expanding velocity gradient [72, 74, 75], therefore, the dependence of the HBT radii on the pair momenta, contains dynamical information of the particle emitting source [54, 73].

4.6 Hydrodynamic predictions

In heavy-ion collisions, during a finite time interval between hadronization and thermal freeze-out, and under certain conditions, the system can be described as an ideal (non-viscous) fluid by a hydrodynamical model [53, 76, 77, 78].

A hydrodynamic model is fully specified by the equation of state and the initial conditions; and its evolution is ended by implementing freeze-out conditions.

One of the first hydrodynamic calculations [79], that assumed QGP formation and included HBT, predicted that the source would emit pions over a long time period resulting in a long lifetime of the source and so in a large contribution $\beta_T^2\langle\tilde{t}^2\rangle$ to the outward HBT radius in Eq. (4.35). As a consequence, the ratio R_o/R_s being much larger than unity was predicted as a clear signal of the QGP formation.

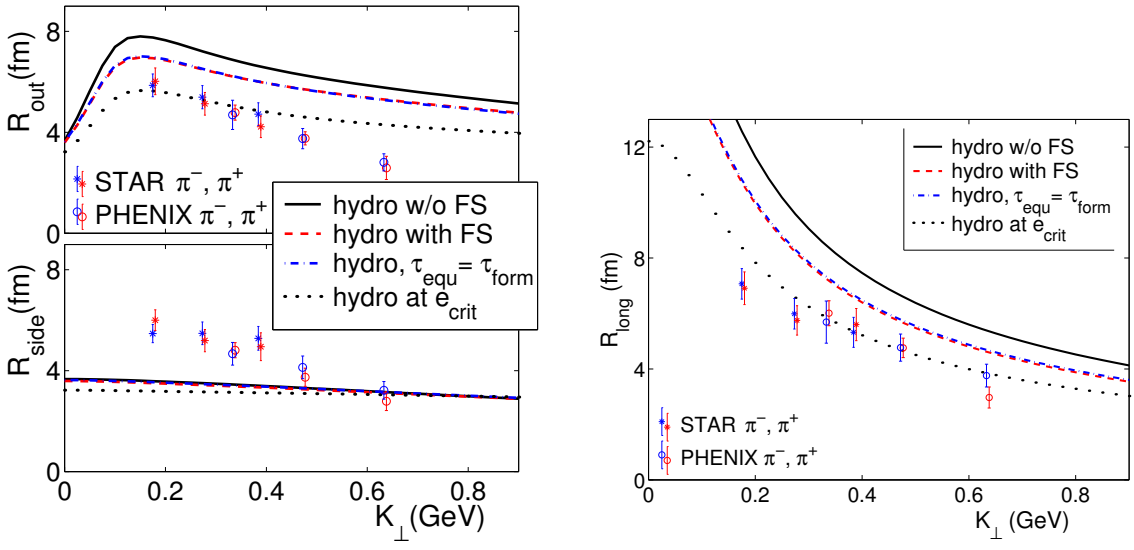

Figure 4.4: HBT radii from a hydrodynamic calculation compared with the experimental values at $\sqrt{s_{NN}}$ = 130 GeV from the STAR and PHENIX collaborations.

After the first results from RHIC at $\sqrt{s_{NN}}$ = 130 GeV came out, it was seen that these hydrodynamic calculations were in good agreement with the experimental measurements of the momentum structure of the emitting source and the elliptic flow, however they failed to describe the space-time distribution at freeze-out as given by the HBT results [77]. This was called the "HBT puzzle" at RHIC.

Figure 4.4 shows a comparison of the experimental data at $\sqrt{s_{NN}} = 130$ GeV/c [80, 81] with results from hydrodynamic calculations [77, 78]. A purely hydrodynamic description with default initial conditions (solid lines in Fig. 4.4) fails to describe the measured HBT radii. Clearly R_s is underestimated,

and R_o and R_l are overestimated by the model, also, the k_T dependence of R_o and R_s is too weak.

R_l is driven by the expansion dynamics via the longitudinal velocity gradient at freeze-out. For a boost invariant longitudinal flow profile, as the one assumed in this calculation, this gradient decreases with time as $1/\tau$, leading to a typical hydrodynamic freeze-out time of $\sim$ 15 fm/c. To reduce R_l, freeze-out must happen earlier or the boost invariance should be broken [77, 78].

The small measured ratio $R_o/R_s \leq 1$ might be explained by a strong positive $x-t$ correlation. Hydrodynamic models assume that particles emitted from a larger x are emitted earlier, leading to a negative $x-t$ correlation that makes the term $-\beta_T\langle\tilde{x}_0\tilde{t}\rangle$ in R_0 (4.35) positive leading to $R_o >> R_s$ [77, 78]. The positive $x-t$ correlation implies that particles emitted from larger x values decouple later.

Later in this thesis, evolution and emission times will be extracted from the HBT radii according to a blast wave parametrization [82]; the expansion of the source will be studied and some hints about the possible causes for the discrepancies between measurements and hydrodynamic calculations will be given.

4.7 Experimental construction of correlation function

As already discussed, the two-particle correlation function between identical bosons with momenta p_1 and p_2 is defined as the ratio of the two-particle

and one-particle distributions:

$$C_2(\vec{p}_1, \vec{p}_2) = \frac{P_2(\vec{p}_1, \vec{p}_2)}{P_1(\vec{p}_1) \cdot P_1(\vec{p}_2)}. \tag{4.38}$$

Experimentally, it is obtained from the ratio:

$$C(\vec{q}, \vec{k}) = \frac{A(\vec{q})}{B(\vec{q})}, \tag{4.39}$$

(normalized to unity at large $\vec{q}$). The numerator, $A(\vec{q})$, is formed from pairs in same events and represents the distribution of the two particle probabilities for the relative momentum of each pair. The denominator, $B(\vec{q})$, is formed by mixing particles in separate events and represents the single particle probabilities.

CHAPTER 5

THE STAR EXPERIMENT

STAR, a solenoidal detector based on particle tracking in a large time-projection chamber, with a large solid angle detection of particles, is one of the four experiments at RHIC. In this chapter, the collider complex is introduced and the STAR detector described.

5.1 The Relativistic Heavy Ion Collider

RHIC consists on two concentric rings that accelerate and store two counter-rotating hadron beams [83]. It is designed to collide the beams at six different intersection points located along their 3.8 km circumference. The top achievable energy for heavy ion beams (*i.e.* gold nuclei) is 100 GeV/u and that for protons is 250 GeV. Superconducting magnets (cooled to below 4.6 degrees Kelvin) are used in both rings to focus and guide the beams, and a radio frequency (rf) system is used to capture, accelerate and store the beams.

A diagram of the collider complex is shown in Fig. 5.1. The acceleration of the gold ion beams is as follows. Gold ions in a charge state Q = -1e are injected in the Tandem Van de Graaff where they are partially stripped of

Figure 5.1: RHIC complex

the electrons to a charge state Q = +12e, and then accelerated to 1 MeV/u in the second stage of the Tandem. After further stripping at the exit of the Tandem, gold ions are delivered to the Booster Synchrotron, with a charge state Q = +32e, where they are accelerated to 95 MeV/u. At the exit of the Booster, ions are stripped again to a charge state Q = +77e. They are then injected into the Alternating Gradient Synchrotron (AGS) where their energy is increased to 10.8 GeV/u. At the exit of the AGS, gold ions are fully stripped to the charge state Q = +79e. The ions are then transferred to RHIC, through the AGS-to-RHIC Beam Transfer Line, where they are accelerated to their final energy and stored for up to 10 hours.

There are four detectors around the ring [84]; two large detectors (STAR and PHENIX) and two smaller detectors (PHOBOS and BRAHMS). All of

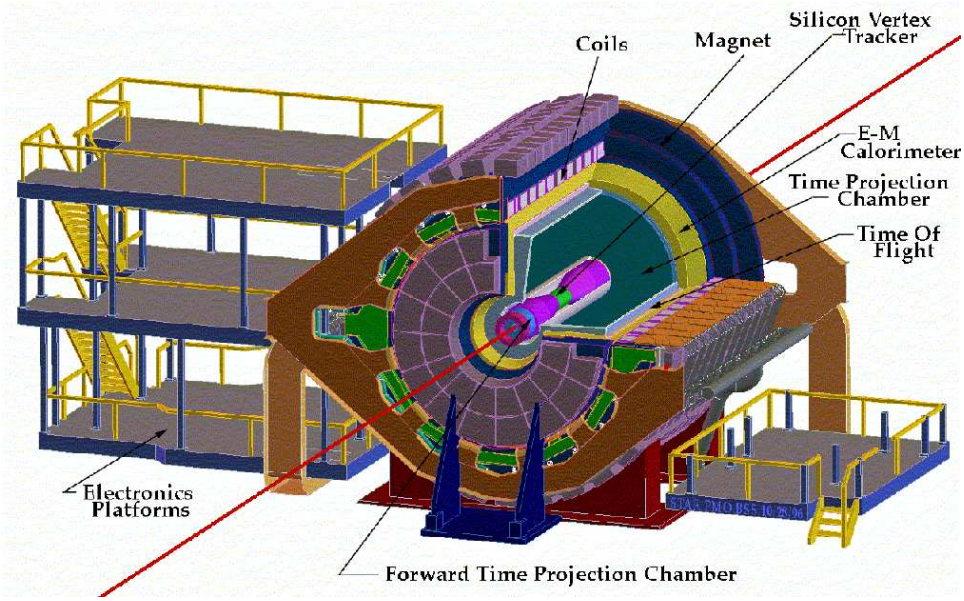

Figure 5.2: STAR detector with a cutaway for viewing the inner detectors.

them are primarily designed to measure the kinetic properties of relatively low-momentum particles in a very high density medium.

5.2 The STAR detector

The STAR detector is an azimuthally symmetric, large acceptance solenoidal detector designed primarily for measurements of hadron production over a large solid angle [85].

The layout of STAR as it was for Run-2 is shown in Figs. 5.2 and 5.3. It is located in a solenoidal magnet that provides a uniform magnetic field along the beam axis, of up to 0.5 Tesla, for charged particle momentum analysis [86]. The main tracking system is a large Time Projection Chamber (TPC).

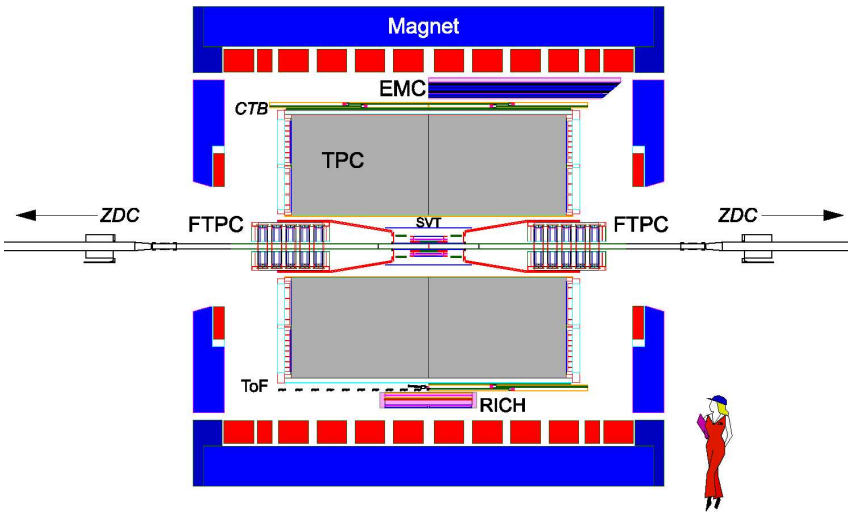

Figure 5.3: Side view of the STAR detector.

In addition, there are two other tracking detectors, a Silicon Vertex Detector (SVT) [87], located close to the beam pipe for the tracking of charged particles near the interaction point, and two forward TPCs (FTPCs) [88], for tracking of charge particles at large rapidity, $2.5 < |\eta| < 4$. Other active subsystems include, a Ring Imaging Cherenkov (RICH) [89] that extent particle identification at higher p_T, and about 10% of the full-barrel electromagnetic calorimeter [90] to measure photons, electrons, and the total transverse energy of events. The fast detectors that provide input to the trigger system are a central trigger barrel (CTB) that surrounds the outer cylinder of the TPC, and two zero-degree calorimeters (ZDC) located in the forward and backward directions.

5.2.1 The Time Projection Chamber

The TPC is the main tracking detector in STAR [91] and the only one used in the reconstruction of the events used in the analysis presented in this thesis. It records the tracks of particles, measures their momenta and identifies the particles by measuring their ionization energy loss ($\mathrm{d}E/\mathrm{d}x$), providing complete tracking for charged particles within $\pm$ 1.8 units of pseudorapidity through the full azimuthal angle ($\Delta\phi = 2\pi$) and over the full range of multiplicities up to $\sim 4 \cdot 10^3$ particles per event. Particles are identified over a momentum range from 100 MeV/c to around 1 GeV/c and momenta are measured over a range of 100 MeV/c to 30 GeV/c.

A TPC detector is a large 3 dimensional gas filled vessel in a well defined electric field. When a charged particle traverses the gas, it creates electron-ion pairs, that the electric field prevents from recombining, and the electrons drift quickly towards the readout chambers located at the ends of the TPC. The drift field is chosen so that it is not strong enough to create secondary electron-ion pairs.

The STAR TPC surrounds the beam-beam interaction region and its drift volume is limited by 2 concentric field cage cylinders, of radii 50 cm and 200 cm, and the end caps as shown in Fig. 5.4. It is 4.2 m long. It is filled with P10 gas (10% methane and 90% argon) at 2 mbar above the atmospheric pressure [92]. The main property of this gas is a fast drift velocity which peaks at a low electric field. There is a central membrane held at 28 kV that, together with the equipotential rings along the inner and outer field cage, create a uniform

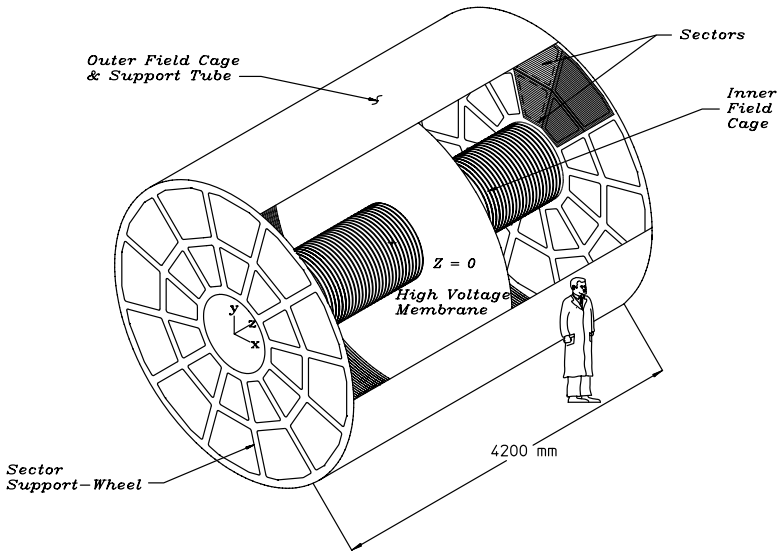

Figure 5.4: Section view of the STAR TPC showing the inner and outer field cages, the central membrana and the 12 sectors of each end cap.

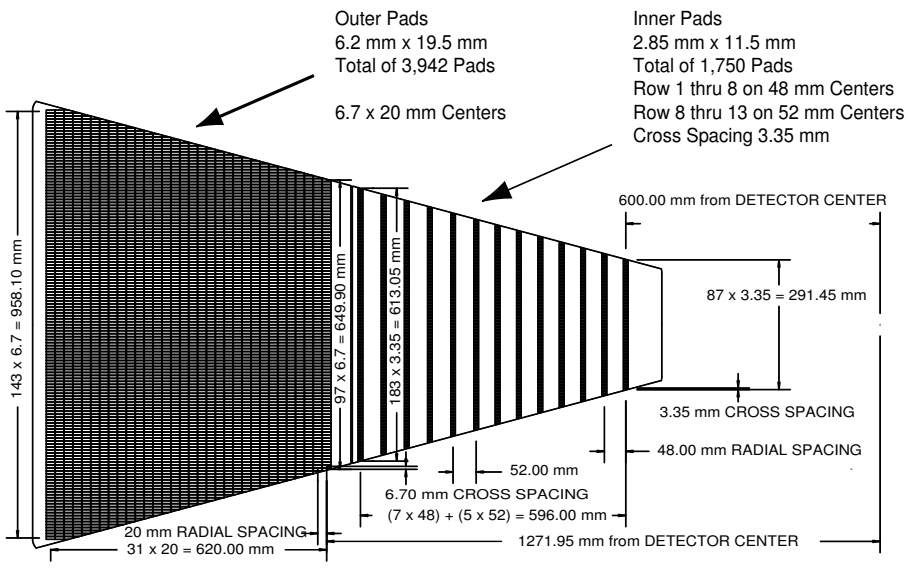

Figure 5.5: Distribution of pads in a STAR TPC sector.

drift field of 135 V/cm from the central membrane to the ground end caps where the readout chambers are located.

The readout system is based on Multi Wire Proportional Chambers (MWPC) with readout pads [93]. The readout pads are arranged in 12 sectors around the end caps which can be seen in Fig. 5.4. There are 45 pad rows, radially located between the inner and outer radii, in each sector. Each sector is divided in inner (13 pad rows) and outer (32 pad rows) subsectors. The outer subsectors have continuous pad coverage to optimize the dE/dx measurements. The inner subsectors are in the region of highest track density and are optimized for good two-hit resolution, using smaller pads. Figure 5.5 shows the distribution of pads in one sector of the TPC.

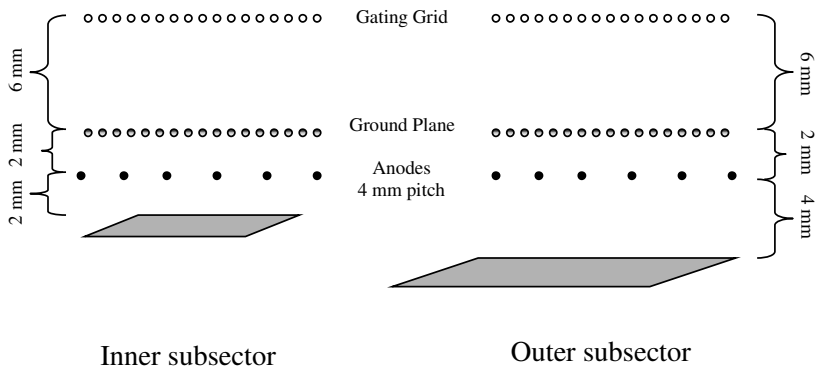

Figure 5.6: TPC gating grid and readout chamber.

The readout chamber is separated from the drift region by the gating grid. The gating grid is a plane of wires that electronically separates the amplification region from the drift region. It is usually closed to prevent ions created in the amplification region from getting back into the drift region. When an event is to be recorded, the gating grid wires are set to voltages that allow electrons to pass through.

The readout chamber consists on two wire planes: a ground plane and anode wires, located above the pad plane as shown in Fig. 5.6. The ground plane shields the TPC drift region from the strong fields around the anode wires. As electrons drift pass the gating grid and the ground plane, they accelerate towards the anode wires where they initiate an avalanche, leaving a cloud of positively charged ions remaining around the wires. The pads image

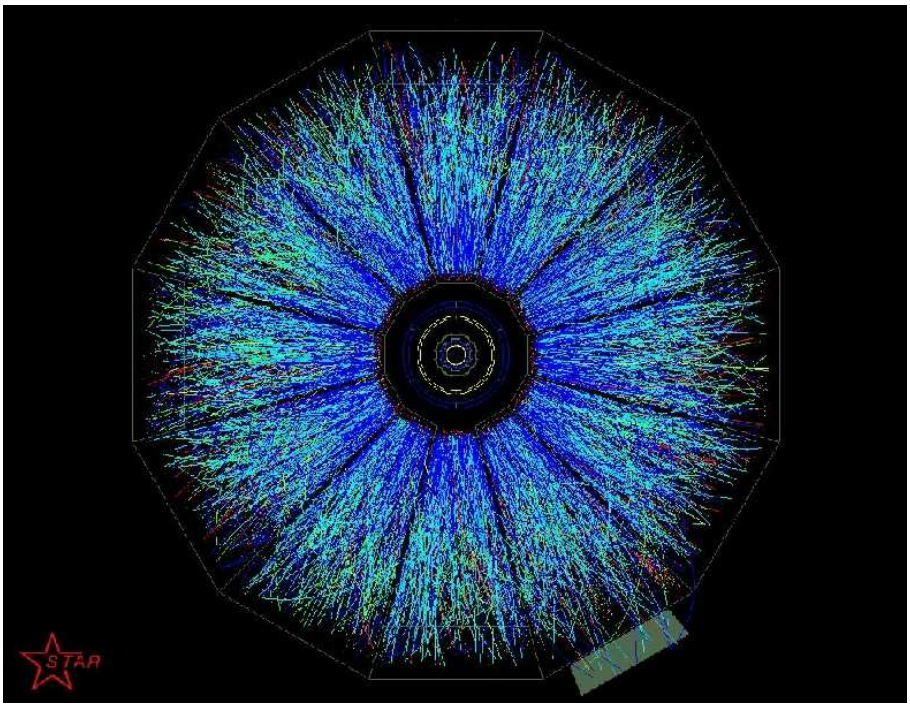

Figure 5.7: View of an event from the end of the TPC as displayed by the level 3 trigger.

this charge that goes to the electronics. The size and shape of the ion cloud depends on the number of primary ions, drift distance and diffusion, and gas gain.

5.2.2 The trigger system

The STAR trigger system is based on the input from fast detectors to control the event selection for the much slower tracker detectors [94]. It is divided into different layers with level 0 being the fastest while level 1 and 2 are slower but apply more restrictive constraints on the event selection. STAR

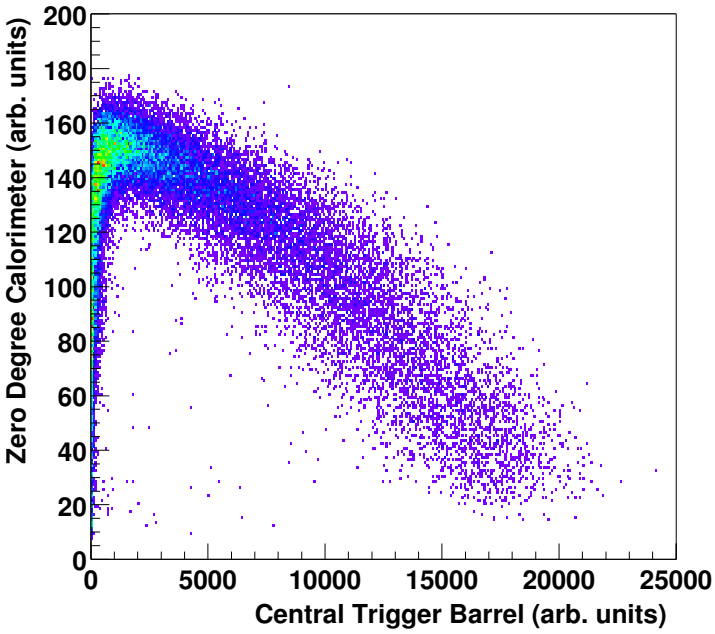

Figure 5.8: Summed pulse heights from the ZDCs vs the ones from the CTB for events with primary collision vertex successfully reconstructed from tracks in the TPC.

has a third level trigger that performs complete online reconstruction of the events [95]. An online display of the level 3 trigger provides views of the events as the one shown in Fig. 5.7, from the end of the TPC.

The fast detectors that provide input to the trigger system are the CTB at $|\eta| < 1$ and the ZDCs in the forward direction at $\theta < 2$ mrad. The CTB surrounds the outer cylinder of the TPC and triggers on the flux of charged particles in the midrapidity region. It consists of 240 scintillator slats arranged in 4 cylindrical bands each covering 1/2 unit of pseudorapidity. The

ZDCs are used to measure the energy of neutral particles remaining in the forward direction since spectators neutrons diverge by less than 1 mrad from the beam. Each ZDC consists of three modules and each module consists on a series of tungsten plates alternating with layers of wavelength shift fibers that route Cherenkov light to a photo multiplier tube.

Figure 5.8 shows the summed ZDC pulse height and that of the CTB for events with primary vertex successfully reconstructed from tracks in the TPC. In collisions at small impact parameters (central collisions), small ZDC values and large multiplicity in the CTB are measured. As the impact parameter increases, the multiplicity measured by the CTB decreases while the energy measured by the ZDC increases. For very large impact parameter (most peripheral collisions), the multiplicity in the CTB is small and the energy in the ZDCs is also small as the neutral spectator fragments are bound to the charged ones and thus deflected by the beam magnets.

In the analysis presented here events from two different trigger settings were used. Hadronic minimum bias, that requires a coincidence of signals above threshold in both ZDCs, and hadronic central, that also requires high CTB signal.

5.3 Hits, tracks and event reconstruction

The reconstruction of the tracks of primary particles passing through the TPC in a given event is as follows. First the ionization clusters in the TPC are separately found in the x and y coordinates. These are determined by the

charge measured on adjacent pads in a single pad row. Assuming that the signal distribution on the pads is a Gaussian

$$x = \frac{\sigma^2}{2\omega} \ln\left(\frac{h_3}{h_1}\right), \tag{5.1}$$

where h_1, h_2, and h_3 are the amplitudes on 3 adjacent pads with pad h_2 centered at y = 0, ω is the pad width and

$$\sigma^2 = \frac{\omega^2}{\ln(h_1 h_2 h_3)}. \tag{5.2}$$

Once the pad location of the clusters is known, a pass is made to find single tracks, *i.e.* that left by a single charged particle as it crossed the pad row, and multiple hits in a cluster. Deconvolution of close hits is very important for two-track resolution and dE/dx measurements. The found hits are then transformed into TPC space points, where the z coordinate is determined by measuring the time of arrival of the electrons in "time buckets" and weighting the average by the amount of charge collected in each bucket. These space points also contain information on the energy deposited by the track.

The track reconstruction algorithm starts by finding a 3-point seed in the outer pad rows of the TPC where the hit density is smaller. This seed is then extrapolated inwards to the next pad rows. A hit in a pad row is added to the track segment if it lies inside a search radius around the track projection to that pad row. Once all the tracks are formed, a Kalman procedure is used to fit the track. The Kalman fit includes Coulomb scattering and energy loss in the traversed material. The Kalman fit is run twice, once outwards and another time inwards, and during this process the outlier hits are removed in

order to improve track momentum resolution. A further pass is done to join track segments that were split during the track finding process. These reconstructed tracks are called *global tracks*. The particle charge is determined by correlating the curvature direction of the track and the magnetic field.

The primary vertex position is calculated from the maximum of the distribution of the position of closest approach of every reconstructed global track to the beam line. After the primary vertex is determined, another fit to the tracks with a distance of closest approach to the primary vertex of less than 3 cm is performed, but in this case the primary vertex in included as a point of the track. If the fit is successful, the track parameters are updated and the track is classified as a *primary track*. The analysis presented in this thesis uses those primary tracks.

CHAPTER 6

ANALYSIS

In this chapter a detail description of the analysis is given and several experimental issues with high importance to HBT like Coulomb interaction or momentum resolution are discussed.

6.1 Event selection and centrality binning

For this analysis, we selected events with a collision vertex position within $\pm$25 cm measured from the center of the TPC in order to keep the same acceptance with the rapidity selection applied. This event *selection* was applied to all data discussed here.

The centrality of the collision was characterized according to the measured multiplicity of charged hadrons at midrapidity as shown in Fig. 6.1. For the analysis presented here we binned our data in six centrality bins corresponding to 0-5%, 5-10%, 10-20%, 20-30%, 30-50% and 50-80% of the total hadronic cross section. A hadronic-central triggered data set of 1 million events was used only for the first bin, the other five bins are from a minimum-bias triggered data set of 1.7 million events.

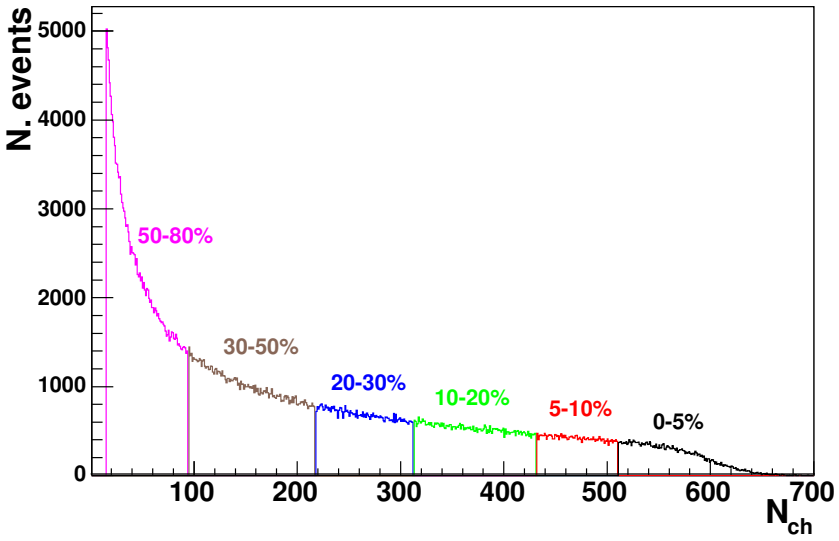

Figure 6.1: Multiplicity distribution.

It was mentioned in Chapter 4 that the denominator of the correlation function, $B(\vec{q},\vec{k})$ in Eq. (4.39), is formed by mixing particles in separate events, so that each particle in one event is mixed with all the particles in a collection of events which in our case consists of 20 events, which is a number large enough to avoid the introduction of any bias in our correlation function. Mixed pairs are formed only with particles with "similar" events in order to avoid any signal in our correlation function that could be produced by mixing events with different characteristics. In our analysis, similar events have primary vertex position within 5 cm and multiplicities within 5 to 30% of the total cross section.

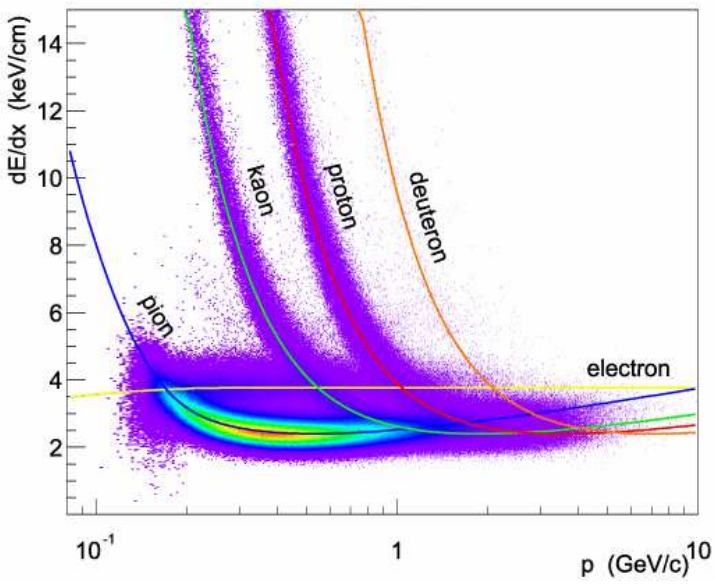

Figure 6.2: dE/dx vs. momentum.

6.2 Particle selection

We selected tracks in the rapidity region $|y| < 0.5$. Particle identification was done by correlating the specific ionization of the particles in the gas of TPC with their measured momentum. The energy lost by a particle as it travels through a given gas depends on the velocity at which it travels and it is described by the Bethe-Bloch formula [96]

$$-\frac{dE}{dx} = \kappa z^2 \frac{Z}{A\beta^2}[\frac{1}{2}\ln\frac{2m_e c^2\gamma^2\beta^2}{I^2}E_{kin} - \beta^2 - \frac{\delta}{2}].$$

For a given momentum, each particle mass will have a different velocity and a different dE/dx as it traverses the gas of the TPC, as seen in Fig. 6.2.

For this analysis, pions were selected by requiring the deviation of the specific ionization to be within 2 standard deviations (experimentally determined as a function of the particle momentum and event multiplicity) of the Bethe-Bloch value for pions. To help remove kaons that could satisfy this condition, particles were also required to be farther than 2 standard deviations of the expected value for kaons. There is a small contamination of electrons in our pion sample, specially in the low momentum region ($p < 400$ MeV/c). The effect of this contamination will be discussed later in this chapter.

To reduce contributions from non-primary pions, we applied a DCA (distance of closest approach of the extrapolated track to the primary vertex) cut of 3 cm to each track.

In the STAR HBT analysis at $\sqrt{s_{NN}} = 130$ GeV [80], as well as in previous experiments [97, 98, 99, 100, 101], tracks were divided in different bins according with their transverse momentum, p_T, and only particles within a given bin were used to form correlation functions. In the analysis presented here, no specific p_T cut was applied to *single* tracks; however, due to limitations in the identification of pions due to the mixing of the dE/dx bands at high momentum (Fig. 6.2), and to the momentum pair cut described in next section, only tracks with $p < 1.2$ GeV/c are included in the correlation functions.

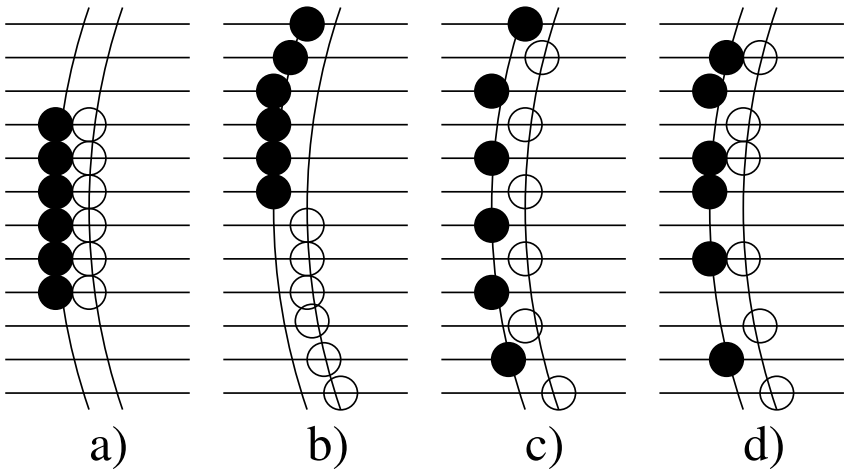

Figure 6.3: Distribution of same number of hits in two tracks for four possible cases. Closed circles are hits assigned to one track, open circles are assigned to the other. a) SL = -0.5 (clearly two tracks) b) SL = 1 (possible split track) c) SL = 1 (possible split track) d) SL = 0.08 (likely two tracks)

6.3 Pair cuts

In this section we describe two cuts that are intended to remove the effects of two track reconstruction defects that have high impact on HBT: split tracks (one single particle reconstructed as two tracks) and merged tracks (two particles with similar momenta reconstructed as one track).

6.3.1 Track splitting

Track splitting causes an enhancement of pairs at low relative momentum q. This false enhancement is created by single particles reconstructed as two tracks with similar momenta. In order to remove these split tracks we compared the location of the hits for each track in the pair along the pad-rows

in the TPC and assigned a quantity to each pair, called *Splitting Level* (SL), calculated as follows:

$$\mathrm{SL} \equiv \frac{\sum_i S_i}{\mathrm{Nhits}_1 + \mathrm{Nhits}_2} \quad \text{where} \quad \mathrm{S}_i = \tag{6.1}$$
$$\begin{cases} +1 & \text{one track leaves a hit on pad-row} \\ -1 & \text{both tracks leave a hit on pad-row} \\ 0 & \text{neither track leaves a hit on pad-row}, \end{cases}$$

where i is the pad-row number, and Nhits_1 and Nhits_2 are the total number of hits associated to each track in the pair. If only one track has a hit in a given pad-row +1 is added to this running quantity, if both tracks have a hit in the same pad-row, a sign of separate tracks, -1 is added to this quantity; after the sum is done, it is divided by the sum of hits in both tracks, this normalizes SL to a value between -0.5 (both tracks have hits in exactly same pad-rows) and 1.0 (tracks do not have any hit in same pad-row). Figure 6.3 shows four different cases for the same number of total hits; in case a) two different tracks with SL = -0.5, in b) and c) two different cases of possible split tracks with SL = 1, and in d) two different tracks with SL = 0.08.

The enhancement of pairs at low relative momentum caused by split tracks can be seen in Fig. 6.4 where the distribution of "real" pairs (pairs of tracks from same event) vs. relative invariant momentum (q_{inv}) and SL is shown. This enhancement is not seen for "mixed" pairs (pairs of tracks from different events) in Fig. 6.5.

To remove these split tracks, we required every pair to have SL smaller than a certain value. This value was determined from the 1-dimensional correlation functions for different values of SL; some of them are shown in Fig.

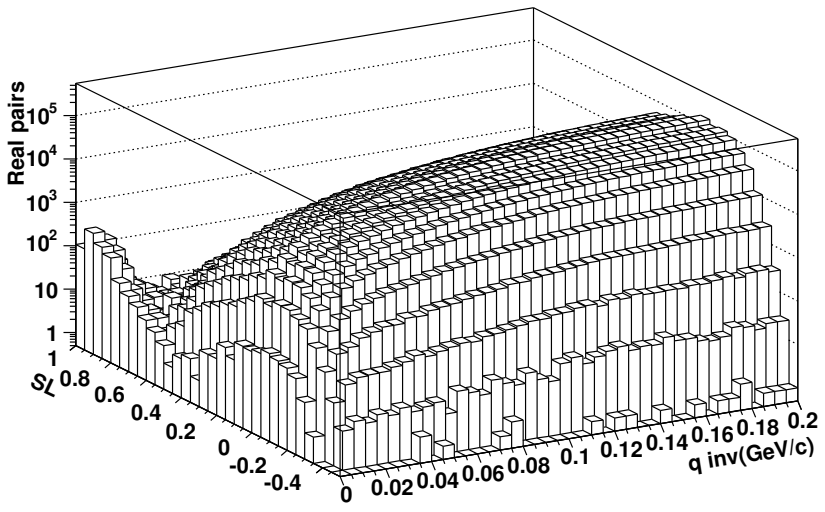

Figure 6.4: Distribution of pairs of tracks from the same event vs. relative momentum q_{inv} and splitting level (SL).

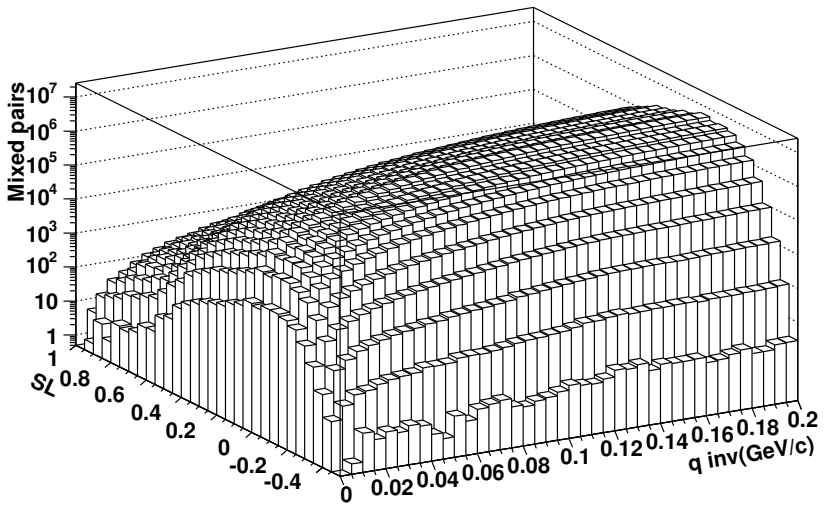

Figure 6.5: Distribution of pairs of tracks from different events vs. relative momentum q_{inv} and splitting level (SL).

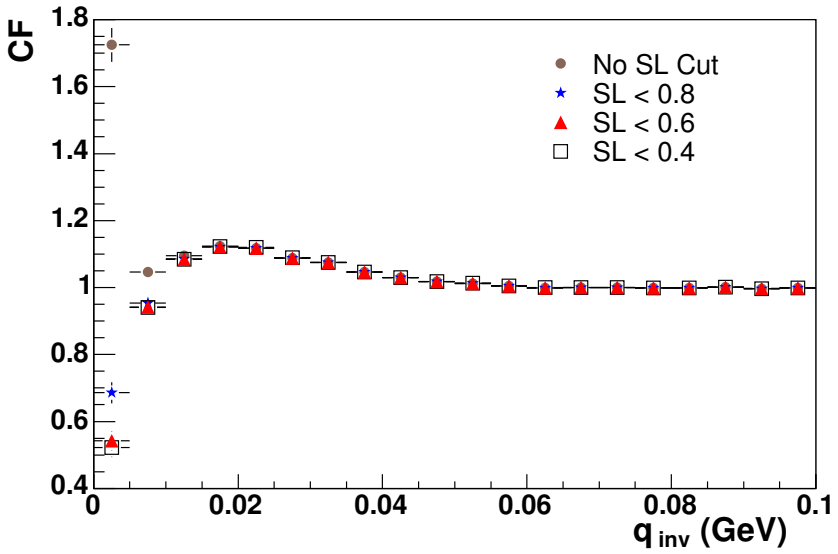

Figure 6.6: 1D correlation function for different values of SL (anti-splitting cut). The cut applied in this analysis is SL < 0.6.

6.6. We observe that when making this cut more restrictive (reducing the maximum allowed value for SL) the enhancement is reduced until we reach SL = 0.6 when the correlation function becomes stable and does not change for lower values of SL. Therefore, all the pairs entering the correlation functions were required to have SL < 0.6; cutting at this value is also supported by simulation studies. While the SL cut eliminates all the false "real" pairs produced by track splitting, it also removes some pairs which happen to satisfy the cut but do not originate from a single particle. Therefore we apply the SL cut to both, "real" and "mixed" pairs.

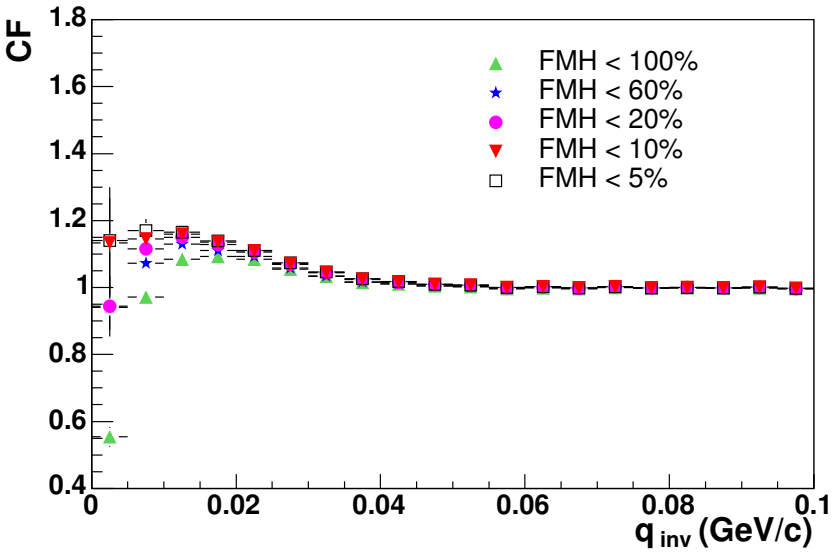

Figure 6.7: 1D correlation function for different values of the maximum fraction of merged hits allowed. Cut applied in the analysis is fraction of merged hits (FMH) $< 10\%$.

6.3.2 Track merging

Once we have removed split tracks, we can study the effects of two particles reconstructed as one track. Merged tracks cause a reduction of pairs at low relative momentum since the particles that have higher probability of being merged are those with similar momenta. To eliminate the effect of track merging, we required that all pairs entering numerator and denominator of the correlation function had a fraction of merged hits no larger than 10%. Two hits are considered merged if the probability of separating them is less than 99% according to the two-track resolution in the TPC. By applying this cut to "real" and "mixed" pairs, we introduce in the denominator the effect that merged tracks have in the numerator: a reduction of low q pairs. However, we may also remove "real" pairs that satisfy the cut, this would reduce the HBT fit parameters, and needs to be taken into account as will be described later in this chapter.

To determine the maximum fraction of merged hits allowed we proceed as we did for the anti-splitting cut. Figure 6.7 shows the 1-dimensional correlation functions for different values of the maximum fraction of merged hits allowed. By requiring the fraction of merged hits to be less than 10% for every pair entering the correlation function, the effect of merged tracks in the correlation function was almost completely removed.

6.3.3 k_T cut

As already mentioned, no p_T cut was applied to *single* tracks, however, in addition to the two cuts already described, *pairs* were required to have an average transverse momentum (k_T) between 150 and 600 MeV/c and they were divided in 4 k_T bins (150-250, 250-350, 350-450 and 450-600 MeV/c). No difference was observed between the extracted HBT parameters when applying equivalent p_T or k_T cuts, however statistics improves when using the latter one, as two pions from different p_T bins will be used in a k_T-cut analysis, but not in a p_T-cut one.

6.4 Coulomb interaction and fitting procedures

As discussed in Chapter 4, Eq. (4.34) applies only if the sole cause of correlation is quantum statistics. In our case, significant Coulomb effects must also be accounted for (strong interactions are negligible here [57]). This Coulomb interaction, repulsive for like-sign particles, causes a reduction on the number of real pairs at low q reducing the correlation function.

Three different procedures can be applied in order to take this interaction into account. The first procedure, that was used in the STAR HBT analysis at $\sqrt{\mathrm{S_{NN}}}$ = 130 GeV [80], as well as by previous experiments [97, 98, 99, 100, 101], consists on fitting the correlation function to:

$$C(q_o, q_s, q_l) = \frac{A(\vec{q})}{B(\vec{q})} = K_{\mathrm{coul}}(q_{\mathrm{inv}}) \times (1 + \lambda e^{-q_o^2 R_o^2 - q_s^2 R_s^2 - q_l^2 R_l^2}), \tag{6.2}$$

normalized to unity at large $\vec{q}$, where $K_{\text{coul}}(q_{\text{inv}})$ is the squared Coulomb wavefunction integrated over the whole source (as described in 4.2.1), which in our case is a spherical Gaussian source of 5 fm radius. Traditionally, equation (6.2) has been expressed as:

$$C'(q_o, q_s, q_l) = \frac{A(\vec{q})}{B(\vec{q})K_{\text{coul}}(q_{\text{inv}})} = 1 + \lambda e^{-q_o^2 R_o^2 - q_s^2 R_s^2 - q_l^2 R_l^2}, \tag{6.3}$$

and this new correlation function was called the *Coulomb corrected correlation function* since we introduce in the denominator a Coulomb factor with what we try to compensate the Coulomb interaction that is present in the numerator. We call this the *standard* procedure. However, this procedure overcorrects the correlation function since it assumes that all pairs in the background are primary pairs and need to be corrected, including those that are not formed by primary pions.

In the second procedure, inspired by the previous one and implemented before by the E802 Collaboration [102], the Coulomb term is diluted according to the fraction of pairs that Coulomb interact:

$$K'_{\text{coul}}(q_{\text{inv}}) = 1 + f(K_{\text{coul}}(q_{\text{inv}}) - 1), \tag{6.4}$$

where f has a value between 0 (no Coulomb weighting) and 1 (*standard* weight). The correlation function, normalized to unity at large $\vec{q}$, in this procedure is fitted to:

$$C(q_o, q_s, q_l) = \frac{A(\vec{q})}{B(\vec{q})} = K'_{\text{coul}}(q_{\text{inv}}) \times (1 + \lambda e^{-q_o^2 R_o^2 - q_s^2 R_s^2 - q_l^2 R_l^2}).$$

We call this the *dilution* procedure. Assuming that λ is approximately the fraction of primary pions, we compare the *standard* procedure to the *dilution*

one with $f = \lambda$ in the latter one. This increases R_o by 10-15% and has a very small effect in R_s and R_l as seen in Fig. 6.8, circles; λ decreases by 10-15%.

Finally, in this analysis, we have implemented a new procedure, first suggested by Bowler [60] and Sinyukov [103], and recently advocated by the CERES collaboration [104], in which only pairs with Bose-Einstein interaction are considered to Coulomb interact. The correlation function in this procedure is fitted to:

$$C(q_o, q_s, q_l) = \frac{A(\vec{q})}{B(\vec{q})} = (1 - \lambda) + \lambda K_{\text{coul}}(q_{\text{inv}})(1 + e^{-q_o^2 R_o^2 - q_s^2 R_s^2 - q_l^2 R_l^2}), \qquad (6.5)$$

normalized to unity at large $\vec{q}$, where $K_{\text{coul}}(q_{\text{inv}})$ is the same as in the *standard* procedure. The first term on the right-hand side of equation (6.5) accounts for the pairs that do not interact and the second term for the ones that (Coulomb and Bose-Einstein) interact. We call this *Bowler-Sinyukov* procedure. It has a similar effect on the HBT parameters as the *dilution* one as seen in Fig. 6.8.

It is worth mentioning that the fact that the parameters λ and R_o, and consequently the ratio R_o/R_s, extracted using the *standard* procedure are smaller than the ones obtained in the STAR HBT analysis at $\sqrt{s_{NN}} = 130$ GeV [80], is explained by a different particle selection used for each analysis. In the analysis presented here, the contribution from non-primary pions is larger than in the previous one leading to smaller λ and R_o when using that procedure. However, the parameters obtained when using the *Bowler-Sinyukov* procedure are almost not affected by this contribution from non-primary pions.

Figure 6.9 shows the projections of the 3-dimensional correlation function according to the Bertsch-Pratt parametrization described in section 4.4 for

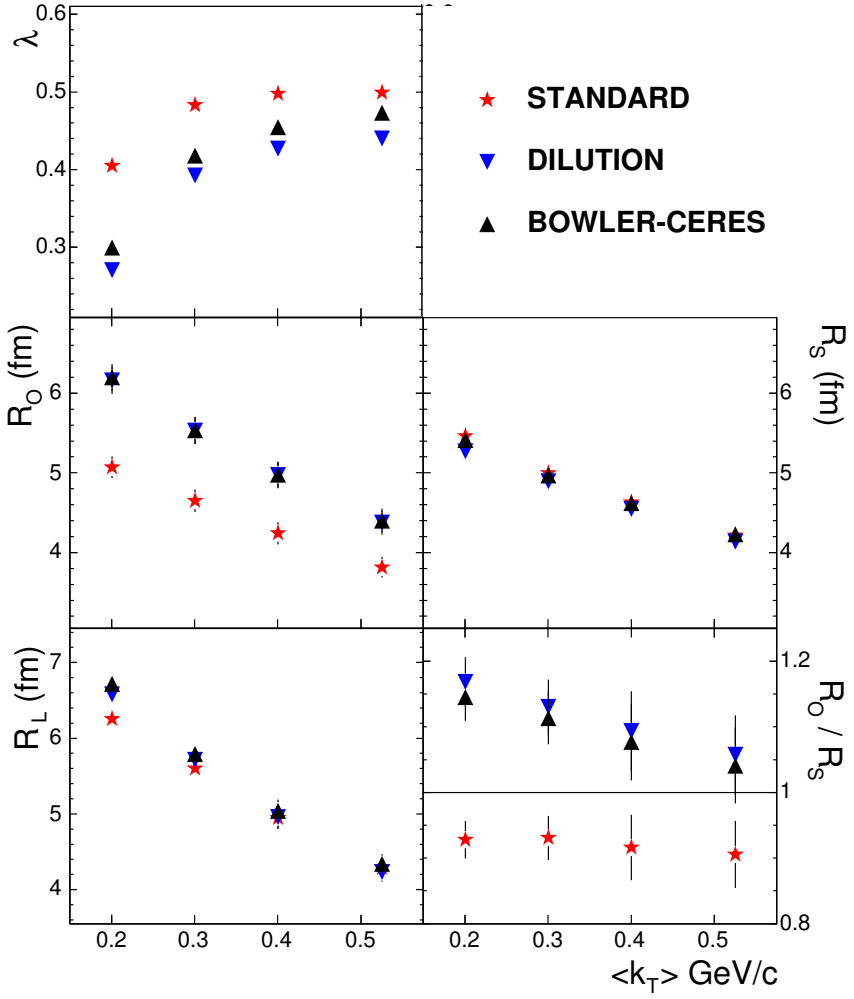

Figure 6.8: HBT parameters for the three possible fitting procedures to the correlation functions from the 0-5% most central events.

an azimuthally integrated analysis. The closed symbols represent the uncorrected correlation function and the open ones the *Coulomb corrected correlation function* according to the *standard* procedure. The lines are fits to the data, the dashed line is the *standard* fit to the *Coulomb corrected correlation function*, and the solid line the *Bowler-Sinyukov* fit to the uncorrected one.

As a consistency check for the *Bowler-Sinyukov* procedure, we calculated the $\pi^+\pi^-$ correlation function, which is dominated by Coulomb interaction, and compare to different calculations. In Fig. 6.10, lines indicate the *standard* (dashed) ($K_{\rm coul}(q_{\rm inv})$) and *Bowler-Sinyukov* (solid) ($(1-\lambda)+\lambda K_{\rm coul}(q_{\rm inv})$) Coulomb functions; in the latter, λ was extracted from the fit to the 3D like-sign correlation function. Clearly, the *Bowler-Sinyukov* function (solid line) better reproduces the data (triangles) than the *standard* function (dashed line). The small discrepancy between the *Bowler-Sinyukov* function and the data disappears when strong interaction (negligible for like sign pairs) is added to the *Bowler-Sinyukov* function as shown by the theoretical calculation [105] (stars).

The Coulomb interaction between the outgoing charged pions and the residual positive charged source is negligible. This is confirmed by the good agreement observed between the parameters extracted from $\pi^+\pi^+$ and $\pi^-\pi^-$ correlation functions as will be shown later in this thesis, Fig. 7.1.

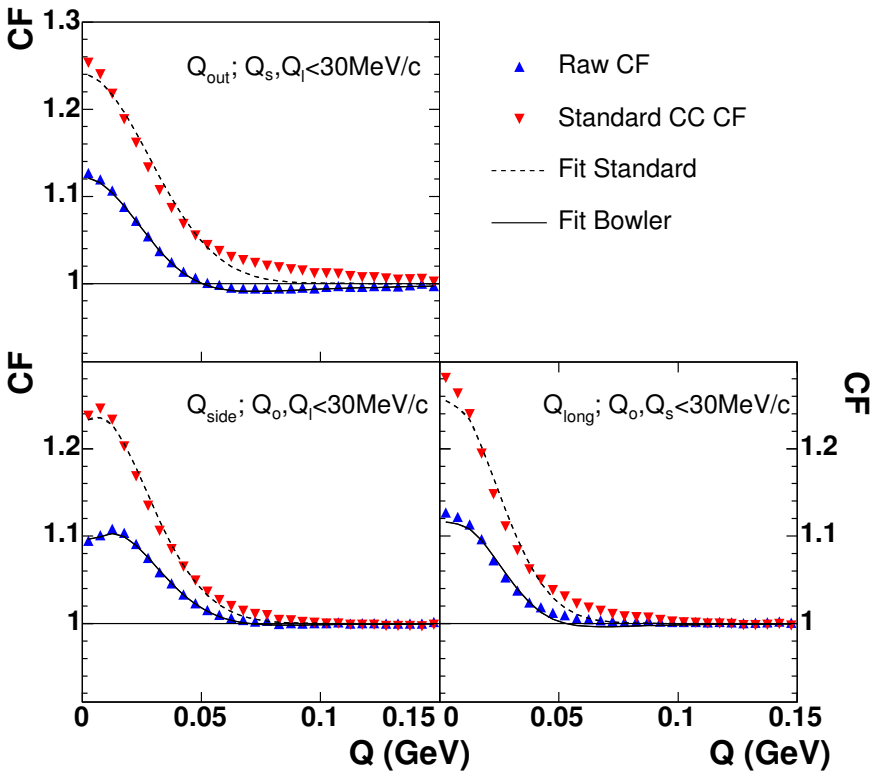

Figure 6.9: Projections of the 3 dimensional correlation function and corresponding fits for negative pions from the 0-5% most central events and $150 < k_T < 250$ MeV/c) according to the *standard* (dashed line) and *Bowler-Sinyukov* (solid line) procedures.

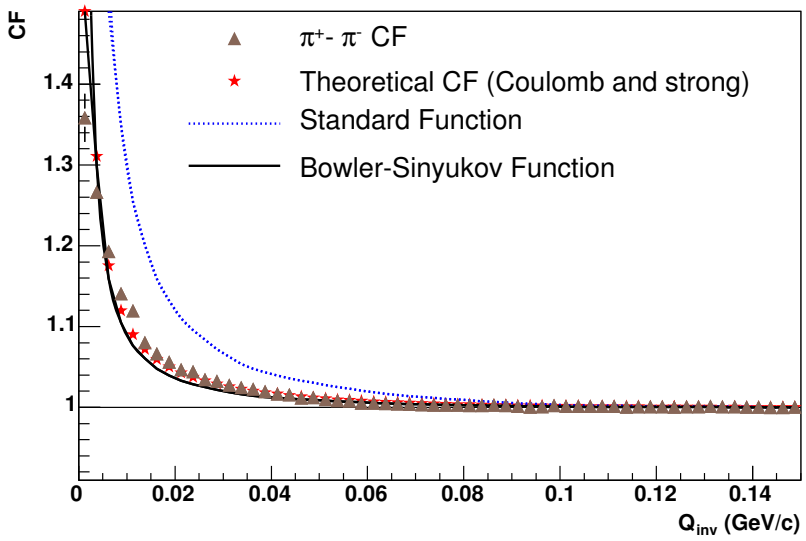

Figure 6.10: 1D correlation function for $\pi^+\pi^-$ compared to Standard, Bowler-Sinyukov functions and a theoretical calculation that includes Coulomb and strong interactions.

6.5 Momentum resolution correction

The limited single-particle momentum resolution induces systematic underestimation of the HBT parameters. To determine the magnitude of this effect we need to know the momentum resolution for the particles under consideration. The components of $\vec{p}$ expressed as a function of the measured quantities p_T, the azimuthal angle, φ, and the polar angle, θ, are

$$\begin{aligned} p_x &= p_T \cos(\varphi) \\ p_y &= p_T \sin(\varphi) \\ p_z &= \frac{p_T}{\tan(\theta)}. \end{aligned} \tag{6.6}$$

The deviation of these components from the *real* components is the momentum resolution and can be expressed as

$$\begin{aligned} \delta p_x &= p_x \frac{\delta p_T}{p_T} - p_y \delta\varphi \\ \delta p_y &= p_y \frac{\delta p_T}{p_T} + p_x \delta\varphi \\ \delta p_z &= p_z \frac{\delta p_T}{p_T} + p_T \frac{\delta\theta}{\sin^2(\theta)}. \end{aligned} \tag{6.7}$$

We extract the widths δp_T, $\delta\varphi$ and $\delta\theta$ as a function of p for midrapidity pions from Monte-Carlo tracks embedded into real events. Figure 6.11 shows these widths as a function of p_T. We see that the resolution on p_T, given by $\delta p_T / p_T$, has a width of about 1% for the p range under consideration.

To account for this limited momentum resolution, a correction, K_{momentum}, is applied to each measured correlation function:

$$C(\vec{q}_{\text{meas}}) = \frac{A(\vec{p}_{1,\text{meas}}, \vec{p}_{2,\text{meas}})}{B(\vec{p}_{1,\text{meas}}, \vec{p}_{2,\text{meas}})} K_{\text{momentum}}. \tag{6.8}$$

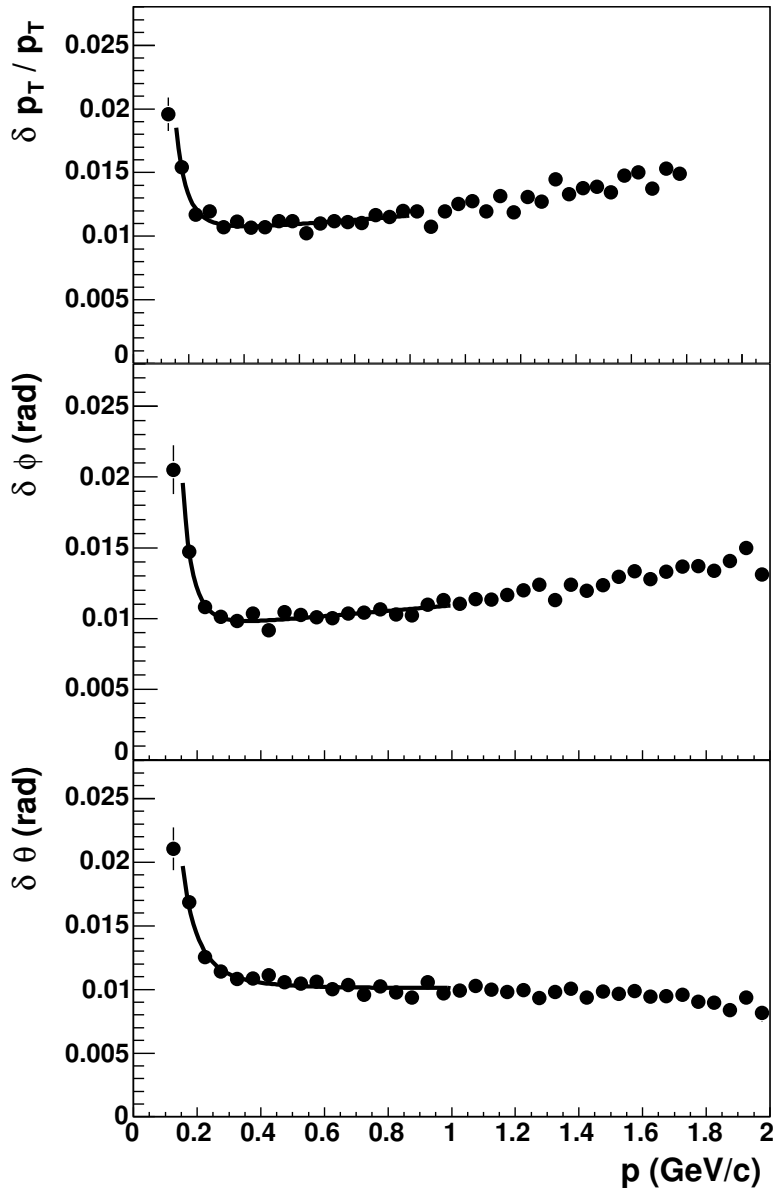

Figure 6.11: Momentum resolution for pions at midrapidity expressed by the widths $\delta p_T/p_T$, $\delta\varphi$ and $\delta\theta$ as a function of p.

The correction factor is calculated from the single-particle momentum resolution as follows:

$$K_{\text{mometum}}(\vec{q}) = \frac{C_2(\vec{q}_{\text{ideal}})}{C_2(\vec{q}_{\text{smear}})} = \frac{\frac{A(\vec{p}_{1,\text{ideal}},\vec{p}_{2,\text{ideal}})}{B(\vec{p}_{1,\text{ideal}},\vec{p}_{2,\text{ideal}})}}{\frac{A(\vec{p}_{1,\text{smear}},\vec{p}_{2,\text{smear}})}{B(\vec{p}_{1,\text{smear}},\vec{p}_{2,\text{smear}})}}, \tag{6.9}$$

where the *ideal* and *smear* correlation function are formed as follows.

Numerator and denominator of the *ideal* correlation function are formed by pairs of pions from different events. Each pair in the numerator is weighted, accordingly with the *Bowler-Sinyukov* function, by:

$$weight = (1-\lambda) + \lambda K_{\text{coul}}(q_{\text{inv}}) \times (1 + e^{-q_o^2 R_o^2 - q_s^2 R_s^2 - q_l^2 R_l^2}), \tag{6.10}$$

where $K_{coul}(q_{inv})$ is the same one as described in section 6.4. If the measured momentum were the "real" momentum, this *ideal* correlation function would be the "real" correlation function, however this is not the case, so we calculate a *smeared* correlation function for which numerator and denominator are also formed by pairs of pions from different events but their momenta have been smeared according to the extracted momentum resolution. Pairs in numerator are also weighted by the $weight$ given by Eq. (6.10). This *smeared* correlation function is to the *ideal* one, as our "measured" correlation function is to the "real" one, which allows us to calculate the correction factor.

For the $weight$, certain values for the HBT parameters (λ, R_o, R_s, and R_l) need to be assumed. Therefore, this procedure is iterative with the following steps:

1. Fit the correlation function without momentum resolution correction and use the extracted HBT parameters for the first $weight$

2. Construct the momentum resolution corrected correlation function

3. Fit it according to (6.5)

4. If the extracted parameters agree with the ones used to calculate the $weight$, those are the final parameters. If they differ from the ones used, then use this latter extracted parameters for the new $weight$ and go back to step 2.

Also, to be fully consistent, the Coulomb factor $K_{\text{coul}}(q_{\text{inv}})$ used in the fit to extract the HBT parameters must be modified to account for momentum resolution as follows:

$$K_{\text{coul}}(q_{\text{inv}}) = K_{\text{coul}}(q_{\text{inv,meas}})\frac{K_{\text{coul}}(q_{\text{inv,ideal}})}{K_{\text{coul}}(q_{\text{inv,smear}})} = \frac{K^2_{\text{coul}}(q_{\text{inv,meas}})}{K_{\text{coul}}(q_{\text{inv,smear}})}. \tag{6.11}$$

For this analysis, after two iterations the extracted parameters were consistent with the input ones. We also checked that when convergence is reached, the "uncorrected" results matched the *smeared* ones. The effect of this correction is an increase on the HBT radius parameters between 1.0% for the lowest k_T bin (150, 250) MeV/c and 2.5% for the highest one (450, 600) MeV/c.

6.6 Systematic associated with pair cuts

The maximum fraction of merged hits cut used to remove the effects produced by track merging, as described in section 6.3, introduces a systematic reduction on the HBT fit parameters λ, R_o^2, R_s^2, and R_l^2, since it discriminates against low-q pairs which carry the correlation signal.

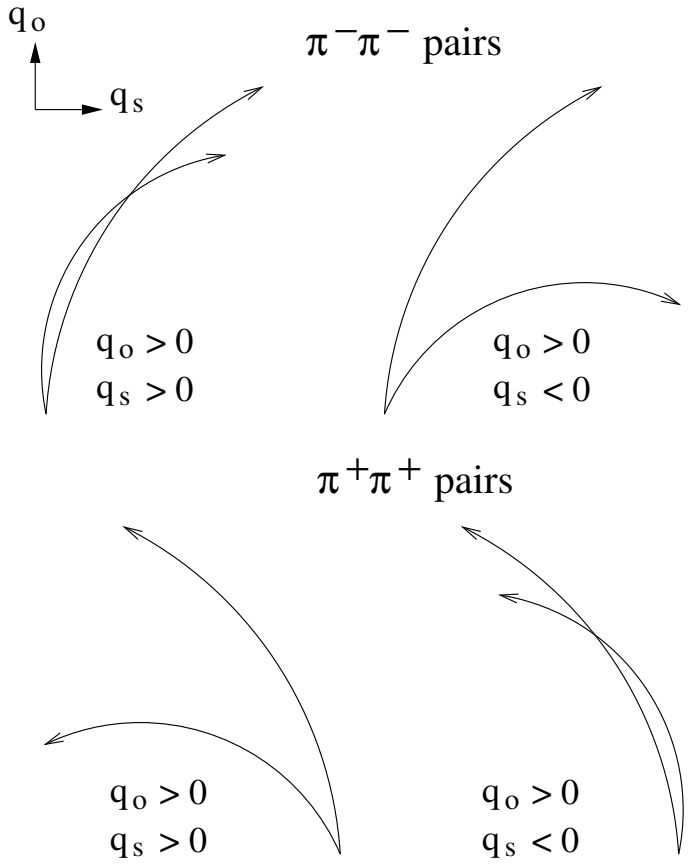

Figure 6.12: For $\pi^-\pi^-$ pairs (top), merging occurs more often between tracks with $|q_o q_s| = q_o q_s$ than with $|q_o q_s| \neq q_o q_s$. For $\pi^+\pi^+$ pairs (bottom) opposite conditions are satisfied.

In order to estimate this reduction we define a validity range for the cut in the number of merged hits in which the lower limit is 0 (*i.e.* no merging) and the upper limit is defined by the value for which we consider there is already *too much* merging. This value is determined from the 0^{th} order Fourier coefficients, $R^2_{os,0}$ which is expected to be 0 (see equation 4.38). However, track merging introduces a deviation caused by the preferential merging of track pairs with correlated transverse momenta, q_o and q_s as shown in Fig. 6.12. In the case of $\pi^-\pi^-$ pairs, there is a higher degree of track merging when $|q_o q_s|$ = $q_o q_s$ than when $|q_o q_s| \neq q_o q_s$ (top pairs). For $\pi^+\pi^+$ pairs the conditions are opposite (bottom pairs).

When R^2_{os} for $\pi^+\pi^+$ or $\pi^-\pi^-$ analysis clearly deviates from 0, we considered that there is already *too much* merging and use that value of the maximum fraction of merged hits as the upper limit of the validity range. We calculate the change on each HBT radius in this range and consider it to be the artificial reduction due to the cut for that specific parameter. This reduction is included as a systematic error in the final error. This is done for each centrality and each k_T bin.

As an example, Fig. 6.13 shows the 0^{th} order (left) and 2^{nd} divided by 0^{th} order (right) Fourier coefficient as a function of the maximum fraction of merged hits allowed for the 5% most central events and k_T between 150 and 250 MeV. From $R^2_{os,0}$, located in the bottom left panel, we determined the upper limit of our range to be 0.2 and the corresponding variations in the HBT radii to be 0.7% for R_o, 0.5% for R_s and 1.1% for R_l.

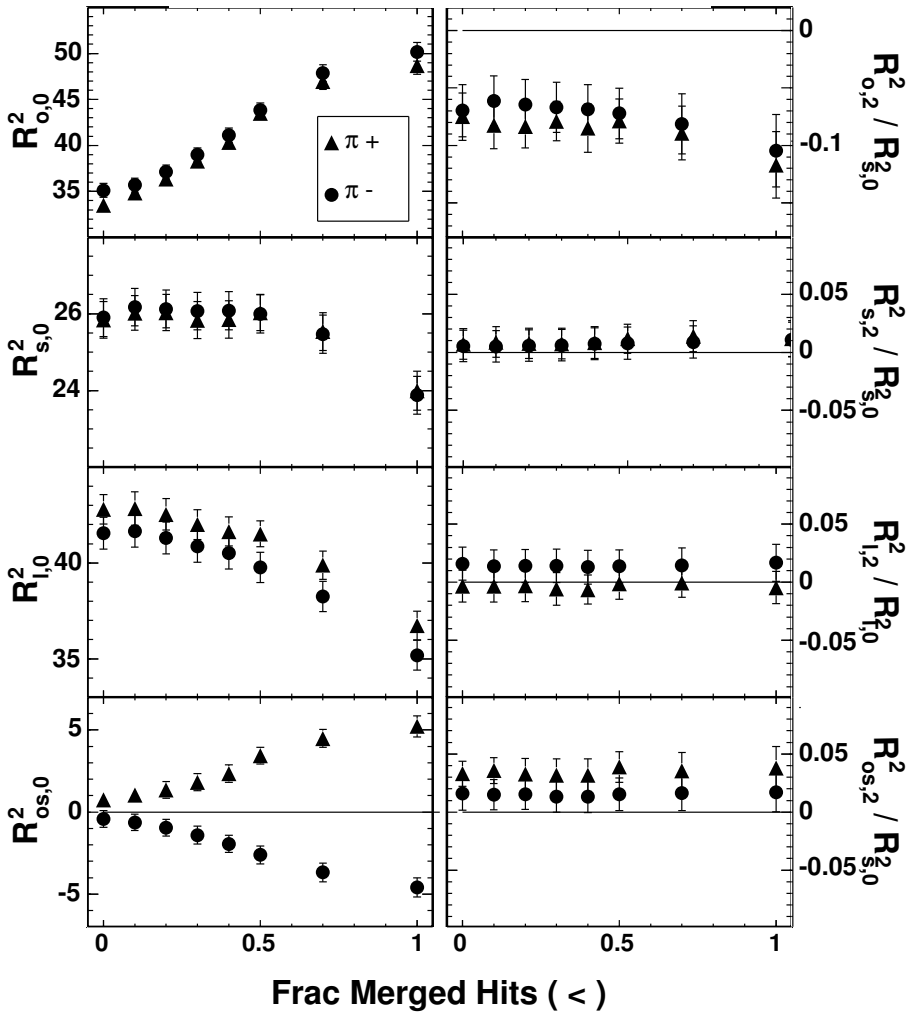

Figure 6.13: Fourier coefficients as a function of the maximum fraction of merged hits for the 5% most central events and k_T between 150 and 250 MeV/c.

6.7 How Gaussian is the source?

As already discussed, the shape of the correlation function is usually described by a Gaussian. Before showing the results from our analysis it is important to study the possible deviations of our correlation functions from a Gaussian shape. To do so, we followed the method suggested in [106], in which the *Edgeworth expansion*, an expansion based on a complete orthonormal set of functions around a Gaussian, is expected to give a better description of the data. The expansion around the 3-dimensional Gaussian in the *Bowler-Sinyukov* procedure for an azimuthally integrated analysis is

$$\begin{aligned} C(q_o, q_s, q_l) &= (1-\lambda) + \lambda K_{\text{coul}}(q_{\text{inv}}) \\ &+\lambda K_{\text{coul}}(q_{\text{inv}}) \cdot e^{-q_o^2 R_o^2 - q_s^2 R_s^2 - q_l^2 R_l^2} \times \\ &\Big[1 + \sum_{n=4,n\ even}^{\infty} \frac{\kappa_{o,n}}{n!(\sqrt{2})^n} H_n(q_o R_o)\Big] \times \\ &\Big[1 + \sum_{n=4,n\ even}^{\infty} \frac{\kappa_{s,n}}{n!(\sqrt{2})^n} H_n(q_s R_s)\Big] \times \\ &\Big[1 + \sum_{n=4,n\ even}^{\infty} \frac{\kappa_{l,n}}{n!(\sqrt{2})^n} H_n(q_l R_l)\Big], \end{aligned} \tag{6.12}$$

where $\kappa_{i,n}$ ($i = o, s, l$) are fit parameters and $H_n(q_i R_i)$ are the Hermite polynomials of order n:

$$H_n(x) = (-1)^n e^{x^2} \frac{d^n}{dx^n}\, e^{-x^n}. \tag{6.13}$$

Only Hermite polynomials of even order are included in the expansion because the correlation function for identical particles must be invariant under $(q_o, q_s, q_l) \rightarrow (-q_o, -q_s, -q_l)$ as discussed in Chapter 4.

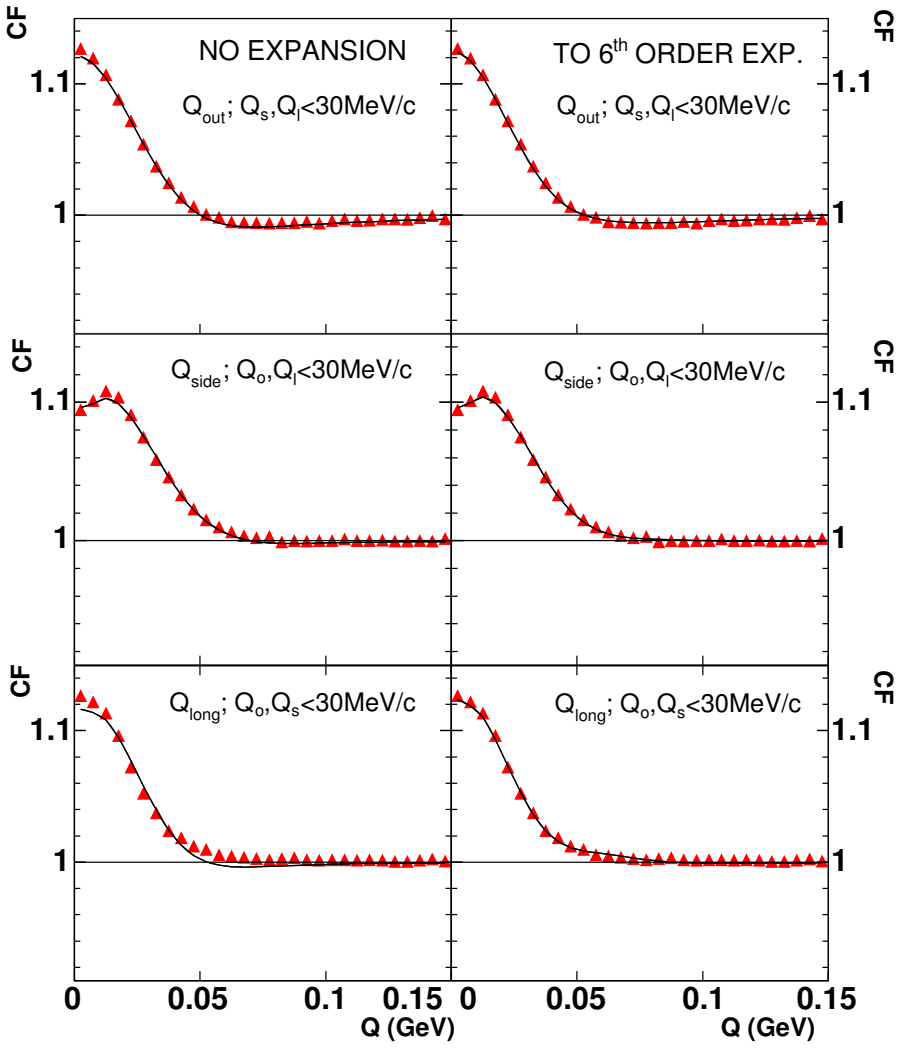

Figure 6.14: Projections of the 3 dimensional correlation functions and fits to equation (6.5) (left) and with the Edgeworth expansion to equation (6.12) to 6^{th} order (right).

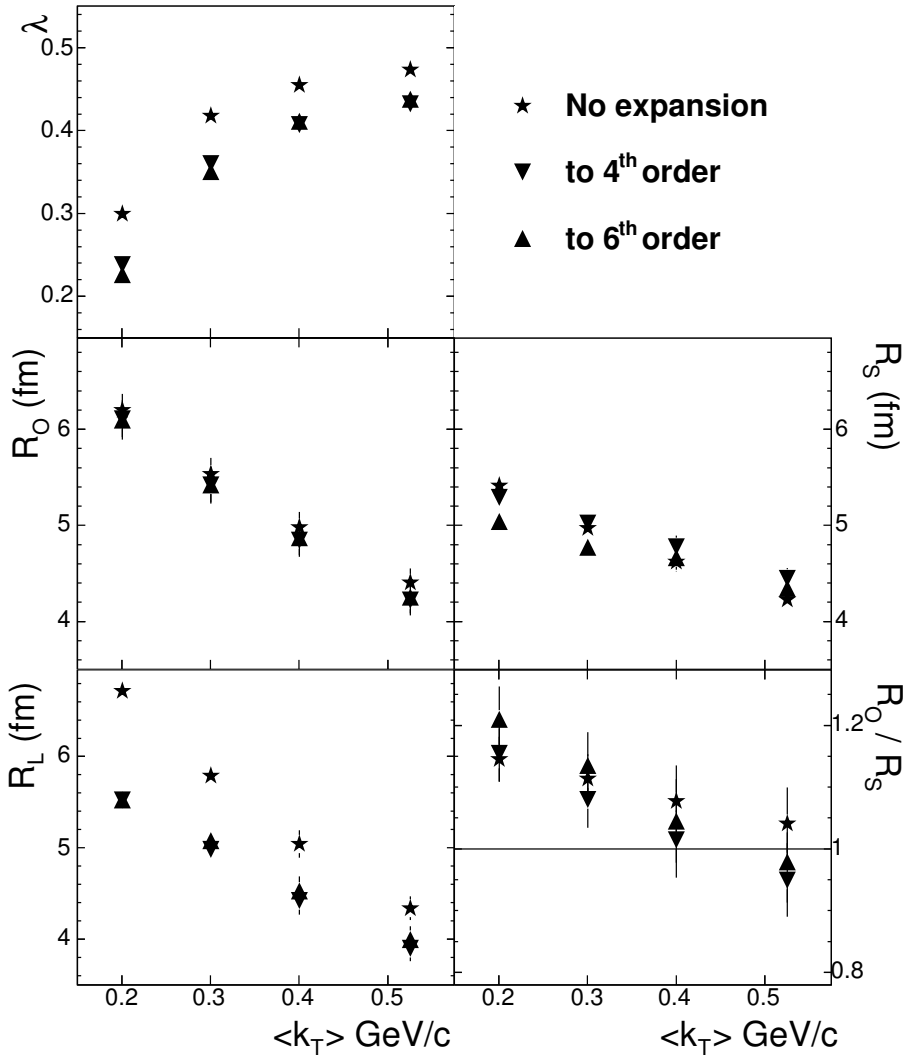

Figure 6.15: HBT parameters for 0-5% most central events for fits to equation (6.5) and to equation (6.12) to 4^{th} and to 6^{th} orders.

k_T (MeV/c)	150-250	250-350	350-450	450-600
$\kappa_{o,4}$ (4^{th} ord.)	0.37±0.05	0.36±0.04	0.33±0.05	0.40±0.06
$\kappa_{o,4}$	0.53±0.11	0.45±0.10	0.20±0.11	0.22±0.13
$\kappa_{o,6}$	0.83±0.39	0.53±0.38	0.63±0.44	-0.84±0.53
$\kappa_{s,4}$ (4^{th} ord.)	0.22±0.04	-0.03±0.04	-0.27±0.04	-0.50±0.05
$\kappa_{s,4}$	0.99±0.10	0.79±0.10	0.16±0.11	-0.07±0.13
$\kappa_{s,6}$	3.07±0.35	3.21±0.37	1.71±0.44	1.80±0.51
$\kappa_{l,4}$ (4^{th} ord.)	1.60±0.06	1.25±0.05	1.04±0.06	0.78±0.06
$\kappa_{l,4}$	1.32±0.07	0.70±0.07	0.54±0.09	0.32±0.11
$\kappa_{l,6}$	-1.76±0.29	-2.82±0.29	-2.41±0.35	-2.12±0.43

Table 6.1: $\kappa_{i,n}$ parameters for fits of the correlations functions up to 4^{th} order (when indicated) and 6^{th} order of the Edgeworth expansion for the 5% most central events. The extracted radii are shown in Fig. 6.15.

We fit our correlation functions to the form given by (6.12) up to 4^{th} and 6^{th} order of the Hermite polynomials, and compare with fits to (6.5) (without expansion). In Fig. 6.14 we show the projections of the correlation function for the 0-5% most central events and k_T between 150 and 250 MeV/c, and corresponding fits with no expansion in the left column and with expansion up to 6^{th} order in the right one; we observe a small improvement in the fit when we include the Edgeworth expansion in the fit. However, no significant differences are observed between a fit with an expansion to 4^{th} or 6^{th} order. In Fig. 6.15 the extracted HBT parameters as a function of k_T for the 0-5% most central events for the fits without expansion, with expansion up to 4^{th} order and with expansion up to 6^{th} order are shown. The corresponding values for the κ parameters are shown in Table 6.1. When comparing the extracted parameters including the expansion to 6^{th} order to those extracted without the

expansion, we observe that R_o decreases by $\sim$ 2% for all k_T bins, R_s changes between $\sim$ -7% for the lowest k_T bin (150-250) MeV/c and $\sim$ +3% for the highest one (450-600) MeV/c, and R_l decreases between $\sim$ 18% and $\sim$ 8% for the lowest and highest k_T bins respectively. Similar trends are observed at all centralities. This changes in the HBT radii can be considered as systematic deviation of the correlation function from a Gaussian, however we do not consider them as an uncertainty in the extracted HBT parameters. The main reason for this is that we do not know what the relation between the HBT parameters extracted when including the expansion and the source function is.

CHAPTER 7

RESULTS AND DISCUSSION

In this chapter the HBT parameters as a function of m_T for the 6 different centralities are presented. This allows us to study the centrality dependence of the m_T dependence of the HBT radii, which is discussed in the second section of the chapter. In the last section, the extracted parameters from a blast wave fit to the results are given and discussed. The expansion of the source is also studied.

7.1 m_T dependence of the HBT parameters for most central collisions

As already discussed in Chapter 4, the HBT radius parameters measure the sizes of the homogeneity regions (regions emitting particles of given momenta) [73]. Hence, for an expanding source, depending on the momenta of the pairs of particles entering the correlation function, different parts of the source are measured. Also, the size of these regions are controlled by the expanding velocity gradients [72, 74, 75]. Therefore the dependence of the transverse radii on the pair transverse mass contains dynamical information of the particle emitting source [54, 73].

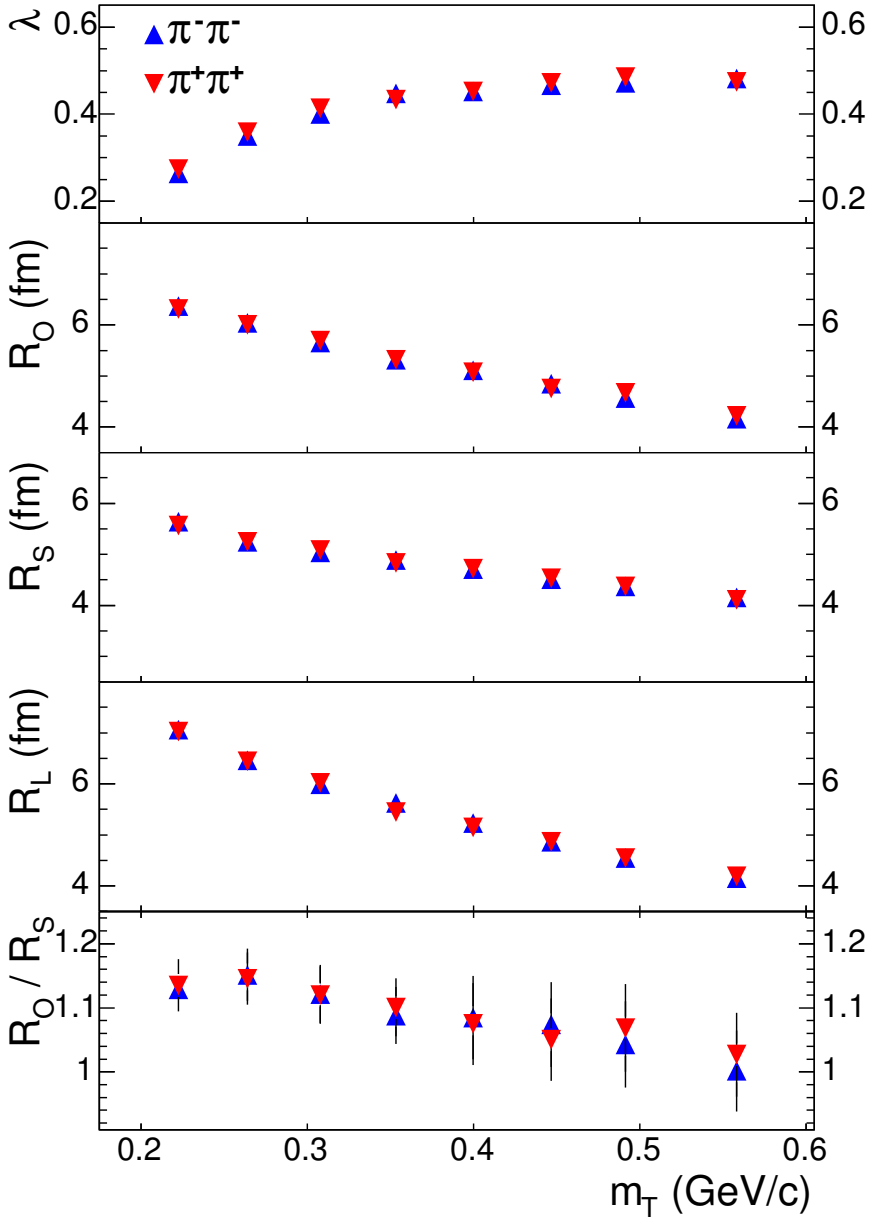

Figure 7.1: HBT parameters for 0-5% most central events for $\pi^+\pi^+$ and $\pi^-\pi^-$ correlation functions. Error bars include statistical and systematic uncertainties.

Figure 7.1 shows the HBT parameters λ, R_o, R_s, R_l and the ratio R_o/R_s for the 0-5% most central events as a function of m_T for $\pi^+\pi^+$ and $\pi^-\pi^-$ correlation functions. We observe an excellent agreement between the parameters extracted from the positively and negatively charged pion analyses. This confirms that the interaction between the outgoing particles an the positively charged source is negligible. The λ parameter increases with m_T, this is consistent with studies at lower energies [80, 97, 101, 107], in which the increase was attributed to decreased contributions of pions from long-lived resonances at higher p_T. The three HBT radii rapidly decrease as a function of m_T; the decrease of the transverse radii (R_o and R_s) with m_T is due to the radial flow [72, 74, 75]; the strong decrease in R_l is produced by the longitudinal flow [64, 72, 73, 75, 108]. R_o falls steeper than R_s with m_T which could suggest that R_o might be more affected by radial flow [82]. In contrast to several model predictions [77, 79], $R_o/R_s \sim 1$, which indicates short emission duration in a blast wave parametrization [82] as will be discussed later in this section.

In Fig. 7.2 we compare our extracted HBT radius parameters from $\pi^+\pi^+$ and $\pi^-\pi^-$ correlation functions for the 0-30% most central events with those obtained by the PHENIX collaboration [109] at the same beam energy and centrality. In general, very good agreement is observed in the three radii, although small discrepancies are seen in R_o at small relative momentum.

Figure 7.3 shows the HBT parameters vs. collision energy for midrapidity, low p_T $\pi^-\pi^-$ from central Au+Au, Pb+Pb or Pb+Au collisions [97, 98, 99, 100,

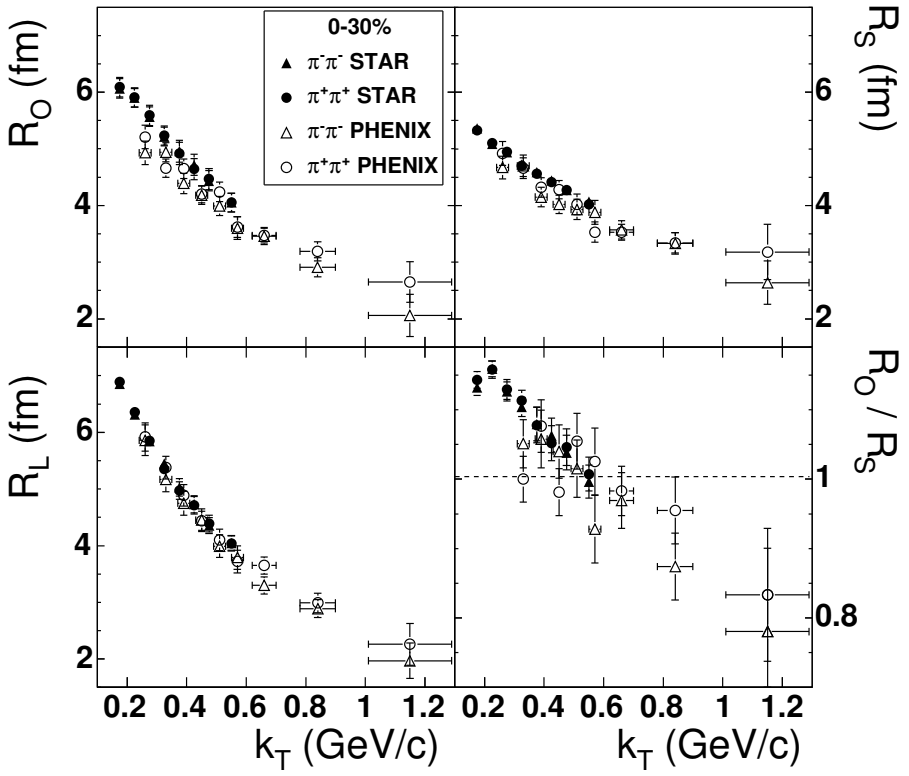

Figure 7.2: HBT parameters from STAR and PHENIX at the same beam energy and centrality, 0-30% most central events. Error bars include statistical and systematic uncertainties.

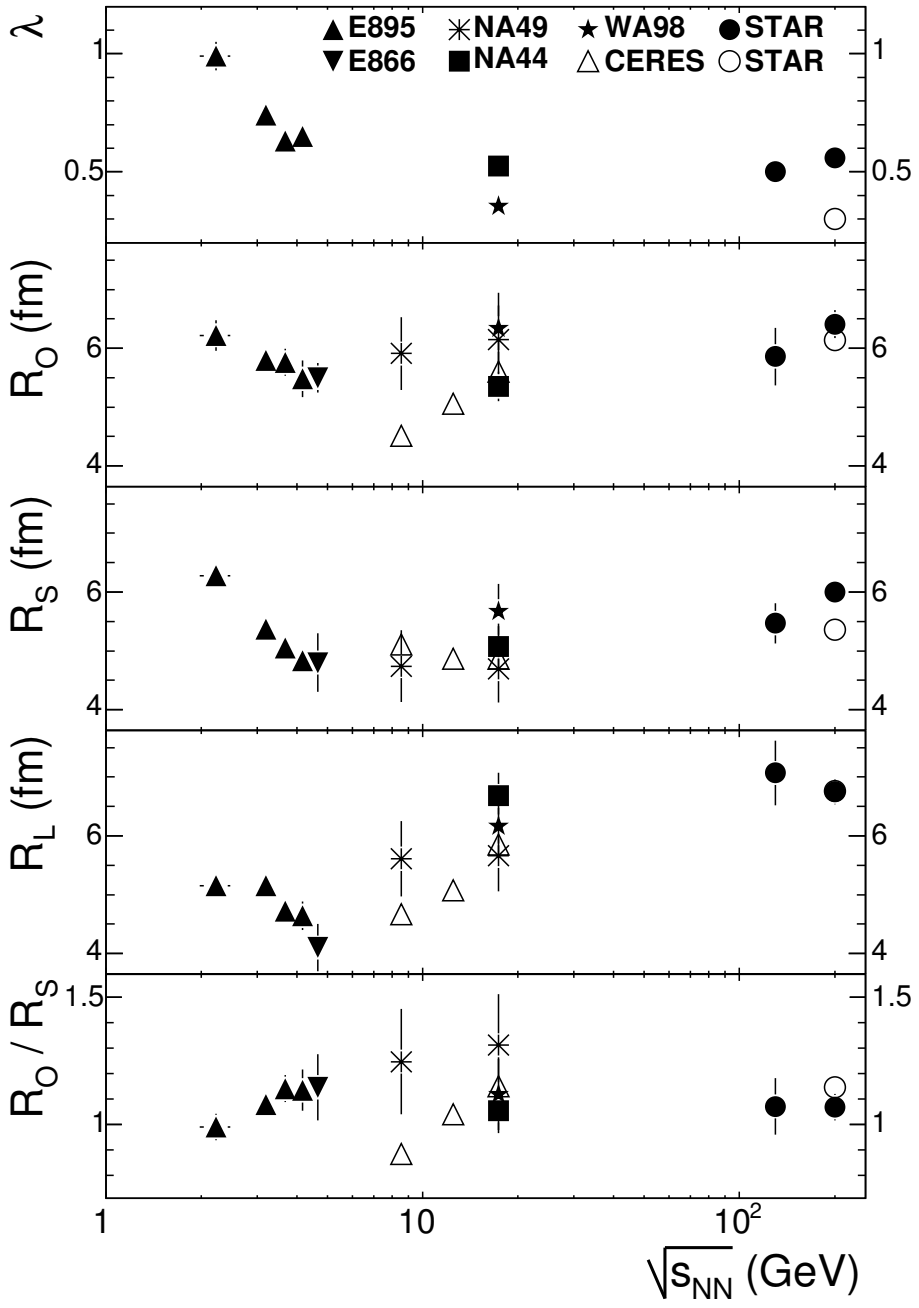

Figure 7.3: Energy dependence of π^- HBT parameters for central Au+Au, Pb+Pb or Pb+Au collisions at midrapidity and $p_T \approx 0.2$ GeV/c. Error bars on NA44, NA49, and STAR results include systematic uncertainties; error bars on other results are statistical only.

101]. In order to be able to compare with STAR previous results at $\sqrt{s_{NN}} = 130$ GeV, we applied similar cuts in our analysis as those described in [80] and we fit our correlation function according to the *standard* procedure described in section 6.4, closed circles ($\sqrt{s_{NN}} = 200$ GeV) in Fig. 7.3. With respect the STAR results at $\sqrt{s_{NN}} = 130$ GeV, we observe an increase of $\sim 10\%$ in the transverse radii R_o and R_s. In the case of R_s this increase could be attributed to a larger freeze-out volume for a larger pion multiplicity. R_l is consistent with our previous result. Also, the predicted increase by hydrodynamic models in the ratio R_o/R_s as a probe of the formation of QGP is not observed at $\sqrt{s_{NN}} = 200$ GeV.

We have also included in Fig. 7.3 the values for the HBT parameters at $\sqrt{s_{NN}} = 200$ GeV extracted when applying the cuts discussed in this thesis and fitting the correlation function accordingly to the *Bowler-Sinyukov* procedure (section 6.4), open circles in Fig. 7.3. This procedure is also used by the CERES collaboration. The smaller λ, R_o, and R_s can be explained by the different cuts as already discussed in section 6.4. The larger value for R_o/R_s is due to the improved procedure for taking Coulomb interaction into account, *Bowler-Sinyukov* procedure, section 6.4.

7.2 Centrality dependence of the m_T dependence

The excellent agreement in the results for positively and negatively charged pion correlation functions for the most central collisions shown in the previous section allows us to add the correlation functions for positive and negative

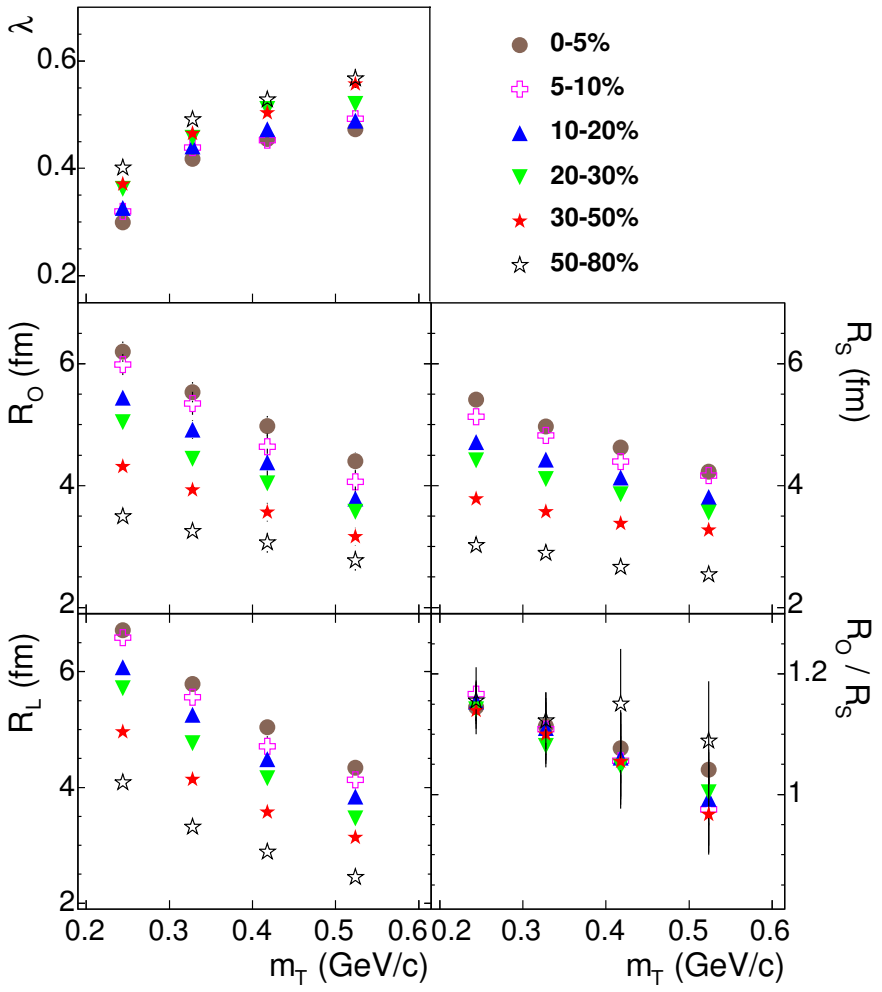

Figure 7.4: HBT parameters vs. m_T for 6 different centralities.

pions in order to improve statistics. All the results shown in the rest of this chapter correspond to these added correlation functions. The centrality dependence of the source parameters is presented in Fig. 7.4 where the HBT parameters are shown as a function of m_T for 6 different centralities. The λ parameter slightly increases with decreasing centrality. The three radii increase with increasing number of participants and R_l varies similar to R_o and R_s; for R_o and R_s this increase may be attributed to increase in the geometrical overlap of the two nuclei. $R_o/R_s \sim 1$, for all centralities.

7.3 Discussion of the centrality dependence of the m_T dependence

As already mentioned in section 7.1, the dependence of the HBT radii in the transverse mass contains dynamical information of the particle emitting source. In order to extract information about the dependence of the HBT radii on m_T for different centralities, we fit the m_T dependence of each HBT radii for each centrality from Fig. 7.4 by a simple power-law fit: $R_i(m_T) = R_i' \cdot (m_T/m_\pi)^{-\alpha_i}$ (solid lines in Fig. 7.5). Figure 7.6 shows the extracted fit parameters for the three HBT radii, R' in the top panel and α in the lower one, as a function of the number of participants, where $\mathrm{N_{participants}}$ has been calculated using a Glauber model calculation that is described in [110]. R' decreases with decreasing number of participants, consistently with the decreasing initial source size. α is approximately constant for R_l, this would indicate a constant longitudinal flow for all centralities; however, for the transverse radii R_o and R_s, α seems to decrease for the most peripheral collisions which could

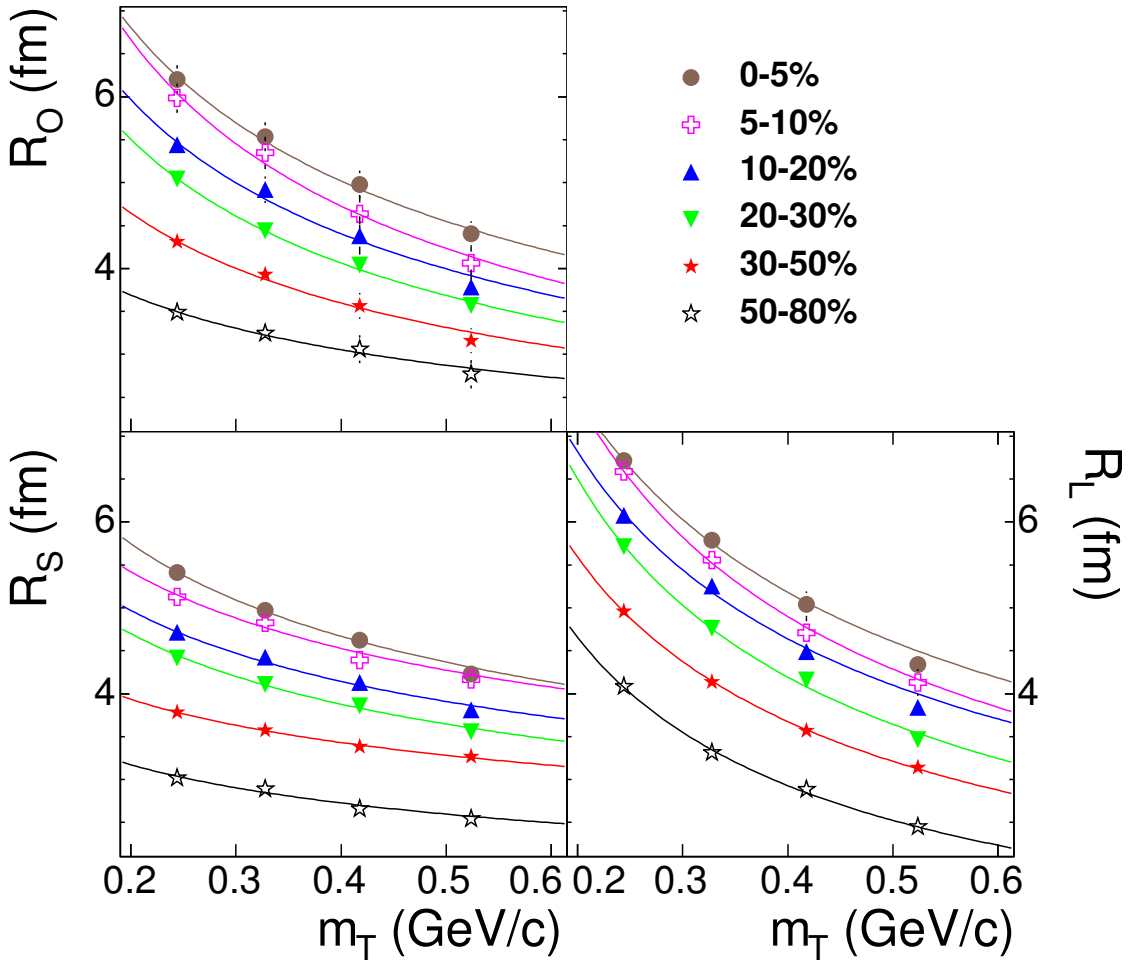

Figure 7.5: HBT radius parameters for 6 different centralities. The lines are power-law fits ($R_i(m_T) = R'_i \cdot (m_T/m_\pi)^{-\alpha_i}$) to each parameter for each centrality.

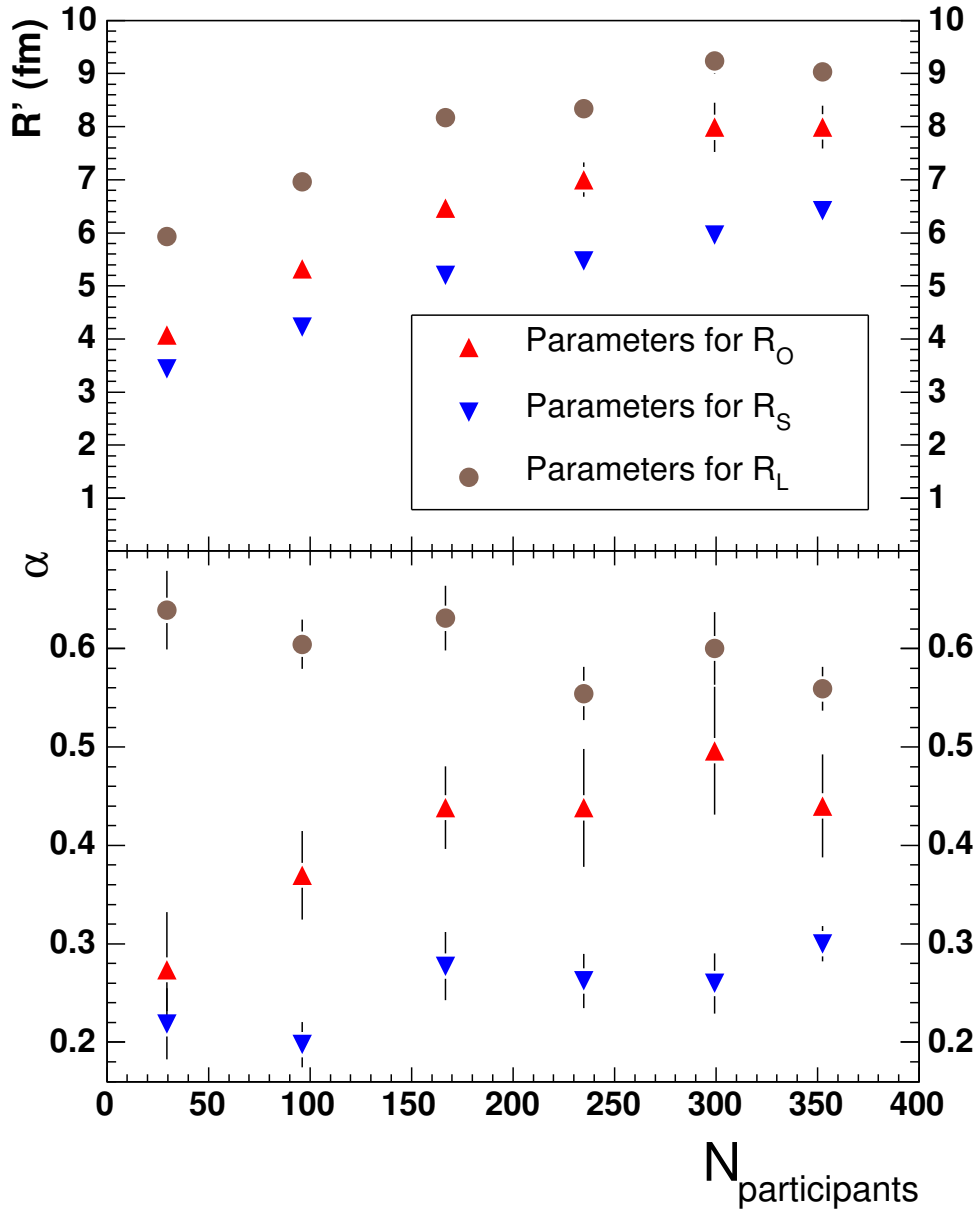

Figure 7.6: Extracted parameters from the power-law fits to the HBT radius parameters (lines in Fig. 7.5). R' in the top panel, α in the bottom.

Cent. (%)	T (MeV)	ρ_0	R (fm)	τ (fm/c)	$\Delta\tau$ (fm/c)	χ^2/dof
0-5	88 ± 2	1.04 ± 0.01	13.5 ± 0.1	9.3 ± 0.1	2.96 ± 0.04	9.50/58
5-10	99 ± 3	1.00 ± 0.01	12.4 ± 0.1	8.3 ± 0.2	2.49 ± 0.10	1.35/46
10-20	102 ± 3	0.97 ± 0.01	11.3 ± 0.1	7.6 ± 0.2	2.31 ± 0.08	1.69/48
20-30	105 ± 2	0.93 ± 0.01	10.3 ± 0.1	6.9 ± 0.1	2.00 ± 0.08	0.93/50
30-50	109 ± 3	0.82 ± 0.02	8.2 ± 0.2	6.0 ± 0.2	1.38 ± 0.18	1.25/50
50-80	110 ± 4	0.52 ± 0.05	4.5 ± 0.5	5.0 ± 0.3	0.31 ± 0.82	0.77/47

Table 7.1: Extracted parameters from a blast wave fit simultaneously to pion HBT radii, and pion, kaon, and proton transverse momentum spectra.

be an indication of a small decrease on transverse flow and/or an increase on temperature for those most peripheral collisions; this is consistent with the values for flow and temperature extracted from blast wave fits to pion, kaon, and proton transverse momentum spectra [111]. The decrease in α with decreasing number of participants is faster in R_o than in R_s which could again indicate that R_o may be more affected by radial flow [82].

7.4 Blast wave parametrization

It was already discussed that hydrodynamic calculations that successfully reproduce transverse momentum spectra and elliptic flow, fail to reproduce the HBT parameters [77]. In most cases, these calculations underestimate R_s and overestimate R_o and R_l; since R_s only probes the spatial extent of the source while R_o and R_l are sensitive to the duration of the particle emission and the system lifetime [54], they may be underestimating the system size and/or overestimating its emission duration and evolution time. We use a blast wave parametrization, designed to describe the freeze-out configuration,

to fit our data. In this section the extracted parameters and their physical implications are discussed.

This blast wave parametrization [82] assumes that the system is contained within an infinitely long cylinder along the beam line and requires longitudinal boost invariant flow. We use this parametrization to simultaneously fit the pion HBT radii and the pion, kaon and proton spectra [111] (to constraint temperature and flow velocity) with a single set of free parameters: the freeze-out temperature (T); the maximum flow rapidity (ρ_0); the radius (R) of the cylinder that confines the system; the system proper time ($\tau = \sqrt{t^2 - z^2}$); and the emission duration ($\Delta\tau$). In the fit, the transverse flow rapidity linearly increases from zero at the center to a maximum value at the edge of the system. The best fit parameters are summarized in Table 7.1.

Most of the parameters, as well as their evolution with centrality, agree with reasonable expectations. Temperature decreases with increasing centrality and the average transverse flow velocity $< \beta_T >$ increases with increasing centrality, both results are consistent with those extracted from blast wave fits to spectra only [111] and reflect increasing rescattering and expansion with centrality. This is also consistent with the observed increase in the system evolution time. We observe an increasing emission duration with centrality too.

The geometrical size of the source, $R_{\rm geom}$, can be calculated assuming a transverse expanding, longitudinally boost-invariant source, and a Gaussian

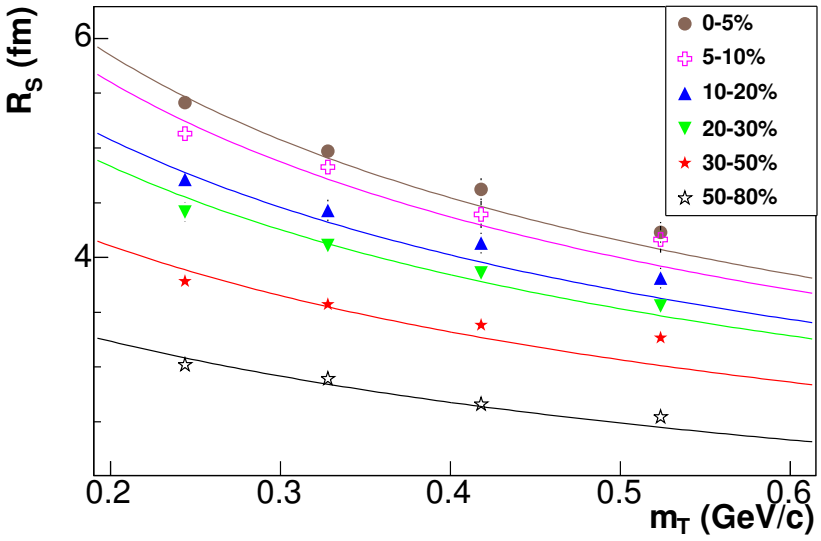

Figure 7.7: HBT parameter R_s. Lines represent the fits $R_s(m_T) = \sqrt{\frac{R^2_{\rm geom}}{1+\rho_0^2(\frac{1}{2}+\frac{m_T}{T})}}$.

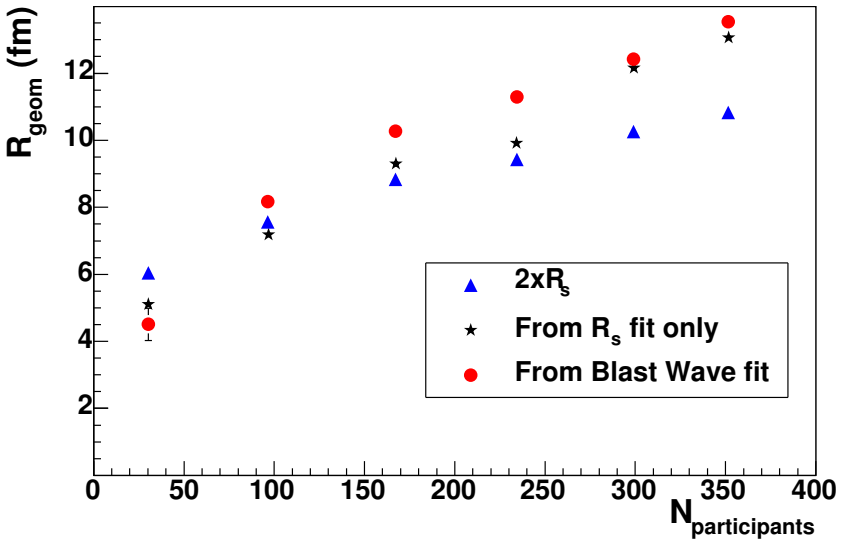

Figure 7.8: Extracted freeze-out source radius extracted from a blast wave fit; source radius $R_{\rm geom}$ from fits to R_s (lines in Fig. 7.7); and $2 \times R_s$ for the lowest k_T bin as a function of number of participants.

transverse density profile, by fitting the m_T dependence of R_s to:

$$R_s(m_T) = \sqrt{\frac{R^2_{\text{geom}}}{1+\rho_0^2(\frac{1}{2}+\frac{m_T}{T})}}, \tag{7.1}$$

where T is the freeze-out temperature and ρ_0 is the surface transverse rapidity [75]. Figure 7.7 shows the fits to R_s for each centrality with T and ρ_0 extracted from fits to pion, kaon, and proton transverse momentum spectra (T = 90 MeV, ρ_0 = 1.206 for the most central collisions and T = 120 MeV, ρ_0 = 0.829 for the most peripheral ones) [111]. The above extracted R_{geom} is shown in Figure 7.8 as a function of $N_{\text{participants}}$. R as extracted from the blast wave fit discussed above is also shown. We observe a good agreement between the two extracted radii, that increase from $\sim$5 fm for the most peripheral collisions to $\sim$13 fm for the most central ones following the growth of the system initial size.

As already mentioned, R_s carries only spatial information about the source [52, 72]. In the particular case of vanishing space-momentum correlations (no transverse flow or $T = \infty$), the radius of the "whole" source R is approximately described by $R = 2 \times R_s$, independent of k_T, where R_s is the extracted HBT side radius, which in this particular case is the RMS of the distribution of particles in the transverse plane at freeze-out. In Fig. 7.8 we have included $2 \times R_s$ for our lowest k_T bin, k_T = 150-250 MeV/c, in order to compare it with the extracted source radii. We observe that for the most peripheral collision $2 \times R_s$ is similar to R indicating smaller space-momentum correlations (*i.e.* less transverse flow and/or higher temperature); however, for the most central collisions, $2 \times R_s$ is smaller than the extracted radii indicating an increase

in flow and/or a decrease in temperature that increase the space-momentum correlations in these collisions.

7.4.1 Source expansion

For non-central collisions, the initial overlapping region of the two nuclei has an elliptic shape with the larger axis perpendicular to the reaction plane (out-of-plane) and the shorter axis in the reaction plane (in-plane) (see Fig. 3.3). The initial in-plane ($R_{x,\text{initial}}$) and out-of-plane ($R_{y,\text{initial}}$) radii can be calculated as $2 \times R^{RMS}_{i,\text{initial}}$ for $i = x, y$, if one assumes homogeneous distribution of particles, where $R^{RMS}_{i,\text{initial}}$ is the root mean squared of the distribution of particles in the 2-dimensional almond shaped initial overlapping region. In this analysis this initial distribution of particles in the transverse plane was calculated using the Monte Carlo Glauber model calculation described in [110]. The azimuthally integrated initial radius of the ellipse (R_{initial}) can be calculated from those two radii as

$$R_{\text{initial}} = \sqrt{\frac{R^2_{x,\text{initial}} + R^2_{y,\text{initial}}}{2}}. \tag{7.2}$$

The final in-plane (R_x) and out-of-plane (R_y) radii can be calculated from the extracted radius R from the blast wave parametrization and the final source eccentricity, calculated as $\varepsilon_{\text{final}} \approx 2R^2_{s,2}/R^2_{s,0}$ where $R^2_{s,2}$ and $R^2_{s,0}$ are the 0^{th} and 2^{nd} order R_s Fourier coefficients [70], as follows:

$$\begin{aligned} R^2_x &= (1-\varepsilon)R^2 \\ R^2_y &= (1+\varepsilon)R^2 \end{aligned} \tag{7.3}$$

The final eccentricity values are: 0.0049 ± 0.01, 0.0289 ± 0.01, 0.0775 ± 0.01, 0.1111 ± 0.01, 0.1289 ± 0.01, from most central to most peripheral, where the uncertainties are experimental only [70].

Figure 7.9 (bottom panel) shows $R/R_{initial}$ vs. number of participants for in-plane, out-of-plane and azimuthally integrated directions. The relative expansion of the source R/R_{initial}, is found to be stronger in-plane than out-of-plane for peripheral collisions, and similar in both directions for the most central ones. The azimuthally integrated radius indicates a stronger expansion of the source for the central collisions than for peripheral however, this expansion seems to be very similar for all centralities decreasing just for the most peripheral cases. Figure 7.9 (top panel) shows the overall expansion of the source given by $R - R_{\text{initial}}$ vs. number of participants. This expansion clearly increases with centrality and it is similar in-plane and out-of-plane, specially for the most central collisions.

We would like to know what is the origin of the expansion and in particular what is causing the differences between in-plane and out-of-plane expansions. We know that most of the collisions have an initial spatial anisotropy, they are out-of-plane extended at the initial stage. Only in the most central collisions the initial source will be almost spherical. This initial spatial anisotropy induces an energy density gradient stronger in the in-plane than in the out-of-plane direction, which, by particle reinteraction, generates an initial pressure gradient also stronger in-plane than out-of-plane. As the centrality increases

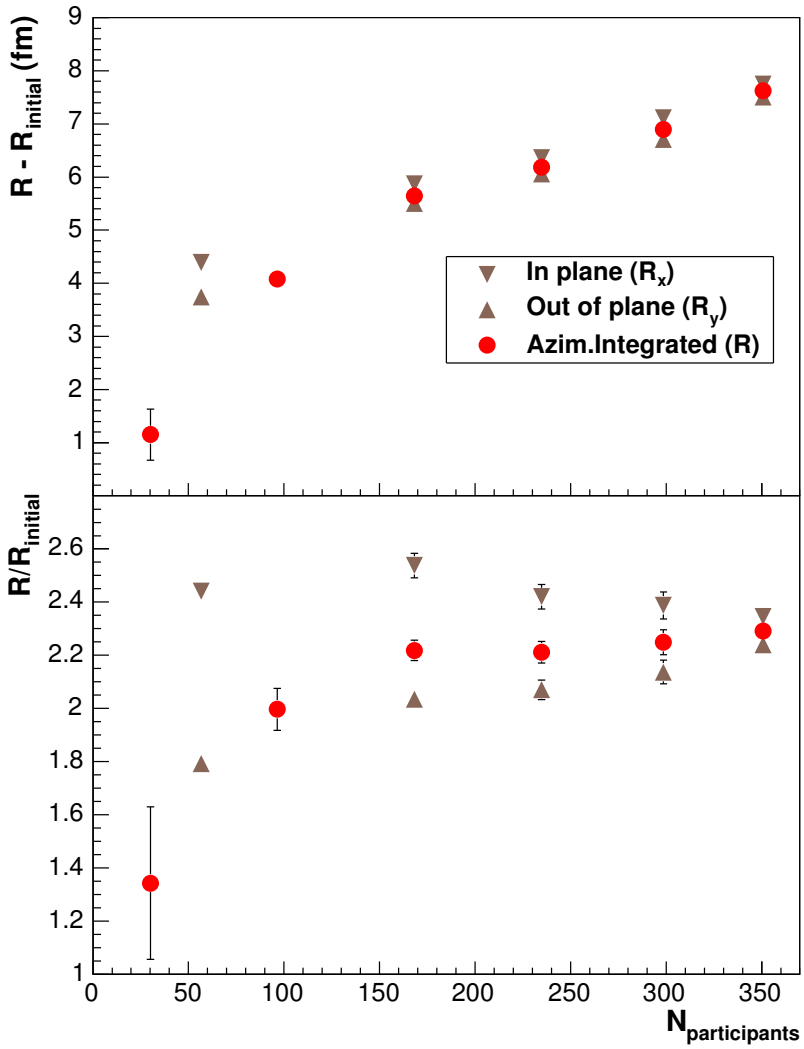

Figure 7.9: $R - R_{\text{initial}}$ (top panel) and R/R_{initial} (bottom panel) for the azimuthally integrated analysis and in the x (in-plane) and y (out-of-plane) direction vs. number of participants

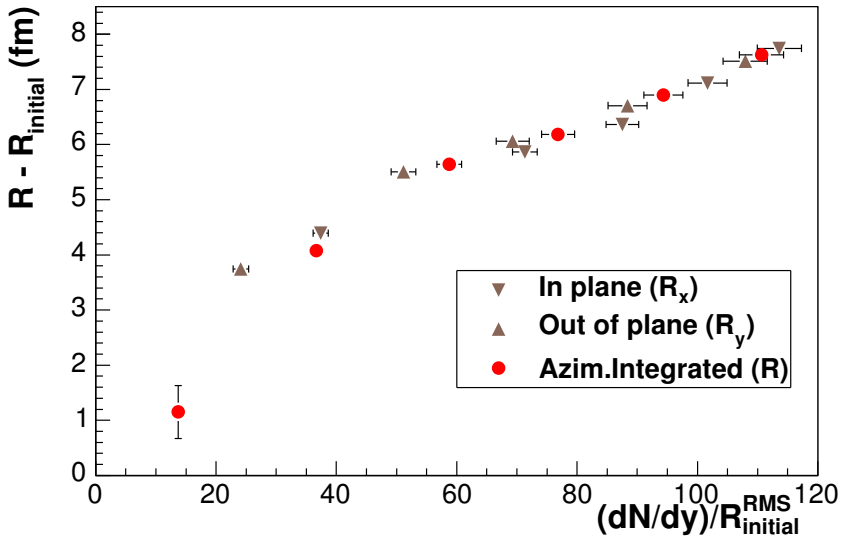

Figure 7.10: $R - R_{\text{initial}}$ for the azimuthally integrated analysis and in the x (in-plane) and y (out-of-plane) direction vs. $(dN/dy)/R^{RMS}_{\text{initial}}$

the difference between the initial energy density gradient in-plane and out-of-plane diminishes, which brings the expansion in-plane and out-of-plane closer together.

Following this idea that the initial pressure gradients drive the expansion, we attempt to estimate the initial energy density gradient. We assume that the energy density at the center of the system scales with the particle multiplicity, which we obtained from the pion dN/dY as reported in [111]. An estimate of the energy density gradient may be obtained by dividing the maximum energy density by the initial spatial RMS that we have introduced earlier. Doing so, we assume that this spatial RMS scales with the distance

between the center and the edge of the system where the energy density is zero.

Figure 7.10 shows $R - R_{\text{initial}}$ vs. $(dN/dy)/R^{RMS}_{\text{initial}}$, where R^{RMS}_{initial} is the corresponding in-plane, out-of-plane and azimuthally integrated initial RMS described before. We observe a clear scaling for R_x and R_y as well as for the azimuthally integrated radius R with $(dN/dy)/R^{RMS}_{\text{initial}}$. For the same centrality, the in-plane radius corresponds to a larger value of $(dN/dy)/R^{RMS}_{\text{initial}}$ than the out-of-plane one indicating that the expansion is actually driven by the initial pressure gradient.

The good fit to the data obtained with the blast wave parametrization, consistent with expansion, and the comparison in different ways of the initial and final sizes of the source clearly indicate that the results can be interpreted in terms of collective expansion that could be driven by the initial pressure gradient. However, the time scales extracted from the fit seems to be small, *i.e.* smaller than the values predicted by most hydrodynamic models [77]. Time scales are discussed next.

7.4.2 Time scales

From the dependence of R_l on m_T shown in Fig. 7.11 and assuming boost-invariant longitudinal flow, we can extract information about the system evolution time-scale, or proper time of freeze-out, of the source by fitting it to a formula first suggested by Sinyukov and collaborators [73, 108] and then

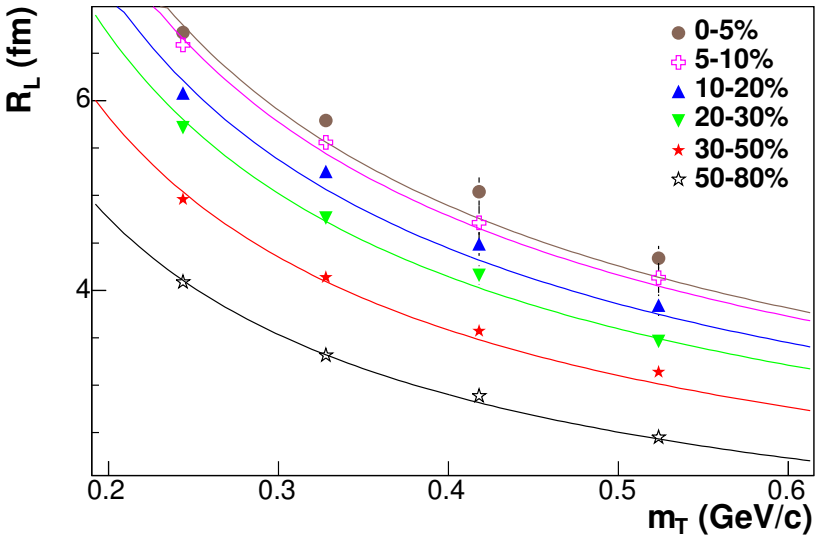

Figure 7.11: Longitudinal HBT radius R_l. Lines represent the fits $R_l = \tau\sqrt{\frac{T}{m_T}\frac{K_2(m_T/T)}{K_1(m_T/T)}}$ for each centrality.

improved by others [64, 75, 82]:

$$R_l = \tau\sqrt{\frac{T}{m_T}\frac{K_2(m_T/T)}{K_1(m_T/T)}}, \tag{7.4}$$

where T is the freeze-out temperature and K_1 and K_2 are the modified Bessel functions of order 1 and 2. This expression also assumes vanishing transverse flow and instantaneous freeze-out in proper time (*i.e.* $\Delta\tau$ = 0). The first assumption is approximatively justified by the small dependence of R_l on ρ_0 in a full blast wave calculation [82]; the second approximation is justified by the small $\Delta\tau$ from blast wave fits. Figure 7.11 also shows the fits to R_l (lines) using temperatures, T, consistently with spectra as for the fit to R_s. The extracted values for the evolution time are shown in Fig. 7.12; we observe an

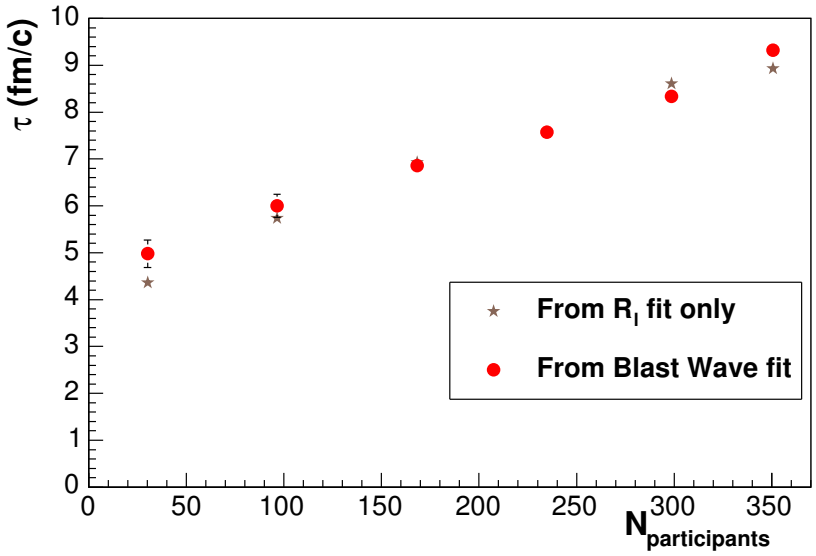

Figure 7.12: Evolution duration τ vs. number of participants as extracted from a fit to R_l, lines in Fig. 7.11 (stars) and from a blast wave fit to HBT parameters and spectra (circles).

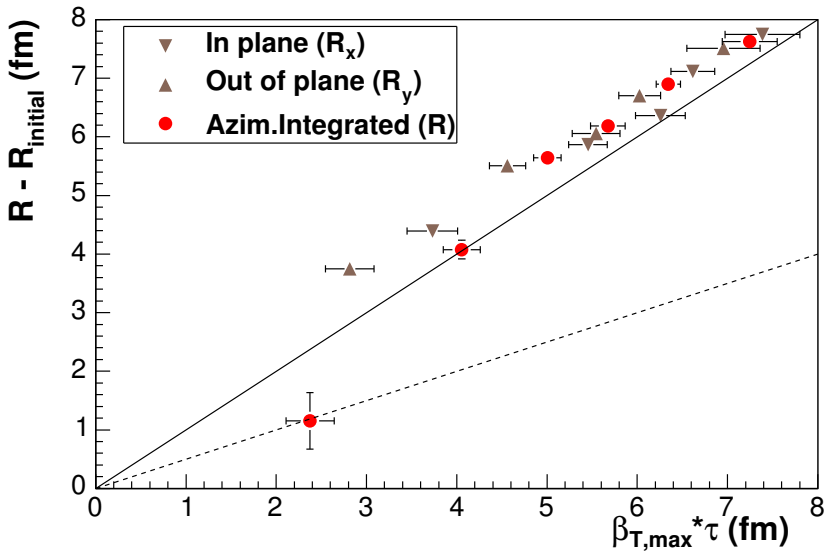

Figure 7.13: $R - R_{\text{initial}}$ for the azimuthally integrated analysis and for the in-plane and out-of-plane directions vs. $\beta_{T,\text{max}} \cdot \tau$. The continues line is a "$y = x$" line; the dashed line is a "$y = 0.5x$" line.

increase in evolution time with centrality from $\tau \approx 4$ fm/c for the most peripheral events to $\tau \approx 9$ fm/c for the most central ones. In the same plot, the extracted evolution time from the blast wave fit is shown. Good agreement is observed between the two extracted evolution times for all centralities. They are surprisingly small compared to hydrodynamical calculations which predict a freeze-out time of ~ 15 fm/c and not of ~ 9 fm/c. These hydrodynamical calculations may over-predict the system lifetime or our assumption in which the extraction of τ is based, longitudinal boost invariant expansion, may be wrong.

As a check for the consistency of the evolution time extracted from the blast wave fit, Fig. 7.13 shows the final source radius as extracted from the blast wave fit minus the initial edge source size vs. $\beta_{T,\text{max}} \cdot \tau$. Here, $\beta_{T,\text{max}}$ is the maximum flow velocity and the one we would expect to measure at the edge of the expanding source at kinetic freeze-out. It has been calculated from the ρ_0 blast wave parameter shown in Table 7.1. The evolution time, τ, is the blast wave parameter shown in Fig. 7.12. The systematic error in $\beta_{T,\text{max}} \cdot \tau$ comes from the finite size of the centrality bins. If the extracted radius and evolution time are right, we expect that the final edge radius can be related to the initial one by the relation $R_{\text{final}} < R_{\text{initial}} + \beta_{T,\text{max}} \cdot \tau$ so that the points in Fig. 7.13 should be clearly below the solid line ($x = y$). Most points are clearly above the line which may suggest that τ is not properly calculated within the blast wave parametrization. A larger τ would move the points below the line.

In order to calculate what values for $R - R_{initial}$ as a function of $\beta_{T,max}\tau$ would be a reasonable expectation, a possible approach would be to set a profile for the transverse flow velocity at the edge like: $\beta_{T,\text{edge}} = \frac{t}{\tau}\beta_{T,\text{max}}$. We can then expect R_{final} to be given by $R_{\text{final}} = R_{\text{initial}} + \int_0^\tau \beta_{T,\text{edge}} dt = R_{\text{initial}} + 0.5\beta_{T,\text{max}} \cdot \tau$. The dashed line in Fig. 7.13 is a $y = 0.5 \cdot x$ line and indicates where the results of this calculation would be. We see that, as expected, the points are even farther away (more than two times) from this line confirming that τ may not be properly calculated.

However the procedure followed to get Fig. 7.13 has a problem. In order to calculate the initial and final edge radii of the whole source, some shape

for the source needs to be assumed. In this analysis we assumed a hard edge shape ("box profile") for both, initial and final, sources, and calculated the radii as $2 \cdot R^{RMS}$ where R^{RMS} is the RMS of the distribution of particles in the transverse plane. This is only true for a homogeneous distribution of particles. It would be better if we did not have to assume any shape and could compare the initial and final RMS's. In order to do that we assume an initial 2 dimensional Gaussian transverse density profile with $\sigma = R^{RMS}_{initial}$ in which every particle has a transverse radial velocity $\beta_T = \frac{r}{R}\beta_{T,max}$ so that the equation of motion for each particle is given by: $r = r_0 e^{Bt}$ where $B = \frac{\beta_{T,max}}{R}$. This implies that the initial Gaussian profile evolves in the presence of a time-independent non-relativistic Hubble flow. By studying its evolution we expect to extract more information on the evolution time of our source.

If the final transverse distribution of particles is given by a function $f(r,t)$, then, by the conservation on the number of particles

$$\frac{1}{2\pi\sigma_0^2}\int_0^b e^{-r^2/2\sigma_0^2} r\ dr = \int_0^{be^B t} f(r,t) r\ dr \tag{7.5}$$

If we differentiate both sides of this equation with respect to b,

$$\frac{1}{2\pi\sigma_0^2} e^{-b^2/2\sigma_0^2} \cdot b = f(be^{Bt}) \cdot b \cdot e^{2Bt} \tag{7.6}$$

And changing the variable to $r = be^{Bt}$:

$$f(r,t) = \frac{1}{2\pi(\sigma_0 e^{Bt})^2} e^{-r^2/2(\sigma_0 e^{Bt})^2} \tag{7.7}$$

So that the final distribution in indeed a Gaussian with $\sigma(t) = \sigma_0 e^{Bt}$, which allows us to study the evolution from the initial to the final RMS.

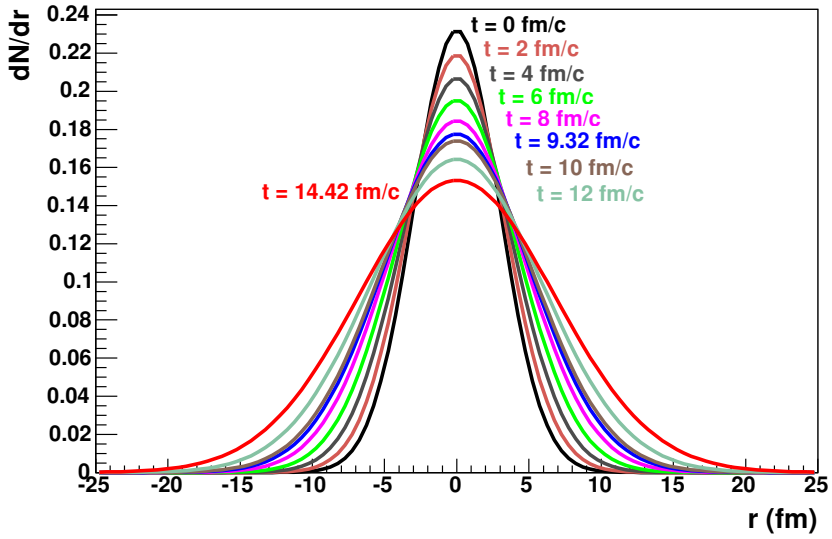

Figure 7.14: Evolution of a Gaussian distribution for a constant number of particles with standard deviation changing with time as $\sigma(t) = \sigma_0 e^{\beta_{T,max} \cdot t/R}$.

As an example, Fig 7.14 shows the evolution of the Gaussian distribution of particles for the 0-5% most central collisions. We observe that at the time extracted from the blast wave fit the Gaussian has not yet reached its final $\sigma = RMS_{final}$. It needs 14.42 fm/c to reach it. However this time should be a lower limit of the actual evolution time since we assume that all the particles have already a small transverse velocity at $t = 0$. This extracted time may confirm the conclusion from Fig. 7.13 that the evolution time extracted from the blast wave fit is too small. Table 7.2 shows the comparison between the two extracted times for different centralities. We observe that the one extracted from the blast wave fit is smaller in most of the centralities.

Centrality (%)	BW τ (fm/c)	τ_{min} (fm/c)
0-5	9.3 ± 0.1	14.4 ± 1.1
5-10	8.3 ± 0.2	13.2 ± 1.0
10-20	7.6 ± 0.2	11.9 ± 1.1
20-30	6.9 ± 0.1	11.2 ± 0.9
30-50	6.0 ± 0.2	8.4 ± 0.8
50-80	5.0 ± 0.3	2.8 ± 0.6

Table 7.2: Evolution time as extracted from the blast wave fit compared to the one extracted from the evolution of initial Gaussian density profile and which may be a lower limit of the actual evolution time.

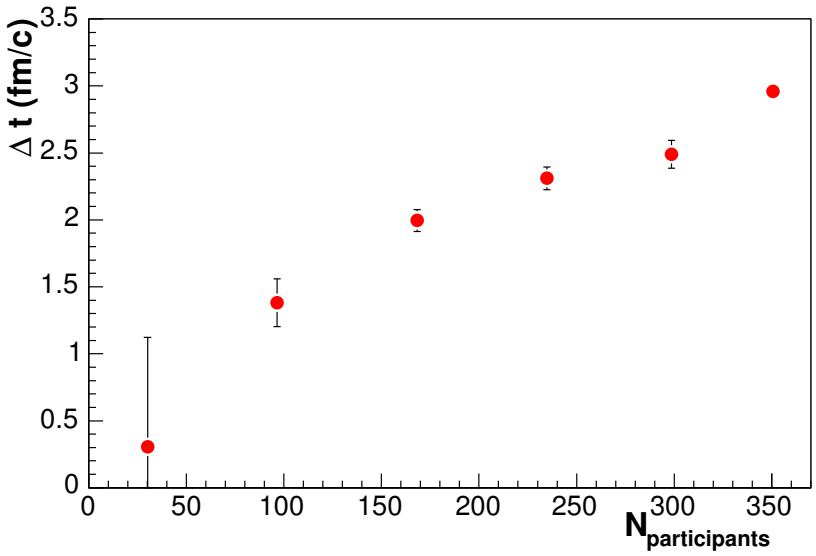

Figure 7.15: Emission duration time $\Delta\tau$ vs. number of participants as extracted using a blast fit to HBT parameters and spectra.

Figure 7.15 shows the emission duration time, $\Delta\tau$ as a function of the number of participants extracted from the blast wave fit to pion HBT parameters and spectra described above. $\Delta\tau$ increases with increasing centrality up to $\sim$ 3 fm/c. As for the proper time, the emission duration is very small for all centralities, however it has increased with respect to the values extracted from our analysis at $\sqrt{s_{NN}}$ = 130 GeV [82] due to the improved procedure of taking Coulomb interaction into account and the consequently increase in R_o.

CHAPTER 8

CONCLUSION

In this thesis, a systematic analysis of two identical pion interferometry in relativistic heavy ion collisions at RHIC has been presented. These collisions give us access to an unknown phase of matter at extremely high temperatures and densities in an asymptotic region of QCD.

It was shown that relativistic heavy ion collisions are not just a superposition of pp collisions. One important difference is the collective behavior seen in heavy ion collisions that is not observed in pp collisions. The m_T dependence of the HBT transverse radii indicates a strong transverse flow in the system, which depends on the centrality of the collision. By using the blast wave parametrization to fit our results, it was shown that the system collectively expands by a factor of at least two times for most centralities. This has been well established by HBT. It was determined that this collective expansion may be caused by the initial pressure gradient that was generated in the initial stages of the collision through particle rescattering in a very dense medium.

The long emission time predicted as a clear signature of the QGP formation that would have been reflected in the ratio $R_o/R_s >> 1$ has not been measured in this analysis. On the contrary, from the blast wave fit we extract rather short emission times. Also, the evolution times extracted from that fit are smaller than the one predicted by hydrodynamic calculations. This discrepancy may be due to an overestimation of R_l in the hydrodynamical model or due to the incorrect blast wave assumption of the system being longitudinally boost invariant. We have shown that slightly longer evolution times are more reasonable implying that, indeed, the longitudinal boost invariant assumption may have only limited validity. However, agreement between hydrodynamic calculations and HBT experimental results is needed in order to make the hydrodynamic description of the heavy ion collisions completely reliable.

APPENDIX A

RELEVANT VARIABLES

The coordinate system in STAR is defined to be right-handed, with the $+z$ axis defined by the direction of the clockwise RHIC beam. Positive y is defined to point vertically upwards, and $+x$ is perpendicular to both. The origin of the coordinate system is located at the center of the STAR solenoid magnet [86].

The transverse momentum of a particles is the modulus of the momentum vector transverse to the beam direction,

$$p_T = \sqrt{p_x^2 + p_y^2}. \tag{A.1}$$

The transverse mass of the particle having mass m_0 is,

$$m_T = \sqrt{p_T^2 + m_0^2}. \tag{A.2}$$

so that the transverse kinetic energy is $m_T - m_0$.

The azimuthal angle of the particles momentum in the laboratory frame is

$$\phi_{lab} = \tan^{-1}(p_y/p_x). \tag{A.3}$$

The rapidity of the particle is a measurement of its forward (beam) direction,

$$\mathrm{y} = \frac{1}{2}\ln\Big(\frac{E + p_z}{E - p_z}\Big), \tag{A.4}$$

which is boost invariant.

The pseudorapidity is defined as

$$\eta = \frac{1}{2}\ln\left(\frac{1+\cos(\theta)}{1-\cos(\theta)}\right) = -\ln\{\tan[\cos^{-1}(p_z/p)]\}, \tag{A.5}$$

where θ is the angle between the momentum of the particle and the beam axis. For $p >> m$, $\eta \approx$ y.

For a pair of particle, the transverse momentum vector of the pair is defined as,

$$\vec{k}_T = \left(\frac{\vec{p}_1 + \vec{p}_2}{2}\right)_T. \tag{A.6}$$

The transverse mass of the pair, for identical particles of mass m_0, is defined as,

$$m_T = \sqrt{|\vec{k}_T|^2 + m_0^2}. \tag{A.7}$$

The momentum difference of the pair is given by

$$\vec{q} = \vec{p}_1 - \vec{p}_2. \tag{A.8}$$

An invariant form of this momentum differences commonly used in a 1-dimensional HBT analysis is

$$q_{\text{inv}} = \sqrt{(q^0)^2 - |\vec{q}|^2}. \tag{A.9}$$

In the blast wave parametrization, the maximum transverse flow velocity is given by

$$\beta_{T,max} = \tanh(\rho), \tag{A.10}$$

where $\rho = \tilde{r}(\rho_0 + \rho_a \cos(2\phi))$ is the transverse flow rapidity. In an azimuthally integrated analysis $\rho_a = 0$ and $\rho = \tilde{r}\rho_0$.

The average transverse flow velocity is

$$\langle \beta_T \rangle = \frac{\int \text{arctanh}(\rho \frac{r}{R}) r \; dr}{\int r \; dr}. \tag{A.11}$$

The system evolution time is,

$$\tau = \sqrt{t^2 - z^2}. \tag{A.12}$$

BIBLIOGRAPHY

[1] M. Gell-Mann, Phys. Lett. **8**, 214 (1964).

[2] J. C. Collins and M. J. Perry, Phys. Rev. Lett. **34**, 1353 (1975).

[3] A. M. Polyakov, Phys. Lett. **B72**, 477 (1978).

[4] E. V. Shuryak, Phys. Lett. **B78**, 150 (1978).

[5] L. D. McLerran, Rev. Mod. Phys. **58**, 1021 (1986).

[6] E. W. Kolb and M. S. Turner, *The Early Universe* (Addison-Wesley, Redwood City, USA, 1990), Chap. 3.5.

[7] *Quark Matter 2004 Proceedings* (Oakland, USA, to be published in J. Phys. G., http://qm2004.lbl.gov/, 2004).

[8] *Quark Matter 2002 Proceedings* (Nantes, France, Nucl. Phys. **A715**, 2003).

[9] *Quark Matter 2001 Proceedings* (Stony Brook, USA, Nucl. Phys. **A698**, 2001).

[10] *Quark Matter 1999 Proceedings* (Torino, Italy, Nucl. Phys. **A661**, 1999).

[11] K. Rajagopal, AIP Conf. Proc. **602**, 339 (2001).

[12] N. K. Glendenning, Phys. Rept. **342**, 393 (2001).

[13] T. D. Lee and G. C. Wick, Phys. Rev. **D9**, 2291 (1974).

[14] F. Karsch, hep-lat/9903031 (1999).

[15] F. Karsch, Nucl. Phys. **A698**, 199 (2002).

[16] F. Karsch and E. Laermann, hep-lat/0305025 (2003).

[17] E. Laermann and O. Philipsen, hep-ph/0303042 (2003).

[18] F. Karsch, Lect. Notes Phys. **583**, 209 (2002).

[19] J. Cleymans, R. V. Gavai, and E. Suhonen, Phys. Rept. **130**, 217 (1986).

[20] F. R. Brown *et al.*, Phys. Rev. Lett. **65**, 2491 (1990).

[21] Z. Fodor and S. D. Katz, Phys. Lett. **B534**, 87 (2002).

[22] P. Braun-Munzinger, J. Stachel, and C. Wetterich, nucl-th/0311005 (2003).

[23] J. D. Bjorken, Phys. Rev. **D27**, 140 (1983).

[24] D. D'Enterria, nucl-ex/0306001 (2003).

[25] J. Kapusta, P. Lichard, and D. Seibert, Phys. Rev. **D44**, 2774 (1991).

[26] D. K. Srivastava and B. Sinha, Phys. Rev. Lett. **73**, 2421 (1994).

[27] J. Rafelski and B. Muller, Phys. Rev. Lett. **48**, 1066 (1982).

[28] P. Koch, B. Muller, and J. Rafelski, Phys. Rept. **142**, 167 (1986).

[29] P. Koch, B. Muller, H. Stocker, and W. Greiner, Mod. Phys. Lett. **A3**, 737 (1988).

[30] G. E. Bruno, nucl-ex/0403036 (2004).

[31] T. Matsui and H. Satz, Phys. Lett. **B178**, 416 (1986).

[32] D. Kharzeev, C. Lourenco, M. Nardi, and H. Satz, Z. Phys. **C74**, 307 (1997).

[33] M. C. Abreu *et al.*, Phys. Lett. **B477**, 28 (2000).

[34] J.-Y. Ollitrault, Phys. Rev. **D46**, 229 (1992).

[35] P. F. Kolb, J. Sollfrank, and U. W. Heinz, Phys. Rev. **C62**, 054909 (2000).

[36] H. Sorge, Phys. Rev. Lett. **78**, 2309 (1997).

[37] S. Voloshin and Y. Zhang, Z. Phys. **C70**, 665 (1996).

[38] C. Alt *et al.*, Phys. Rev. **C68**, 034903 (2003).

[39] B. Wosiek *et al.*, Nucl. Phys. **A715**, 510 (2003).

[40] D. Kharzeev, Nucl. Phys. **A715**, 35 (2003).

[41] J. Castillo, nucl-ex/0403027 (2004).

[42] D. Molnar and S. A. Voloshin, Phys. Rev. Lett. **91**, 092301 (2003).

[43] V. Greco, C. M. Ko, and P. Levai, Phys. Rev. **C68**, 034904 (2003).

[44] R. J. Fries, B. Muller, C. Nonaka, and S. A. Bass, Phys. Rev. **C68**, 044902 (2003).

[45] M. Gyulassy and M. Plumer, Phys. Lett. **B243**, 432 (1990).

[46] X.-N. Wang and M. Gyulassy, Phys. Rev. Lett. **68**, 1480 (1992).

[47] C. Adler *et al.*, Phys. Rev. Lett. **89**, 202301 (2002).

[48] C. Adler *et al.*, Phys. Rev. Lett. **90**, 082302 (2003).

[49] J. Adams *et al.*, Phys. Rev. Lett. **91**, 072304 (2003).

[50] R. Hanbury-Brown and R. Q. Twiss, Nature **178**, 1046 (1956).

[51] G. Goldhaber, S. Goldhaber, W.-Y. Lee, and A. Pais, Phys. Rev. **120**, 300 (1960).

[52] U. A. Wiedemann and U. W. Heinz, Phys. Rept. **319**, 145 (1999).

[53] M. Gyulassy, S. K. Kauffmann, and L. W. Wilson, Phys. Rev. **C20**, 2267 (1979).

[54] S. Pratt, Phys. Rev. Lett. **53**, 1219 (1984).

[55] G. C. Wick, Phys. Rev. **80**, 268 (1950).

[56] S. Chapman, P. Scotto, and U. W. Heinz, Nucl. Phys. **A590**, 449c (1995).

[57] M. G. Bowler, Z. Phys. **C39**, 81 (1988).

[58] G. Baym and P. Braun-Munzinger, Nucl. Phys. **A610**, 286c (1996).

[59] S. Pratt, Phys. Rev. **D33**, 72 (1986).

[60] M. G. Bowler, Phys. Lett. **B270**, 69 (1991).

[61] W. A. Zajc *et al.*, Phys. Rev. **C29**, 2173 (1984).

[62] H. W. Barz, Phys. Rev. **C59**, 2214 (1999).

[63] S. Chapman, P. Scotto, and U. W. Heinz, Phys. Rev. Lett. **74**, 4400 (1995).

[64] M. Herrmann and G. F. Bertsch, Phys. Rev. **C51**, 328 (1995).

[65] U. W. Heinz, B. Tomasik, U. A. Wiedemann, and Y. F. Wu, Phys. Lett. **B382**, 181 (1996).

[66] U. Heinz, private communication.

[67] M. I. Podgoretsky, Sov. J. Nucl. Phys. **37**, 272 (1983).

[68] S. Pratt, Phys. Rev. **D33**, 1314 (1986).

[69] G. Bertsch, M. Gong, and M. Tohyama, Phys. Rev. **C37**, 1896 (1988).

[70] J. Adams *et al.*, Phys. Rev. Lett. **93**, 012301 (2004).

[71] U. W. Heinz, A. Hummel, M. A. Lisa, and U. A. Wiedemann, Phys. Rev. **C66**, 044903 (2002).

[72] U. A. Wiedemann, Phys. Rev. **C57**, 266 (1998).

[73] A. N. Makhlin and Y. M. Sinyukov, Z. Physics. **C39**, 1988 (1988).

[74] B. Tomasik, U. A. Wiedemann, and U. W. Heinz, Nucl. Phys. **A663**, 753 (2000).

[75] U. A. Wiedemann, P. Scotto, and U. W. Heinz, Phys. Rev. **C53**, 918 (1996).

[76] D. Teaney, J. Lauret, and E. Shuryak, nucl-th/0110037 (2001).

[77] U. W. Heinz and P. F. Kolb, hep-ph/0204061 (2002).

[78] P. F. Kolb and U. Heinz, nucl-th/0305084 (2003).

[79] D. H. Rischke and M. Gyulassy, Nucl. Phys. **A608**, 479 (1996).

[80] C. Adler *et al.*, Phys. Rev. Lett. **87**, 082301 (2001).

[81] K. Adcox *et al.*, Phys. Rev. Lett. **88**, 192302 (2002).

[82] F. Retière and M. A. Lisa, nucl-th/0312024 (2003).

[83] M. Harrison, T. Ludlam, and S. Ozaki, Nucl. Instrum. Meth. **A499**, 235 (2003).

[84] T. Ludlam, Nucl. Instrum. Meth. **A499**, 428 (2003).

[85] K. H. Ackermann *et al.*, Nucl. Instrum. Meth. **A499**, 624 (2003).

[86] F. Bergsma *et al.*, Nucl. Instrum. Meth. **A499**, 633 (2003).

[87] R. Bellwied *et al.*, Nucl. Instrum. Meth. **A499**, 640 (2003).

[88] K. H. Ackermann *et al.*, Nucl. Instrum. Meth. **A499**, 713 (2003).

[89] A. Braem *et al.*, Nucl. Instrum. Meth. **A499**, 720 (2003).

[90] M. Beddo *et al.*, Nucl. Instrum. Meth. **A499**, 725 (2003).

[91] M. Anderson *et al.*, Nucl. Instrum. Meth. A **499**, 659 (2003).

[92] L. Kochenda *et al.*, Nucl. Instrum. Meth. **A499**, 703 (2003).

[93] M. Anderson *et al.*, Nucl. Instrum. Meth. **A499**, 679 (2003).

[94] H. J. Crawford *et al.*, Nucl. Instrum. Meth. **A499**, 766 (2003).

[95] C. Adler *et al.*, Nucl. Instrum. Meth. **A499**, 778 (2003).

[96] W. Blum and L. Rolandi, *Particle detection with drift chambers* (Springer, Berlin, Germany, 1993).

[97] M. A. Lisa *et al.*, Phys. Lett. **B496**, 1 (2000).

[98] J. H. Lee, prepared for 2nd Catania Relativistic Ion Studies: Measuring the Size of Things in the Universe: HBT Interferometry and Heavy Ion Physics (CRIS 98), Acicastello, Italy, 8-12 Jun 1998.

[99] T. Alber, Nucl. Phys. **A590**, 453c (1995).

[100] I. G. Bearden *et al.*, Nucl. Phys. **A661**, 456 (1999).

[101] M. M. Aggarwal *et al.*, Eur. Phys. J. **C16**, 445 (2000).

[102] L. Ahle *et al.*, Phys. Rev. **C66**, 054906 (2002).

[103] Y. Sinyukov *et al.*, Phys. Lett. **B432**, 248 (1998).

[104] D. Adamova *et al.*, Nucl. Phys. **A714**, 124 (2003).

[105] R. Lednicky and V. L. Lyuboshitz, Yad. Fiz **35**, 1316 (1982), fortran program provided by R. Lednicky.

[106] T. Csorgo, S. Hegyi, and W. A. Zajc, nucl-th/0310042 (2003).

[107] I. G. Bearden *et al.*, Phys. Rev. **C58**, 1656 (1998).

[108] S. V. Akkelin and Y. M. Sinyukov, Phys. Lett. **B356**, 525 (1995).

[109] S. S. Adler *et al.*, nucl-ex/0401003, Submitted to Phys. Rev. Lett. (2004).

[110] J. Adams *et al.*, nucl-ex/0311017, Submitted to Phys. Rev. Lett. (2003).

[111] J. Adams *et al.*, Phys. Rev. Lett. **92**, 112301 (2004).